

**PLASTIC DEFORMATION OF CRYSTALS:  
ANALYTICAL AND COMPUTER SIMULATION STUDIES OF  
DISLOCATION GLIDE**

**CONTENTS**

ABSTRACT .....	111
I. INTRODUCTION.....	1
II. OUTLINE OF THE PROBLEM.....	3
III. SPECIFIC PRIOR WORK .....	7
IV. PURPOSE AND SCOPE OF THE PRESENT INVESTIGATION.....	16
V. ANALYTICAL CALCULATIONS.....	20
A. ATHERMAL GLIDE.....	20
1. CRSS FOR LIKE OBSTACLES .....	20
2. CRSS FOR UNLIKE OBSTACLES .....	35
a) Two Types Of Obstacles .....	39
b) Arbitrary Distribution of Obstacles .....	41
B. THERMALLY ACTIVATED GLIDE.....	44
VI. COMPUTER SIMULATION.....	50
A. BASIC CODING TECHNIQUES.....	52
1. Storing the Array .....	53
2. Representing the Dislocation.....	56
3. Advancing the Dislocation .....	57
B. APPLICATIONS AND RESULTS .....	61

**MAST**

— NOTICE —

This report was prepared as an account of work sponsored by the United States Government. Neither the United States nor the United States Department of Energy, nor any of their employees nor any of their contractors, subcontractors, or their employees, makes any warranty, explicit or implied, or assumes any legal liability or responsibility for the accuracy, completeness, or usefulness of any information, apparatus, product, or process disclosed, or represents that its use would not infringe privately owned rights.

1. DISLOCATION GLIDE THROUGH LARGE ARRAYS .....	61
a) Correction to Theory .....	65
b) Thermally Activated Glide .....	66
2. GLIDE THROUGH FIELDS OF UNLIKE OBSTACLES .....	67
a) Two Types of Obstacles .....	68
b) Square Spectrum of Obstacle Strengths.....	71
c) Thermally Activated Glide .....	74
VII. COMPARISON WITH EXPERIMENTS AND DISCUSSION.....	76
VIII. SUMMARY AND CONCLUSIONS .....	87
ACKNOWLEDGEMENTS.....	90
REFERENCES.....	91
TABLE .....	98
FIGURE CAPTIONS.....	99
FIGURES .....	105

**PLASTIC DEFORMATION OF CRYSTALS:  
ANALYTICAL AND COMPUTER SIMULATION STUDIES OF  
DISLOCATION GLIDE**

*SABRI ALTINTAS*

Materials and Molecular Research Division,  
Lawrence Berkeley Laboratory and Department of Materials  
Science and Engineering, University of California,  
Berkeley, California

**ABSTRACT**

The plastic deformation of crystals is usually accomplished through the motion of dislocations. The glide of a dislocation is impelled by the applied stress and opposed by microstructural defects such as point defects, voids, precipitates and other dislocations.

The planar glide of a dislocation through randomly distributed obstacles is considered. The objective of the present research work is to calculate the critical resolved shear stress (CRSS) for athermal glide and the velocity of the dislocation at finite temperature as a function of the applied stress and the nature and strength of the obstacles.

Dislocation glide through mixtures of obstacles has been studied analytically and by computer simulation. Arrays containing two kinds of obstacles as well as square distribution of obstacle strengths are considered. The critical resolved shear stress for an array containing obstacles with a given distribution

of strengths is calculated using the sum of the quadratic mean of the stresses for the individual obstacles and is found to be in good agreement with the computer simulation data.

Computer simulation of dislocation glide through randomly distributed obstacles containing up to  $10^6$  obstacles show that the CRSS decreases as the size of the array increases and approaches a limiting value. Histograms of forces and of segment lengths are obtained and compared with theoretical predictions. Effects of array shape and boundary conditions on the dislocation glide are also studied.

Analytical and computer simulation results are compared with experimental results obtained on precipitation-, irradiation-, forest-, and impurity cluster-hardening systems and are found to be in good agreement.

## I. INTRODUCTION

The dislocation theory of plastic flow originated in 1911 through a suggestion by Prandtl<sup>1,2</sup> in explaining the mechanical hysteresis in metals in which several characteristic elements of dislocations were present. Dehlinger<sup>3</sup> was the first to consider dislocations in connection with questions of slip in a theory of recrystallization. The first, detailed theoretical discussions and the foundations of the modern dislocation theory of slip were laid by Orowan<sup>4,5</sup>, Polanyi<sup>6</sup> and Taylor<sup>7</sup> in 1934.

In an attempt to explain the discrepancy between the high theoretical estimate and the low observed value of yield stress Becker<sup>8</sup> and Orowan<sup>9</sup> suggested that the non-linear resistance to deformation derives from the flow units in the solid which are larger than the atomic size. The large internal concentrations of the applied stress produced by the flow units in plastic deformation make the thermally activated production of new flow units easy. This means in contemporary language that the rate process in plastic deformation derives from thermally activated motion of crystal dislocations over local slip plane obstacles.

The ideas of Becker and Orowan were developed and extended later by Orowan<sup>10</sup>, Kauzmann<sup>11</sup>, Seeger<sup>12</sup> and Friedel.<sup>13</sup> Since then the theoretical and experimental studies of dislocation dynamics have aimed at providing a clearer understanding and more accurate description of the plastic deformation of crystals.

The achievement of a microstructure-based theory of mechanical behavior of engineering alloys however remains still one of the central objectives of basic

research in metallurgy. This is from an engineering point of view important for two reasons: First, in order to provide a firm basis for materials selection and engineering design with real materials a predictive theory is needed. Second, an interpretive theory of mechanical behavior is needed to guide metallurgical research in the design of new alloys to meet advanced engineering needs. The complexity of the mechanical behavior of materials suggests however that a complete understanding of plastic deformation has a long way to go yet, indications are that a slight advance in understanding has a large effect on the development of new materials for specific uses.

The purpose of this thesis is to study the plastic deformation of crystals through thermally activated glide of dislocations. This problem is relevant, as discussed below, to deformation of single crystals and to yielding and initial plastic flow in engineering alloys. The objective of this research is to complete a theory of athermal and thermally activated dislocation glide through fields of microstructural barriers. The technical approach to the problem is to use computer models to directly simulate glide under precisely controlled conditions and to use the results to guide the development of predictive theories. The results of this research are used to interpret and predict the experimental data.

## II. OUTLINE OF THE PROBLEM

Following Friedel<sup>14</sup>, a typical problem in the mechanical behavior of engineering alloys sets up essentially as follows. As indicated schematically in Figure 1, an alloy consists of an aggregate of individual crystalline grains. Each of these grains is described by its composition, its crystal structure, its defect structure, its size and shape, and the nature of the grain boundaries which define its contact with adjacent grains. The defect structure includes point defects, the network of existing dislocations and the type and distribution of voids or precipitates.

To initiate plastic deformation, dislocations must be created or liberated onto slip planes bearing a resolved shear stress to sustain glide. The yield strength of imperfect crystals is determined by the resolved shear stress that is needed to move glide dislocations across their slip planes. If the applied stress is small the response is elastic with a small anelastic supplement due to bowing or recoverable motion of dislocations and to short range chemical rearrangements.

One of the most interesting and important (Kocks et al.<sup>15</sup>) theoretical problems in plastic deformation of crystals is the problem of yield and initial deformation in a grain or single crystal which is assumed to contain dislocations or active sources of dislocations, together with microstructural features which act as barriers to free dislocation glide. The bulk of prior research (summarized in references 15, 16 and 17) argues that this is a central problem in the deformation of engineering materials. Potentially mobile dislocations may generally

be assumed to exist in a metal and the native lattice resistance (Peierls - Nabarro Stress) to glide may generally be assumed small compared to that offered by such internal barriers as point defects, "forest" dislocations, precipitates, voids, and other internal stress fields.

If there are no obstacles to dislocation motion present, dislocations would sweep through crystals at infinitesimally low stresses. All real crystals, however, contain obstacles. It is the nature and distribution of such obstacles that determines the plastic behavior of metals and alloys.

The central parameters of this narrowed problem are

- 1) the resolved shear stress impelling glide,
- 2) the nature and distribution of the barriers,
- 3) the temperature and,
- 4) the nature of dislocations in the matrix.

At zero temperature the important parameter is the critical resolved shear stress for dislocation glide through the microstructure, a function of the nature and distribution of barriers. At finite temperature thermal activation may assist dislocation glide. The critical resolved shear stress is consequently less well defined, and essentially becomes the stress which allows sensible deformation within some appropriate experimental time. The problem is further complicated by the variety of possible barrier distributions and dislocation-barrier interactions, by the possibility that the barriers are mobile, and by the possibility of cross-slip of the mobile dislocations, particularly when it encounters a forest dislocation of appropriate Burger's vector and line direction.

The initial research on this problem concentrated on the motion of an isolated segment of a dislocation by cutting through or bowing around an obstacle or simple configurations of obstacles of given type. This research continues<sup>18</sup> as investigators have sought more precise solutions to more realistic dislocation obstacle models.

However, as was recognized in early research by Mott<sup>19</sup> and by Friedel<sup>13</sup>, the distribution of barriers is also of qualitative importance. The modest introduction of statistics by Friedel<sup>13</sup> for high temperature glide through a random array of point obstacles showed that the nature of activation barriers would change with applied stress even though the physical nature of the obstacles remained the same. The source of the change was a statistical tendency for the dislocation to contact a greater number of obstacles per unit length with increasing stress. Because, as the applied stress is increased, dislocations bow to smaller radii of curvature causing the average dislocation length between the obstacles to decrease. Mott and Nabarro<sup>20</sup> treated an essentially similar phenomenon in the case of diffuse barriers. This initial research led to a series of studies on the effect of statistics of the obstacle distribution on the characteristics of dislocation glide (summarized by Kocks, Argon, and Ashby in reference 15 and by Nabarro in references 16 and 17). In the case of "localized" obstacles, whose range of interaction with a dislocation is small compared to their mean spacing, the "Friedel statistics" has been used as a theoretical technique. "Mott statistics" is used for "diffuse" obstacles. The "localized" obstacles approximation appears generally more applicable to hardening by small precipitates, "forest" dislocations which interact weakly in the glide plane, small voids

and inclusions, and solute atoms in dilute concentration. The "diffuse" obstacle approximation is thought to be applicable to hardening by a higher concentration of solute atoms and by dislocations which interact strongly in the glide plane. Criteria separating the two cases have been given by Labusch<sup>21</sup> and elaborated further by Nabarro<sup>22</sup>. More theoretical progress has been made on the "localized" obstacle approximation, largely due to the observation (initially by Foreman and Makin<sup>23</sup>) that under suitable approximations this case could be set up for direct computer simulation.

### III. SPECIFIC PRIOR WORK

The plastic deformation of crystalline solids involves generally the movement of dislocations against the resistance by various types of obstacles. In many cases the obstacle has only short-range interaction with a glide dislocation and may be replaced as a point obstacle<sup>24</sup>. Furthermore, obstacles are assumed to be randomly distributed rigid barriers to dislocation motion.

Friedel<sup>13</sup> was first to introduce elementary concepts of statistics to the motion of dislocations past randomly distributed point obstacles. The bulk of the research on the problem of dislocation glide through a statistical distribution of localized microstructural obstacles addresses variants of the following basic problem<sup>25</sup>. Consider a crystal plane which is the glide plane of a dislocation. Let it contain a random distribution of microstructural barriers, which are represented as point obstacles to dislocation glide. The array is described by the statement that its points are randomly distributed and by a characteristic interobstacle spacing

$$l_s = (a)^{1/2} \quad (\text{III.1})$$

where  $a$  is the average area per point. The total area of the array is

$$A = N(l_s)^2 \quad (\text{III.2})$$

where  $N$  is the total number of points contained. We can non-dimensionalize the area by dividing through by the square of the characteristic length, so as to get

$$A^* = A/(l_s)^2 = N \quad (\text{III.3})$$

and the edge length of the square area in dimensionless form is

$$W^* = (A^*)^{1/2} = N^{1/2} \quad (\text{III.4})$$

Let a dislocation be introduced into the glide plane. We model the dislocation as a flexible string of constant line tension  $\Gamma$ , its energy per unit length, and Burger's vector of magnitude  $b$ , which is taken to lie in the glide plane. Any dependence of  $\Gamma$  on the orientation of the line or on the mutual interaction of segments of the dislocation is neglected.

The resolved shear stress,  $\tau$ , impelling glide of this dislocation may be conveniently written in dimensionless form

$$\tau^* = \frac{\tau l_s b}{2\Gamma} \quad (\text{III.5})$$

Let the dislocation under the applied stress  $\tau^*$ , encounter a configuration of point obstacles denoted by (i) (Figure 2). Between two adjacent obstacles the dislocation will take the form of a circular arc of radius

$$R = \frac{\Gamma}{\tau b} \quad (\text{III.6})$$

which can be written in dimensionless form,

$$R^* = \frac{R}{l_s} = \frac{\Gamma}{\tau b l_s} = \frac{1}{2\tau^*} \quad (\text{III.7})$$

If the distance between any two adjacent obstacles along (i) exceeds  $2R^*$  or if the dislocation line anywhere intersects itself, then the configuration (i) is transparent to the dislocation and will be mechanically bypassed. If (i) is not transparent, its mechanical stability is governed by the strength of the dislocation-

obstacle interaction.

The obstacles are assumed to be identical, circularly symmetric, localized barriers to the dislocation whose effective range of interaction ( $d$ ) is small compared to their mean separation ( $l_j$ ). They may hence be treated as point obstacles<sup>24</sup>. At the ( $k$ -th) obstacle on the ( $i$ -th) configuration the dislocation line forms the asymptotic angle  $\psi_i^k (0 \leq \psi_i^k \leq \pi)$  (Figure 2). The force,  $F_i^k$ , that the dislocation exerts on the ( $k$ -th) obstacle is simply, from Figure 2

$$F_i^k = 2\Gamma \cos\left(\frac{1}{2}\psi_i^k\right) \quad (\text{III } 8)$$

or in dimensionless form

$$\beta_i^k = \frac{F_i^k}{2\Gamma} = \cos\left(\frac{1}{2}\psi_i^k\right) \quad (\text{III } 9)$$

The dislocation-obstacle interaction is governed by a force-displacement relationship<sup>24</sup>,  $\beta(x/d)$ , the effective dimensionless point force on the dislocation as it sweeps through (or folds around<sup>26</sup>) the obstacle. The mechanical strength of the obstacle is measured by the dimensionless parameter  $\beta_c$  (or angle  $\psi_c$ ) and corresponds to the maximum force the obstacle can sustain without being cut or locally by-passed. A non-transparent line configuration of obstacles constitutes a mechanically stable barrier to the glide of a dislocation under stress  $\tau^*$  if  $\beta_i^k < \beta_c$  for all obstacles ( $k$ ) on ( $i$ ), where  $\beta_c$  is a critical pre-selected obstacle strength, or if  $\beta_i < \beta_c$  where  $\beta_i$  is taken to be the maximum of  $\beta_i^k$ . The smallest stress  $\tau^*$  at which  $\beta_i > \beta_c$  for all configurations within the array (i.e.,  $\beta_1 > \beta_c$ , where  $\beta_1$  is the minimum of  $\beta_i$ ) is the critical resolved shear stress  $\tau_c^*$ .

The dislocation line containing  $\beta_1$  is the strongest configuration within the array.

Friedel<sup>13</sup> employed essentially this model to treat thermally activated glide at high temperature and low stress. He attempted to estimate the influence of the obstacle spacing on the yield stress by assuming that the average configuration might be approximated as shown in Figure 3. He assumed that when the stress became high enough to cause the dislocation to cut the obstacles A,B,C etc., the dislocation advanced to the next set of obstacles, e.g. B, where the area swept out per obstacle,  $l_c^2$ , is approximated by

$$l_c^2 = lh \quad (\text{III.10})$$

The average segment length between the obstacles as a function of the applied stress can be calculated as follows: As required by the simple geometric relationship (Figure 3),

$$R^2 = (R - h)^2 + l^2 \quad (\text{III.11})$$

which can be written for weak obstacles, where  $h \ll 2R$

$$l^2 = 2Rh \approx 2R \frac{l_s^2}{l} \quad (\text{III.12})$$

The mean length between adjacent weak obstacles increases with increasing values of the radius of curvature and using equation (III.6) it can be approximated by

$$l = \frac{l_s}{(\tau l_s b / 2\Gamma)^{1/3}} \quad (\text{III.13})$$

Accordingly, following

$$\cos\left(\frac{\psi}{2}\right) = \frac{l}{2R} = \frac{\tau b l}{2\Gamma} = \left(\frac{\tau l_s b}{2\Gamma}\right)^{2/3} \quad (\text{III.14})$$

the flow stress  $\tau_0$  at the absolute zero temperature corresponding to a critical value of the included angle  $\psi_c$ , is given by

$$\frac{\tau_0 l_s b}{2\Gamma} = \left(\cos\frac{\psi_c}{2}\right)^{3/2} \quad (\text{III.15})$$

or, in dimensionless form, using equations (III.5) and (III.9)

$$\tau^* = (\beta)^{3/2} \quad (\text{III.16})$$

or

$$\beta = (\tau^*)^{2/3} \quad (\text{III.17})$$

and  $l^*$ , the separation between adjacent obstacles, is

$$l^* = \frac{l}{l_s} = (\tau^*)^{-1/3} \quad (\text{III.18})$$

or

$$l^* = \beta^{-1/2} \quad (\text{III.19})$$

Thus the average distance,  $l^*$ , between adjacent obstacles increases as the stress decreases.

Many detailed statistical descriptions of the motion of dislocation through random points at 0°K are given: Labusch<sup>27</sup> used the method of distribution functions which yielded functional agreement with Friedel model at low stresses. Fleischer<sup>28</sup> and Fleischer and Hibbard<sup>29</sup> suggested that the same

model might be applied to determine the critical resolved shear stress for athermal glide through a random array of weak obstacles. Their expectation seemed confirmed by the computer simulation experiments of Foreman and Makin<sup>23</sup>, who determined the critical resolved shear stress for athermal glide ( $\tau_c^*$ ) as a function of obstacle strength ( $\beta_c$ ) for random arrays of up to  $4 \times 10^4$  points. They found good agreement with equation (III.16) when the obstacle strength was small. Foreman and Makin inferred that the other features of the Friedel model, e.g. equation (III.18), were also obeyed for small obstacle strengths, but apparently did not confirm this result. Kocks<sup>36</sup> who used graphical methods to determine critical resolved shear stress obtained good agreement with the value of  $\tau_c^* \sim 0.82$  which was found by Foreman and Makin, through computer simulation for very strong obstacles ( $\beta_c \sim 1.0$ ). His method of approach was adopted by Stefansky and Dorn<sup>31</sup> and Dorn et al.<sup>32</sup> used the "unzipping" model.

Foreman and Makin<sup>33</sup> have also considered the glide through arrays of unlike obstacles and Foreman, Hirsch and Humphries<sup>34</sup> simulated the motion of a dislocation through random arrays of impenetrable point and parallel line obstacles. Scattergood and Das<sup>35</sup> developed a computer simulation method to determine the flow stress of a random distribution of circular, impenetrable obstacles. And recently, Shewfelt and Brown<sup>36</sup> extended the computer model initially developed by Foreman and Makin<sup>23</sup> to include the case in which some of the obstacles are bypassed by local climb.

The first code to simulate thermally activated glide of a dislocation was the first Berkeley code written by Klahn, Austin and Dorn<sup>37</sup>. The code successfully

simulated dislocation glide as a function of stress, obstacle strength, and temperature, assuming a simple step form for the dislocation-obstacle interaction. Zaitsev and Nadgornyi<sup>38</sup> calculated using a Monte-Carlo method the velocity of the dislocation as a function of stress and temperature. Arsenaull and Cadman used computers to calculate the force-distance profile<sup>39</sup> and the flow stress as a function of temperature for single and two types of obstacles<sup>40</sup>.

Morris and Klahn<sup>25</sup> found that fundamental statistical theorems could be used to substantially simplify the computational effort required in a simulation of thermally activated glide, and to give a precise statistical definition to the glide velocity obtained. High and low-temperature limits were identified which reduce the theoretical problem to the computation of characteristics of particular dominant configurations found in glide: the most stable, or "strength-determining" configuration in the case of low-temperature glide, and the "random" configuration in the case of high-temperature glide. At intermediate temperatures, the glide path, or sequence of configurations assumed during glide, becomes a statistical function of temperature.

Morris and Klahn<sup>41</sup> and Altintas et al.<sup>42,43</sup> used the statistical results presented in reference 25 to study thermally activated glide at low temperature, assuming an array of like obstacles and a dislocation-obstacle interaction of simple step form. The central results obtained were three:

- (1) Studying the glide velocity as a function of temperature stress and obstacle strength, they found that low temperature approximations could be used to represent the data over a wide range of conditions. Since these approx-

imations obey relatively simple equations, they may easily be used to assess the effect of the operational variables on the qualitative features of glide.

(2) Behavior in low-temperature glide is strongly influenced by the characteristics of the most stable configuration encountered during glide. These most stable configurations depend on applied stress, but are identically the configurations which determine the critical resolved shear stress as a function of obstacle strength. Detailed examination of these configurations showed that while their strengths were reasonably approximated by the Friedel relation (at low stress) their other pertinent characteristics (shape, distribution of forces, distribution of segment lengths) were not. This discrepancy is significant, since the distribution of forces is important to the kinetics of low-temperature glide and since the mean segment length is a parameter often used in attempts to fit experimental data to the point obstacle model.

(3) Simulation of crystal deformation using a model constructed by "stacking" slip planes showed features in interesting correspondence with the deformation of real crystals. At very low temperature slip concentrated on well-defined slip planes. As temperature was raised deformation became more uniform, appearing homogeneous at high temperature.

To remove discrepancies between the Friedel model and the results of computer simulation reported in reference 41, Hanson and Morris<sup>44</sup> reinvestigated the strength-determining configurations at low stresses. Using a variant of the extinction theorem of branching processes in probability theory they were able to arrive at an analytic solution for critical resolved shear stress for

infinitely large arrays. The strength, distribution of forces, and mean segment length defined by this solution were compared to the computer simulation data obtained in examining arrays containing up to  $10^4$  obstacles. Even though the derived strength and distribution of forces were in reasonable agreement with the computer simulation data the distribution of segment lengths were not. The speculation that the discrepancy might be due to finite arrays used in computer simulation called for reinvestigation.

The approach used in reference 44 was extended to treat glide through an array of obstacles having an arbitrary distribution of properties. The results were given in terms of integral equations and comparison was made with computer simulation experiments using arrays containing obstacles of two different types.<sup>45</sup>

#### IV. PURPOSE AND SCOPE OF THE PRESENT INVESTIGATION

Given the status of research at the time the present investigation started, it was believed that a realistic attempt could be made to complete a theoretical solution to the general problem of dislocation glide through distributed localized microstructural barriers. Granting that the problem to be attacked is a small and specialized part of the overall problem of mechanical behavior it is however the most realistic problem in dislocation theory which is open to detailed theoretical study. The results model the deformation of grains or crystals which may be assumed to deform by the above mechanism and are of significant value both in their own right and also for the insight they give into the influence of the statistics of microstructure on plastic deformation.

The specific objective of this dissertation is to calculate the CRSS as a function of the strength of the obstacles and to determine dislocation velocity as a function of temperature, applied stress and strength of the obstacles. The technical approach is to use a computer model to directly simulate glide under precisely controlled conditions and to compare the results with the calculations and with available experimental data.

The results can be summarized as follows: Given that the computer simulation results are very important in comparing with theoretical predictions and as a guide to further theoretical work, a systematic study was necessary to obtain accurate results using a computer code which can handle very large arrays. Most of the previous analytical predictions were suspect because they were compared with the results obtained from relatively small sized arrays.

Computer simulation of dislocation glide through randomly distributed obstacles containing up to  $10^6$  obstacles has been performed using an efficient code. (The details of the computer program is given in a later section). The results indicate that the CRSS is array size dependent and decreases as array size increases, approaching a limiting value. Histograms of forces and segment lengths are obtained and compared with theoretical predictions. Effects of array shape and boundary conditions on the dislocation glide are also studied.

Since most physically realistic systems contain obstacles of different type an extension of the analytic solutions is made to treat arrays containing arbitrary distribution of obstacle strengths and simple formulas for the CRSS and average segment length are obtained. The case in which two kinds of obstacles contribute to the strength is considered in detail and compared with existing predictions in the literature.<sup>46,47</sup> It is shown that the CRSS can be calculated using the quadratic mean of the stresses for each kind of obstacles. The results are compared with computer simulation data and show good agreement.

In crystals containing obstacles whose range of interaction with the dislocation is short compared to their spacing, thermal activation may help to overcome the barriers. Computer simulation of thermally activated dislocation glide indicates that the stress at a given velocity decreases as temperature increases. It is shown that the stress exponent of dislocation velocity varies inversely with temperature and that the obstacle strength can be estimated using the experimentally determined values. The character of the strength determining configuration changes with temperature strongly in the case of arrays containing

two-types of obstacles. The effects of temperature on the dislocation motion have important consequences with respect to deformation behavior of the crystals.

Even though the results of the Friedel model have been used in the literature to predict the strengthening of crystals<sup>48,49</sup> no detailed comparison of the model and computer simulation results with experiments have been made. In this thesis, such a task was undertaken to compare the results with experiments performed on materials which were strengthened through irradiation and precipitation. The general features of dislocation motion obtained from computer simulation showed remarkable similarities to the Transmission Electron Microscope (TEM) observations conducted by Barnes<sup>50</sup>. Recent *in-situ* High Voltage Electron Microscope (HVEM) deformation gave experimental results which made direct comparison with computer simulation data possible. Dislocation velocity measurements by Val'kovskii and Nadgornyi<sup>52</sup> on MgO crystals and *in-situ* HVEM studies by Appel et al.<sup>51</sup> gave results which were in excellent agreement with computer simulation results. Saimoto and co-workers<sup>53,54</sup> studied the deformation behavior of Cu single crystals and measured the segment length distribution. The comparison of this distribution with the one obtained from computer simulation also showed excellent agreement. In an attempt to compare the computer simulation results of Foreman and Makin<sup>33</sup>, Munjal and Ardell<sup>55</sup> made an extensive study of a precipitation hardened alloy. Even though their results were interpreted to disagree with the computer simulation data, the calculations and computer simulation of this investigation showed good agreement with the experiment.

In the next sections, we first give analytical calculations concerning the athermal and thermally activated dislocation glide through randomly distributed obstacles. The description of the computer code and comparison of the results with analytical predictions and experimental data are given in later sections.

## V. ANALYTICAL CALCULATIONS

### A. ATHERMAL GLIDE

#### 1. CRSS For Like Obstacles

A dislocation moving through an array containing randomly distributed obstacles will encounter various configurations under the influence of the applied stress. As illustrated in Figure 2, if the dislocation encounters a configuration (i) under stress  $\tau^*$ , it will take the form of a circular arc of dimensionless radius  $R^*(=1/2\tau^*)$  between adjacent obstacles. If the distance between any two adjacent obstacles along (i) exceeds  $2R^*$  or if the dislocation line anywhere intersects itself then configuration (i) is transparent to the dislocation and will be mechanically by-passed. If (i) is not transparent its mechanical stability is governed by the geometry of the configuration.

At the (k-th) obstacle on (i) the dislocation exerts a force  $\beta_i^k$  on the obstacle, where  $0 \leq \beta_i^k \leq 1$  and is given by equation (III.9). If  $\beta_c$  is the strength of the obstacle impeding glide then it is necessary for the mechanical stability of the configuration that  $\beta_i^k < \beta_c$  for all (k) on (i), or that

$$\beta_i \leq \beta_c \quad (\text{V.1})$$

where  $\beta_i$  is the maximum of the  $\beta_i^k$ . If there is to be at least one mechanically stable barrier configuration within the array for given stress  $\tau^*$  then necessarily

$$\beta_1 = \min(\beta_i) \leq \beta_c \quad (\text{V.2})$$

where  $\beta_1$  is the minimum force exerted by the dislocation on the most stable

configuration within the array.

The non-transparent configurations in a given array of obstacles are uniquely fixed by the dimensionless stress ( $\tau^*$ ) as are the forces,  $\beta_i^k$ , exerted on them<sup>41</sup>. The maximum force exerted on the most stable configuration within the array is hence specified by the function

$$\beta_1 = \beta_1(\tau^*) \quad (V.3)$$

whose inverse

$$\tau_c^* = \tau^*(\beta_1) = \tau^*(\beta_c) \quad (V.4)$$

gives the critical resolved shear stress for athermal glide through an array of obstacles of strength  $\beta_c$ .

A useful technique for locating the stable configurations within a random array of point obstacles is the "circle rolling" described in reference 41. The dislocation line between two obstacles (say,  $k-1$  and  $k$ ) is the arc of a circle of dimensionless radius  $R^* = 1/(2\tau^*)$ . If  $k-1$  and  $k$  are obstacles of strength  $\beta_c$  in a stable configuration at  $\tau^*$ , then there must be at least one obstacle ( $k+1$ ) in the area swept out by rotation of the circle counterclockwise about ( $k$ ) through an angle

$$\theta_c = \pi - \psi_c = 2 \sin^{-1}(\beta_c) \quad (V.5)$$

Since this requirement holds for all obstacles on a stable line, the line may be generated by successive circle rolling. Using this technique, Hanson and Morris<sup>44</sup> approximated the critical resolved shear stress  $\tau_c^*$  for an arbitrarily large array of obstacles of like kind by identifying a "limiting configuration"

which was necessarily at least as strong as the most stable configuration which might be encountered during glide. The derivation may be summarized as follows:

A stable dislocation configuration can be viewed as a chain of stable segments connecting the left-hand side of the array to the right-hand side. Thus a stable configuration can be constructed by beginning from the left-hand side with a single segment and searching for segments which continue the chain across the array. If the applied stress is  $\tau^*$  and the obstacle strength is  $\beta_c$ , then a segment may be continued by connecting its right-hand terminal point to any point found in the area shown in Figure 4, an area generated by rotating a circle of radius  $R^*$  through an angle  $\theta_c (= 2\sin^{-1}\beta_c)$  about the terminal point. The search area is parametrized by the coordinates  $(\theta, \phi)$  shown in Figure 4. The lines of constant  $\theta$  are generated by the leading edge of the circle as it is rotated; the lines of constant  $\phi$  are generated by the trailing edge. The range of  $\theta$  is chosen to be  $0 \leq \theta \leq \theta_c$ . The range of  $\phi$  is taken to be  $-\pi \leq \phi \leq \theta_c$ . Points of the array are distributed over this search area with density unity, hence the number of points in differential dimensionless area  $dA^*$  is simply  $dA^*$ , where

$$dA^* = (R^*)^2 \sin(\theta - \phi) d\theta d\phi = (R^*)^2 da(\theta, \phi) \quad (V.6)$$

Each point within the search area defines a possible segment continuing the chain.

The procedure for constructing a stable chain across the array by stochastically searching successive areas shown in Figure 5 bears a strong formal resemblance to the classical branching process in probability theory. The theory of

branching processes<sup>56</sup> estimates the size of the (k-th) generation of descent from a given initial event, assuming that the probability distribution for the number of descendants per parent is known. A principal result of the theory is the extinction theorem, which states that if the expected number of descendants ( $\langle n \rangle$ ) is less than unity the line of descent will necessarily terminate after a finite number of generations. In the present problem it follows that  $\tau^*$  and  $\theta_c$  must be such that the search area  $A^*$  of Figure 4 is greater than unity if it is to be possible to construct a stable chain across an array of arbitrarily large size.

The stable configurations of the dislocation are, however, additionally constrained in that the dislocation line cannot intercept itself. A necessary (though not sufficient) condition<sup>44</sup> is that the expected value of the coordinate  $\phi$  of the points used to extend the chain must be zero. Since the average value of  $\phi$  over the search area is less than zero (at least for  $\theta_c < \pi$ ) the condition  $\langle \phi \rangle = 0$  constrains the manner in which points may be selected from among those contained in  $A^*$ ; points may only be used in subsets which have zero  $\langle \phi \rangle$ .

Given these considerations, the points used to define the segments which extend a chain across the array are chosen according to a distribution function  $f(\theta, \phi)$ ,  $0 \leq f \leq 1$ , which gives the fraction of the points found in  $da(\theta, \phi)$  in an arbitrarily large sequence of searches of areas like  $A^*$  which are used to form the segments of a stable chain. The function  $f(\theta, \phi)$  must satisfy at least the two constraints :

$$\langle n \rangle = (R^*)^2 \int_a f(\theta, \phi) da(\theta, \phi) > 1 \quad (\text{V.7})$$

and

$$\langle \phi \rangle = (R^*)^2 \int_a \phi f(\theta, \phi) da(\theta, \phi) = 0 \quad (\text{V.8})$$

For given values of  $\langle n \rangle$  and the obstacle strength  $\theta_c$  it may be shown (Appendix to Reference 44) that the radius  $R^*$  is minimized ( $\tau^*$  maximized) under the constraint (V.8) if we choose

$$\begin{aligned} f(\theta, \phi) &= 1 & -\phi_0 \leq \phi \leq \theta_c \\ &= 0 & \phi \leq \phi_0 \end{aligned} \quad (\text{V.9})$$

where  $\phi_0$  is the solution of the equation

$$\langle \phi \rangle = \int_{a_0} \phi da(\theta, \phi) = \int_{-\phi_0}^{\theta_c} \phi da(\phi) = 0 \quad (\text{V.10})$$

with the integral taken over the area  $a_0$  shown in Figure 5.

If we now set

$$\begin{aligned} \langle n \rangle &= 1 \\ \langle \phi \rangle &= 0 \end{aligned} \quad (\text{V.11})$$

and choose  $f(\theta, \phi)$  according to equation (V.9), we obtain a value of  $\tau^*$ ,  $\tau_0^*$ , which is necessarily larger than the stress necessary to pass the most stable chain which might be constructed across an arbitrarily large array of obstacles of strength  $\theta_c$ . Hence

$$\tau_0^* = \frac{1}{2} \left[ \int_{a_0} da(\theta, \phi) \right]^{1/2} > \tau_c^*(\theta_c) \quad (\text{V.12})$$

places an upper limit on the critical resolved shear stress.

To compute the properties of the limiting configuration we require the function  $\phi_0(\theta_c)$  determined by equation (V.10). The differential area

$$da(\phi) = \int_{-\phi_0}^{\theta_c} d\mu(\theta, \phi) \quad (\text{V.13})$$

is (Figure 6)

$$da(\phi) = \begin{cases} 1 - \cos(\theta_c - \phi), & 0 \leq \phi \leq \theta_c \\ \cos\phi - \cos(\theta_c - \phi), & \theta_c - \pi \leq \phi \leq 0 \\ \cos\phi + 1, & -\pi \leq \phi \leq \theta_c - \pi \end{cases} \quad (\text{V.14})$$

Since from equation (V.10)

$$\int_{-\phi_0}^{\theta_c} \phi da(\phi) = 0 \quad (\text{V.10})$$

and using regions I and II (Figure 6)

$$\int_0^{\theta_c} \phi(1 - \cos(\theta_c - \phi)) d\phi + \int_{-\phi_0}^0 \phi(\cos\phi - \cos(\theta_c - \phi)) d\phi = 0$$

for  $\theta_c \geq \phi \geq \theta_c - \pi$  (V.15)

we obtain

$$\frac{1}{2}\theta_c^2 - \cos\phi_0 - \phi_0\sin\phi_0 + \cos(\theta_c + \phi_0) + \phi_0\sin(\theta_c + \phi_0) = 0$$

using

$$\sin x \approx x - \frac{x^3}{3!} + \frac{x^5}{5!}$$

and

$$\cos x \approx 1 - \frac{x^2}{2!} + \frac{x^4}{4!}$$

we get

$$\theta_c^4 - 6\theta_c^2\phi_0^2 - 8\theta_c\phi_0^3 = 0 \quad (\text{V.16})$$

which can be solved for  $\phi_0(\theta_c)$ .

Similarly, from equation (V.12)

$$(2\tau_0^*)^2 = \int_a d\sigma(\theta, \phi) \quad (\text{V.17})$$

or using (V.14)

$$(2\tau_0^*)^2 = \theta_c + \sin\phi_0 - \sin(\theta_c + \phi_0) \quad (\text{V.18})$$

or, approximately

$$(2\tau_0^*)^2 = \frac{\theta_c}{6} \left[ \theta_c^2 + 3\theta_c\phi_0 + 3\phi_0^2 \right] \quad (\text{V.19})$$

The solution of the equation (V.16) using conventional methods<sup>57</sup> gives

$$\begin{aligned} \phi_0 &= \frac{\theta_c}{4} \left\{ (3 + 2\sqrt{2})^{1/3} + (3 - 2\sqrt{2})^{1/3} - 1 \right\} \\ \phi_0 &\approx 0.3388 \theta_c \end{aligned} \quad (\text{V.20})$$

Putting (V.20) into (V.19), we obtain

$$(\tau_0^*)^2 \approx 0.7870 (1/2\theta_c)^3 \quad (\text{V.21})$$

which may be rewritten for weak obstacles

$$\tau_0^* = 0.8871 (\beta_0)^{3/2} \quad (\text{V.22})$$

or

$$\beta_0 = 1.083 (\tau_0^*)^{2/3} \quad (\text{V.23})$$

which differs from the Friedel relation (equation III.16) through a multiplicative constant. The agreement in functional form is not fortuitous, since virtually any technique for searching an array by rolling or bowing a circle of radius  $R^*$  through a small angle  $\theta_c$  leads to a search area proportional to  $(R^*)^2 \theta_c^3$ , and will, hence, yield an equation which differs from Friedel relation only through a multiplicative result. Regarding the disagreement, note that the value in equation (V.22) is an upper bound on the value of  $\tau_c^*$  in an array of arbitrarily large size, which lies below the Friedel limit by  $\sim 11\%$ .

The normalized distribution of forces along the limiting configuration may be computed from the relation

$$\rho(\theta, \tau^*) d\theta = (R^*)^2 \int_{\phi}^{\phi} da(\theta, \phi) \quad (\text{V.24})$$

where  $\rho(\theta, \tau^*)$  is the distribution of angles  $\theta$ , in the limiting configuration at stress  $\tau_0^*$ . Using equation (V.14) and assigning appropriate limits to the integral, we obtain

$$\begin{aligned} \rho(\theta, \tau^*) &= R^{*2} [1 - \cos(\theta + \phi_0)], & \phi_0 \leq \pi - \theta_c \\ &= 2R^{*2}, & \theta_c \geq \theta \geq \pi - \phi_0, \phi_0 \geq \pi - \theta_c \\ &= R^{*2} [1 - \cos(\theta + \phi_0)], & \pi - \phi_0 \geq \theta \geq 0, \phi_0 \geq \pi - \theta_c \end{aligned} \quad (\text{V.25})$$

For the range of interest here,  $0 \leq \beta_0 \leq 0.7$ ,  $\phi_0$  is less than  $(\pi - \theta_c)$ , and only the first term is important. Since  $\beta = \sin(1/2\theta_c)$ ,

$$\begin{aligned} \rho(\beta, \tau^*) &= \rho(\theta, \tau^*) \frac{d\theta}{d\beta} \\ &= 2R^{*2} \left\{ (1 - \beta^2)^{-1/2} [1 - (1 - 2\beta^2)\cos\phi_0] + 2\beta\sin\phi_0 \right\} \end{aligned} \quad (\text{V.26})$$

where we have assumed  $\phi_0 \leq \pi - \theta_c$ . This distribution is, of course, sharply cut off at  $\beta_0$ . It is uniquely fixed by either  $\tau_0^*$  or  $\beta_0$ , since either is sufficient to determine the radius  $R^*$ , the angle  $\phi_0$ , and the maximum  $\beta_0$ .

In the limit of small obstacle strength (or, equivalently, low stresses) the density of forces takes the form

$$\rho(\beta, \beta_0) \approx [(\frac{\beta}{\beta_0} + k_1)^2 / (k_2^2 l_0)] \quad (\beta < \beta_0 \ll 1) \quad (V.27)$$

where  $k_1 = 0.3388$  and  $k_2 = 0.8871$ . Note that this limiting distribution can be recast in the form

$$\rho(\frac{\beta}{\beta_0}) = [(\frac{\beta}{\beta_0} + k_1)^2 / k_2^2] \quad (\frac{\beta}{\beta_0} \leq 1, \beta_0 \ll 1) \quad (V.28)$$

which is independent of  $\tau^*$  or  $\beta_0$ .

The distribution of the angles  $\phi$  can also be derived from equation (V.14) and is given by

$$\begin{aligned} \rho(\phi) &= R^{*2}[1 - \cos(\theta_c - \phi)], & 0 \leq \phi \leq \theta_c \\ &= R^{*2}[\cos\phi - \cos(\theta_c - \phi)], & \theta_c - \pi \leq \phi \leq 0 \\ &= R^{*2}[\cos\phi + 1], & -\pi \leq \phi \leq \theta_c - \pi \end{aligned} \quad (V.29)$$

The normalized distribution of segment lengths,  $\rho(l^*, \tau^*)$ , may be found by expressing  $l^*$  as a function of  $\theta$  and  $\phi$  over which  $l^*$  is constant. The result is for  $\phi_0 \leq \pi - \theta_c$ ,

$$\begin{aligned} \rho(l^*, \tau^*) &= l^* \theta_c & 0 \leq l^* \leq l' \\ &= l^*(\theta_c + \phi_0 - 2\sin^{-1}(l^*/2R^*)) & l' \leq l^* \leq l'' \end{aligned} \quad (V.30)$$

where

$$\begin{aligned}
 l' &= 2R^* \sin\left(\frac{\phi_0}{2}\right) \\
 \bar{l}' &= 2R^* \sin\left(\frac{\theta_c + \theta_0}{2}\right)
 \end{aligned}
 \tag{V.31}$$

The mean segment length,  $\langle l'(\tau^*) \rangle$ , is the quantity which is usually compared to the Friedel relation (III.18). Using equation (V.30)

$$\begin{aligned}
 \langle l'(\tau^*) \rangle &= \int_0^{\tau^*} l' \rho(l', \tau^*) dl' \\
 &= (2/3) (2R^*)^3 \left\{ \cos\left(\frac{\phi_0}{2}\right) \left[ 1 - \frac{1}{3} \cos^2\left(\frac{\phi_0}{2}\right) \right] \right. \\
 &\quad \left. - \cos\left(\frac{\theta_c + \phi_0}{2}\right) \left[ 1 - \frac{1}{3} \cos^2\left(\frac{\theta_c + \phi_0}{2}\right) \right] \right\}
 \end{aligned}
 \tag{V.32}$$

When  $\tau^*$  or  $\theta_c$  is small,  $\langle l'(\tau^*) \rangle$  is approximated by the asymptotic relation

$$\begin{aligned}
 \langle l'(\tau^*) \rangle &= 0.764(\theta_c/2)^{-1/2} \\
 &= 0.734(\tau^*)^{-1/3}
 \end{aligned}
 \tag{V.33}$$

or

$$\langle l'(\tau^*) \rangle = 0.764(\beta_c)^{-1/2}
 \tag{V.34}$$

which suggests that the Friedel relation (equation III.19) overestimates the asymptotic  $\langle l'(\tau^*) \rangle$ , by about 27 %. The two relations are, however, identical in the functional form.

The comparison of the results outlined above to the computer simulation data showed<sup>44</sup> while the mean segment length, the distribution of forces gave good fit, the density function  $\rho(l', \tau^*)$  calculated from equation (V.30) did not correctly reproduce the shape of the empirical distribution, which was determined by compiling the segment lengths found along the most stable configuration in each of the 10 arrays of  $10^4$  points at  $\tau^* = 0.1$ . It was not

clear whether this discrepancy principally resulted from the approximations involved in the theoretical model or from the finite size of the arrays used to generate the empirical distribution.

Recently, Labusch<sup>58</sup> criticized the model by Hanson and Morris<sup>44</sup> on the grounds that the theoretical link length distribution and the one found in computer simulation tests disagreed, and that the function  $f(\phi)$  was not determined correctly. The method of calculation used by Labusch<sup>58</sup> is similar to the entropy calculation used in Statistical Thermodynamics.

He uses same parameters as shown in Figure 4. The search area  $A^*$  is divided into  $L$  elements  $dA_{l(k)}^*$  with the coordinates  $\phi_l$  and  $\theta_l$ . The test lines of  $K$  links is constructed stepwise according to the following scheme: on arriving at point  $(k)$  the next link is drawn as a circular arc of radius  $R^*$  with its end point in an area element  $dA_{l(k)}^*$  in the  $(k)$ -th step. A test line is stable only if a pinning point exists in each of the area elements  $dA_{l(k)}^*$ . The probability that a given test line is stable is

$$\prod_{k=1}^K dA_{l(k)}^* \quad (V.35)$$

If  $n_l$  is the frequency of occurrence of the values of  $(l)$  among  $(k)$  links, this probability can be written as

$$\prod_{k=1}^K dA_{l(k)}^* = \prod_{l=1}^L (dA_l^*)^{(n_l)} \quad (V.36)$$

subject to the condition

$$\sum_{l=1}^L n_l = K \quad (V.37)$$

and to the quasi - straightness condition

$$\sum_{l=1}^L n_l \phi_l = 0 \quad (\text{V.38})$$

The number of different test lines that can be constructed from a given set of links is given by the number of distinguishable permutations of the sequence of links which is equal to

$$\frac{N!}{\prod_{l=1}^L (n_l!)} \quad (\text{V.39})$$

Thus, the expectation value of the total number of stable lines is

$$P = \frac{N!}{\prod_{l=1}^L n_l!} \prod_{l=1}^L (dA_l)^{n_l} \quad (\text{V.40})$$

The solution of this equation subject to the constraints (V.37) and (V.38) can be calculated from the equation

$$\frac{\partial}{\partial n_l} (\ln P + \gamma \sum_l n_l \phi_l + \lambda \sum_l n_l) = 0 \quad (\text{V.41})$$

from which the "partition function" can be found to be

$$z = \int_A e^{\gamma \phi} dA \quad (\text{V.42})$$

which gives

$$z = 4R^{*2} \frac{\exp(\gamma \theta) - 1}{4\gamma^3} \quad (\text{V.43})$$

where the parameter  $\gamma$  is given by

$$\gamma = 2.8214/\theta \quad (\text{V.44})$$

For the critical condition,  $z=1$ , the critical resolved shear stress obtained by Labusch is,

$$\tau_L^* = 1.186 \beta_0^{3/2} \quad (\text{V.45})$$

$$\beta_0 = 0.892(\tau_L^*)^{2/3} \quad (\text{V.46})$$

which is  $\approx 12\%$  higher than the Friedel limit (equation (III.16)).

In an attempt to take the problem of the degeneracy of the lines into account Labusch corrected his result to get

$$\tau_L^* = 0.954 \beta_0^{3/2} \quad (\text{V.47})$$

which differs from equation (III.16) by 5%.

The normalized distribution of forces on pinning points is

$$\rho_L(\beta) = \frac{\exp(2\gamma\sin^{-1}\beta)}{(\sqrt{1-\beta^2}) \int_0^{\beta_c} (\exp(2\gamma\sin^{-1}\beta) / \sqrt{1-\beta^2}) d\beta} \quad (\text{V.48})$$

$$0 \leq \beta \leq \beta_c$$

In the limit of small  $\beta_c$

$$\rho_L(\beta) = \frac{2\gamma\beta}{\exp(2\gamma\beta_c) - 1} \exp(2\gamma\beta) \quad (\text{V.49})$$

The distribution of angles  $\phi$  is given by

$$\rho_L(\phi) = k_0 \exp(\gamma\phi) \cdot \begin{cases} \sin^2(\frac{\theta-\phi}{2}), & 0 \leq \phi \leq \theta \\ \sin^2(\frac{\theta-\phi}{2}) - \sin^2(\frac{\phi}{2}), & -\pi \leq \phi \leq 0 \\ 1 - \sin^2(\frac{\phi}{2}), & -\pi \leq \phi \leq \theta - \pi \end{cases} \quad (\text{V.50})$$

where normalizing factor  $k_0$  is chosen so that

$$\int_{-\pi}^{\theta} f(\phi) d\phi = 1$$

The distribution of segment lengths in normalized form is given by

$$\rho_L(l^*) = \frac{l^* \exp(-2\gamma \sin^{-1}(\frac{l^*}{2R^*}))}{\int l^* \exp(-2\gamma \sin^{-1}(\frac{l^*}{2R^*})) dl^*} \quad (V.51)$$

which depends on the pinning strength through  $\gamma$  and on the applied stress through  $R^*$ . For small obstacle strengths, (V.51) can be written as

$$\rho_L(l^*) = \frac{\gamma^2}{R^{*2}} l^* \exp(-\gamma l^*/R^*) \quad (V.52)$$

The average value of  $l^*$  is given by

$$\langle l_L^* \rangle = \frac{2R^*}{\gamma} = 0.7088(R^*\theta)$$

Since  $R^* = \frac{1}{2\tau^*}$  and  $\theta \approx 2\beta$ ,

$$\begin{aligned} \langle l_L^* \rangle &= 0.7088 \frac{\beta}{\tau^*} \\ &= 0.5976\beta^{-1/2} \end{aligned} \quad (V.53)$$

Using equation (V.46) for  $\beta$ , we obtain

$$\langle l_L^* \rangle = 0.6326(\tau^*)^{-1/3} \quad (V.54)$$

or in corrected form

$$\langle l_L^* \rangle = 0.7314(\tau^*)^{-1/3} \quad (V.55)$$

which is 27% lower than the Friedel limit.

In an attempt to characterize the first stable configuration encountered during glide Landau<sup>59</sup> obtained the following results for the average angle of attack  $\langle \theta \rangle$  and the average segment length  $\langle l^* \rangle$

$$\langle \theta \rangle = 0.831 \left( \frac{3}{R^*} \right)^{1/3} \quad (\text{V.56})$$

and

$$\langle l^* \rangle = 0.979 (3R^*)^{1/3} \quad (\text{V.57})$$

and the ratio

$$\frac{\langle \theta \rangle}{\langle l^* \rangle} = \frac{0.85}{R^*} \quad (\text{V.58})$$

However, for a quasi-straight dislocation in a large array, using the relationships

$$\lambda_i = \frac{l_i^*}{R^*} \quad (\text{V.59})$$

where  $\lambda_i$  is the angle corresponding to the circle length of  $l_i^*$  between two obstacles, and assuming straight, long dislocation,

$$\sum_i \lambda_i = \sum_i \theta_i \quad (\text{V.60})$$

and so

$$\sum_i \theta_i = \frac{1}{R^*} \sum_i l_i \quad (\text{V.61})$$

or

$$\frac{\langle \theta \rangle}{\langle l^* \rangle} = \frac{1}{R^*} \quad (\text{V.62})$$

The discrepancy between equations (V.62) and (V.58) suggests that the solution by Landau<sup>59</sup> is probably in error. The average values of the angle  $\langle \theta \rangle$  and segment length  $\langle l^* \rangle$  can also be obtained from equations (V.25) and (V.30) and we obtain

$$\langle \phi \rangle = 0.924(R^*)^{-2/3} \quad (\text{V.63})$$

and

$$\langle l^* \rangle = 0.924(R^*)^{1/3} \quad (\text{V.64})$$

giving

$$\frac{\langle l^* \rangle}{\langle \theta \rangle} = R^* \quad (\text{V.65})$$

exactly the same result as equation (V.62). The ratio of  $\langle l^* \rangle$  to  $\langle \theta \rangle$  for Labusch's solution<sup>58</sup> gives also the correct result.

## 2. CRSS For Unlike Obstacles

Most realistical systems contain more than one type of obstacles, as for example the precipitate size, shape or location may vary, hence changing the interaction force between obstacles and dislocations. Other systems may contain more than one type of strengthening barriers, e.g. solute atoms in a precipitation hardened alloy.

The extension of the theory<sup>45</sup> as outlined in the previous section to the case when obstacles are not identical can be treated by modifying the procedure for generation of the limiting configuration. Let a stable line be constructed left to right across an array which contains randomly distributed obstacles of P dis-

tinct types, labelled  $i = 1, 2, 3, \dots, P$ , having fractions  $x_i$  and strengths  $\beta_i$ . Again using the constraints (V.7) and (V.8) we obtain

$$(\tau_0^*)^2 = \frac{1}{4} \sum_i x_i a_i^0 \quad (\text{V.66})$$

$$0 = \sum_i x_i a_i^0 \langle \phi \rangle_i \quad (\text{V.67})$$

where  $\tau_0^*$  is the strength of the limiting configuration (an upper limit on  $\tau_i^*$ ),  $a_i^0$  is the subarea of  $a_i$  over which  $-\pi \leq \phi \leq \theta$ , and  $\langle \phi \rangle_i$  is the average value of  $\phi$  over  $a_i$ . The fraction of obstacles of type (i) on the strongest configuration can easily be calculated and is given by

$$c_i = x_i a_i^0 (R^*)^2 \quad (\text{V.68})$$

The computation of the distribution of forces in the limiting configuration is straight-forward given the discussion in the previous section. The distribution of forces on obstacles of type i is specified by the density function

$$\begin{aligned} \rho_i(\beta) &= (a_i^0 (R^*)^2)^{-1} \rho(\beta, \tau^*), & 0 \leq \beta \leq \beta_i, \\ &= 0, & \beta > \beta_i, \end{aligned} \quad (\text{V.69})$$

where  $\rho(\beta, \tau^*)$  is the density function given by equation (V.26). The density of forces in the limiting configuration is hence

$$\rho(\beta) = \sum_i c_i \rho_i(\beta) = \rho(\beta, \tau^*) \sum_i x_i h_i(\beta) \quad (\text{V.70})$$

where  $h_i(\beta)$  is a weighting function and is given by

$$h_i(\beta) = \begin{cases} 1 & \text{if } \beta \leq \beta_i \\ 0 & \text{if } \beta > \beta_i \end{cases} \quad (\text{V.71})$$

With similar arguments the average segment length along the configuration can be calculated through

$$\langle l^* \rangle = \sum_i x_i \langle l^*(\tau^*) \rangle_i, \quad (\text{V.72})$$

where the function  $\langle l^*(\tau^*) \rangle_i$  is given by equation (V.30).

Using lower order series expansion to the area  $a_i^0$  obtained from equation (V.14)

$$a_i^0 = (R^*)^2 [\theta_i + \sin \phi_0 - \sin(\theta_i + \phi_0)] \quad (\text{V.73})$$

we obtain

$$a_i^0 = \frac{\theta_i}{6} [\theta_i^2 + 3\theta_i \phi_0 + 3\phi_0^2] \quad (\text{V.74})$$

The series expansions of equations (V.66) and (V.67) are then

$$24(\tau_0^*)^2 = \sum_i x_i \theta_i^3 + 3 \sum_i x_i \theta_i^2 \phi_0 + 3 \sum_i x_i \theta_i \phi_0^2 \quad (\text{V.75})$$

and

$$0 = \sum_i x_i \theta_i^4 - 6 \sum_i x_i \theta_i^2 \phi_0^2 - 8 \sum_i x_i \theta_i \phi_0^3 \quad (\text{V.76})$$

To obtain a closed form solution of the critical resolved shear stress for multiple obstacles as a function of  $x_i$  and  $\theta_i$ , we approximate  $\phi_0$  from equation (V.76) as

$$\phi_0^2 \approx \frac{\sum_i x_i \theta_i^4}{6 \sum_i x_i \theta_i^2} \quad (\text{V.77})$$

As a function of obstacle fraction  $x_i$  and strength  $\beta_i$ , the CRSS for multiple

obstacles is approximately given by

$$(\tau_0^*)^2 \approx \frac{1}{3} \sum_i x_i \beta_i^3 + \frac{1}{2} \phi_0 \sum_i x_i \beta_i^2 + \frac{1}{4} \phi_0^2 \sum_i x_i \beta_i, \quad (\text{V.78})$$

where

$$\phi_0^2 \approx \frac{2}{3} \frac{\sum_i x_i \beta_i^4}{\sum_i x_i \beta_i^2} \quad (\text{V.79})$$

Inserting (V.79) into (V.78) gives

$$(\tau_0^*)^2 = \frac{1}{3} \sum_i x_i \beta_i^3 + \frac{1}{\sqrt{6}} \left( \left( \sum_i x_i \beta_i^2 \right) \left( \sum_i x_i \beta_i^4 \right) \right)^{1/2} + \frac{1}{6} \sum_i x_i \beta_i \left\{ \frac{\sum_i x_i \beta_i^4}{\sum_i x_i \beta_i^2} \right\} \quad (\text{V.80})$$

The fraction of obstacles of type  $i$  on the strongest configuration is calculated from equation (V.68) and (V.74) as

$$c_i = \frac{8x_i \beta_i + 12\phi_0 x_i \beta_i^2 + 6\phi_0^2 x_i \beta_i}{24(\tau_0^*)^2} \quad (\text{V.81})$$

The lower order series expansion for the average segment length can be calculated as follows:

From equation (V.72)

$$\langle l^* \rangle = \sum_i x_i \langle l(\tau^*) \rangle_i$$

where  $\langle l(\tau^*) \rangle_i$  is approximated from equation (V.30) as

$$\langle l(\tau^*) \rangle_i = \frac{(R^*)^3}{12} \left\{ (\theta_i + \phi_0)^4 - \phi_0^4 \right\} \quad (\text{V.82})$$

and

$$\langle l^* \rangle = \frac{(R^*)^3}{12} (\sum_i x_i \theta_i^4 + 4 \sum_i x_i \theta_i^3 \phi_0 + 6 \sum_i x_i \theta_i^2 \phi_0^2 + 4 \sum_i x_i \theta_i \phi_0^3) \quad (V.83)$$

or approximately

$$\langle l^* \rangle \approx \frac{4(R^*)^3 \phi_0}{12} (3 \sum_i x_i \theta_i^2 \phi_0 + \sum_i x_i \theta_i^3 + \sum_i x_i \theta_i \phi_0^2) \quad (V.84)$$

or using equation (V.75)

$$\sum_i x_i \theta_i^3 + 3 \sum_i x_i \theta_i^2 \phi_0 = 24(\tau_0^*)^2 - 3 \sum_i x_i \theta_i \phi_0^2 \quad (V.85)$$

to get

$$\langle l^* \rangle = \frac{4(R^*)^3 \phi_0}{12} (24\tau_0^3 - 2 \sum_i x_i \theta_i \phi_0^2) \quad (V.86)$$

which gives in terms of  $\beta_i$ ,

$$\langle l^* \rangle = \left( \frac{\phi_0}{\tau_0} \right) - \frac{1}{6} \left( \frac{\phi_0}{\tau_0} \right)^3 \sum_i x_i \beta_i \quad (V.87)$$

#### a) CRSS for two types of obstacles

If we have two kinds of obstacles ( strong and weak ) distributed randomly and having strengths  $\beta_s$  and  $\beta_w$  and fractions  $x_s$  and  $x_w$ , the formulas developed above can easily be applied. For the CRSS we obtain from equation (V.80)

$$(\tau_0^*)^2 = (\tau_s^*)^2 x_s + (\tau_w^*)^2 x_w + \text{small terms} \quad (V.88)$$

where

$$\tau_s^* = k \beta_s^{3/2} \quad (V.89)$$

and

$$\tau_w^* = k\beta_w^{3/2} \quad (V.90)$$

where k is a constant.  $\tau_s^*$  and  $\tau_w^*$  are stresses if the arrays contained only strong or weak obstacles, respectively.

There have been empirical formulas in the literature, developed for the superposition of two mechanisms. First one is due to Koppelaar and Kuhlmann-Wilsdorf<sup>47</sup> and requires that the squares of the stresses should be added, i.e.

$$\tau^2 = \tau_s^2 + \tau_w^2 \quad (V.91)$$

or in dimensionless terms

$$(\tau^*)^2 = (\tau_s^*)^2 x_s + (\tau_w^*)^2 x_w \quad (V.92)$$

which is almost the same as obtained in this study.

The second formula is given by Kocks<sup>46</sup> and was obtained for the special case of arrays containing a lot of weak and a few strong obstacles. In this case, the stress due to weak obstacles has been treated as a friction stress and simple addition of stresses is required, i.e.

$$\tau^* = \tau_s^* \sqrt{x_s} + \tau_w^* \sqrt{x_w} \quad (V.93)$$

$$\text{if } x_w \gg x_s \text{ and } \tau_s^* \gg \tau_w^* \text{ (or } \beta_s^* \gg \beta_w^*) \quad (V.94)$$

The above constraints are necessary for the above formula to hold, since if

$\tau_s^* = \tau_w^*$  and  $x_s = x_w = \frac{1}{2}$  we get

$$\tau^* = \sqrt{2}\tau_s^*$$

which is unreasonable.

**b) CRSS for arbitrary distribution of obstacle strengths**

To obtain CRSS for crystals containing arbitrary distribution of obstacle strengths the equations (V.66) and (V.67) can be used in principle, but to get closed form formulas we approximate the CRSS for weak obstacles by,

$$(\tau^*)^2 \approx k^2 \sum_i x_i \beta_i^3 \quad (V.95)$$

or

$$(\tau^*)^2 = \sum_i x_i (\tau_i)^2 \quad (V.96)$$

Since the distribution of obstacle strengths is not a priori known and has to be determined independently, we consider two simple cases of strength distributions. However, the technique used here could be extended to any type of distribution.

The first case to be considered is the distribution of angles, which has also been empirically studied by Foreman and Makin<sup>33</sup> through computer simulation. The obstacle strength is given by the critical angle  $\psi_c$  and square spectrum of angles is assumed (Figure 7). This distribution is characterized either by  $\psi_{min}$  and  $\psi_{max}$  or by the mean value  $\psi_m$  and the width of the distribution  $\psi_w$ , and is given by

$$\rho(\psi) = \frac{1}{\psi_{max} - \psi_{min}} \quad (V.97)$$

We use for the stresses  $\tau_i$  in equation (V.96) the following formulas, depending upon the range of  $\psi_i$ . For strong obstacles we use the empirically found

formula<sup>33</sup>

$$\tau_i^* = 0.82 \cos \frac{\psi_i}{2} \quad \text{for } \psi_i < \frac{\pi}{2} \quad (\text{V.98})$$

and

$$\tau_i^* = k \cos^{\frac{3}{2}} \left( \frac{\psi_i}{2} \right) \quad \text{for } \psi_i > \frac{\pi}{2} \quad (\text{V.99})$$

Converting the equation (V.96) into integral form and using equations (V.97), (V.98), and (V.99) we obtain the CRSS for the square spectrum of angles

$$\begin{aligned} (\tau^*)^2 &= \frac{(0.82)^2}{2\psi_n} \left[ \psi_n + 2\cos\psi_m \sin \frac{\psi_n}{2} \right] \quad \text{for } \psi_m < \frac{\pi}{2} \\ &= \frac{k^2}{\psi_n} \left[ 3\cos \frac{\psi_m}{2} \sin \frac{\psi_n}{4} + \frac{1}{3} \cos \left( \frac{3}{2}\psi_m \right) \sin \left( \frac{3}{4}\psi_n \right) \right] \quad \text{for } \psi_m > \frac{\pi}{2} \end{aligned} \quad (\text{V.100})$$

where

$$2\psi_n = \psi_{min} + \psi_{max}$$

and

$$\psi_m = \psi_{max} - \psi_{min}$$

The second case considered here is the square spectrum of obstacle strengths  $\beta_i$  (Figure 8). In this case, the distribution function is given by

$$\rho(\beta) = \frac{1}{\beta_{max} - \beta_{min}} \quad (\text{V.101})$$

For the stresses  $\tau_i$ , we use the equivalent forms of equations (V.98) and (V.99) using the relation  $\beta_i = \cos\left(\frac{\psi_i}{2}\right)$ .

Using the equations (V.96) and (V.101) we obtain the CRSS for the square spectrum of strengths ( $\beta_i$ )

$$\begin{aligned} (\tau^*)^2 &= (0.82)^2 \left[ \beta_m^2 + \frac{1}{12} \beta_w^2 \right] \quad \text{for } \beta_m > 0.7 \\ &= k^2 \left[ \beta_m^3 + \frac{1}{4} \beta_m \beta_w^2 \right] \quad \text{for } \beta_m < 0.7 \end{aligned} \quad (\text{V.102})$$

where the average strength  $\beta_m$  and the width of the distribution  $\beta_w$  are given by

$$2\beta_m = \beta_{\min} + \beta_{\max}$$

and

$$\beta_w = \beta_{\max} - \beta_{\min}$$

The CRSS obtained for the square spectrum of obstacle strengths can be written in terms of angles  $\psi_m$  and  $\psi_w$ , using the definitions

$$\beta_m = \frac{1}{2} \left( \cos \frac{\psi_{\min}}{2} + \cos \frac{\psi_{\max}}{2} \right) = \cos \frac{\psi_m}{2} \cos \frac{\psi_w}{4} \quad (\text{V.103})$$

and

$$\beta_w = \cos \frac{\psi_{\min}}{2} - \cos \frac{\psi_{\max}}{2} = 2 \sin \frac{\psi_m}{2} \cos \frac{\psi_w}{4} \quad (\text{V.104})$$

we obtain

$$\begin{aligned} (\tau^*)^2 &= \frac{(0.82)^2}{3} \left[ 1 + \cos \psi_m \cos \frac{\psi_w}{2} + \frac{1}{2} \left( \cos \psi_m + \cos \frac{\psi_w}{2} \right) \right] \quad \text{for } \psi_m < \frac{\pi}{2} \\ &= \frac{k^2}{4} \left[ 2 \cos \frac{\psi_m}{2} \cos \frac{\psi_w}{4} \right] \left[ 1 + \cos \psi_m \cos \frac{\psi_w}{2} \right] \quad \text{for } \psi_m > \frac{\pi}{2} \end{aligned} \quad (\text{V.105})$$

The consistency of the formulas can be checked by, for example, letting  $\beta_w$  go to zero, giving only one type of obstacle, which gives for weak obstacles,

from equation (V.102)

$$(\tau^*)^2 = k^2 \beta_m^3 = k^2 \beta_c^3$$

which is equivalent to the theoretical predictions

## B. THERMALLY ACTIVATED GLIDE

Recently, Zaitsev and Nadgornyi<sup>(61)</sup> discussed the problem of waiting time calculation for computer simulation of thermally activated motion and identified three different methods:

- 1) the accumulated time method<sup>37, 61</sup>
- 2) the waiting time method<sup>60, 62</sup>
- 3) the residence time method<sup>25, 41, 42</sup>

and concluded that the methods 2 and 3 are equivalent and the empirical method 1 is a good approximation. They also indicated that the residence time method can have some advantages under the simulation of dislocation motion through randomly distributed point obstacles. To avoid confusion and to overcome the difficulties of comparing the results obtained using different methods, an account of the statistics employed in this study will be given.

The assumptions and basic equations are summarized in Table 1. The obstacles are randomly distributed and the dislocation is allowed to move through them, starting from the bottom as a straight configuration. Let the dislocation at an intermediate position be pressed against a line configuration of point obstacle by the resolved shear stress (Figure 2). If configuration (i) is mechanically stable it must be passed by thermal activation. We ignore the possibility

of thermally activated bow-out of the dislocation line between obstacles and require that activation occur at an obstacle. The activation energy is proportional to the area in force-displacement diagram (Figure 9), and may be written in dimensionless form

$$g_i^k = u(\beta_i) - u(\beta_i^k) \quad (\text{V.106})$$

where  $u(\beta)$  is the dimensionless area under both the force-displacement curve and a horizontal line of height  $\beta$ . The activation barrier at the ( $k$ -th) obstacle on (i) is then

$$\Delta G_i^k = 2\Gamma dg_i^k \quad (\text{V.107})$$

or

$$\frac{\Delta G_i^k}{2\Gamma} = \alpha g_i^k \quad (\text{V.108})$$

where  $\alpha$  is the "dimensionless reciprocal temperature"

$$\alpha = \frac{1}{T^*} = \frac{2\Gamma d}{kT} \quad (\text{V.109})$$

and  $d$  denotes the interaction range, usually of the order of one Burger's vector,  $k$  is the Boltzmann constant and  $T$  is the temperature.

For the statistics of thermal activation past a mechanically stable configuration of obstacles we require two general assumptions about the statistical nature of the activation process<sup>25</sup>:

i) Thermal activation is assumed in a sense that the probability of success in a given trial is independent of previous failures.

ii) Activation trials at a given obstacle are assumed stochastically independent of trials at the other obstacles in simultaneous contact with the dislocation and are taken to occur randomly in time with fixed frequency  $\omega$ . Using these two assumptions, the statistics of thermal activation past a line configuration may be developed as follows:

The probability for thermal activation past the (k-th) obstacle in configuration (i) in one attempt is

$$p_i^k = \exp(-\alpha g_i^k) \quad (V.110)$$

where  $( )$  and  $g_i^k$  have been defined in equations (V.109) and (V.106), respectively. The probability that the barrier remains uncut after  $j$  trials, given that it was intact initially is

$$q_i^k(j) = (1 - p_i^k)^j \quad (V.111)$$

Let the dislocation attempt the obstacle with mean frequency  $\omega$ , assumed constant, then, following assumption ii), that the activation trials occur randomly in time with expectation unity per unit of dimensionless time

$$t^* = \omega t \quad (V.112)$$

the probability of exactly  $j$  trials in time  $t^*$  is given by the Poisson formula

$$p(j, t^*) = \frac{(t^*)^j}{j!} e^{-t^*} \quad (V.113)$$

and the probability  $q_i^k(t^*)$  can be written <sup>25</sup> as

$$q_i^k(t^*) = \exp(-p_i^k t^*) \quad (V.114)$$

The probability that the  $i$ -th configuration remains uncut after time  $t^*$  is the probability that all obstacles on (i) remain intact at  $t^*$

$$q_i(t^*) = \prod_{k=1}^{N_i} q_i^k(t^*) = \exp(-\Lambda_i t^*) \quad (\text{V.115})$$

where

$$\Lambda_i = \sum_{k=1}^{N_i} p_i^k \quad (\text{V.116})$$

and  $N_i$  is the number of obstacles on (i).

The residence time of the dislocation in configuration (i) is the time required for thermal activation past at least one obstacle on (i). Hence the expected value of the residence time is

$$\langle t_i^* \rangle = \Lambda_i^{-1} \quad (\text{V.117})$$

The probability that thermal activation will occur first at an obstacle (k) on configuration (i) is

$$\eta(k, i) = \frac{p_i^k}{\sum_{k=1}^{N_i} p_i^k} = \frac{p_i^k}{\Lambda_i} \quad (\text{V.118})$$

In thermally activated glide the dislocation encounters a sequence of obstacle configurations as it moves through the array. These define the "glide path"  $\chi$  of the dislocation. If there are  $r$  stable configurations along a particular path ( $\chi$ ) through the array then the expected transit time of a dislocation along ( $\chi$ ) is

$$\langle t_\chi^* \rangle = \sum_{i=1}^r \Lambda_i^{-1} \quad (\text{V.119})$$

where we assume that the time required for dislocation glide between successive stable obstacle configurations is negligible compared to the time required for thermal activation past these configurations.

Given that the dislocation may take any one of many available glide paths through the array, the expected transit time is

$$\langle t^* \rangle = \sum_{\chi} \mu_{\chi} \langle t_{\chi}^* \rangle \quad (\text{V.120})$$

where  $\mu_{\chi}$  is the probability that the path  $\chi$  is followed in a given trial.

A variety of ways have been suggested to calculate the average velocity of a dislocation; such as from the total area swept through and the total time during motion; from the average area per activation event and the average expectation time and from the distance traveled by the end of a dislocation and total time. We define the expected value of the velocity of glide through a given array of obstacles in the following way: We consider a crystal made up of parallel glide planes, which contain a distribution of non-interacting gliding dislocations (i.e. the distance between planes is assumed to be sufficiently large). The expected value of the instantaneous strain rate of the crystal is

$$\dot{\gamma} = \frac{b}{V} \langle \partial A / \partial t \rangle \quad (\text{V.121})$$

where  $\langle \partial A / \partial t \rangle$  is the expected total area swept per unit time and  $V$  is the volume of the crystal. The strain rate in dimensionless form is

$$\dot{\gamma}^* = \left( \frac{\rho b}{l_s} \right) \langle v^* \rangle \quad (\text{V.122})$$

where  $\rho$  is the number of dislocations per dimensionless area and  $\langle v^* \rangle$  is the expected value of the dimensionless velocity, which can be written as

$$\langle v^* \rangle = N^{1/2} / \langle l^* \rangle \quad (\text{V.123})$$

or

$$\langle v^* \rangle = \frac{A^*}{W^* \langle l^* \rangle} \quad (\text{V.124})$$

where  $A^*$  is the dimensionless total area swept and  $W^*$  is the dimensionless width and  $N$  is the number of obstacles in the array.

For a crystal made up of stacking of ( $M$ ) parallel slip planes containing a uniform<sup>41</sup> distribution of dislocations the steady state strain rate may be written in dimensionless form

$$\dot{\gamma}^* = (\rho b / l_s) \bar{v}^* \quad (\text{V.125})$$

where  $\bar{v}^*$  is the average of the expected glide velocity for the individual planes in the crystal,

$$\bar{v}^* = \frac{1}{M} \sum_{i=1}^M \langle v_i^* \rangle \quad (\text{V.126})$$

with  $\langle v_i^* \rangle$  the expected value for the glide velocity of the dislocations in the ( $i$ -th) plane and  $M$  is the total number of glide planes.

## VI. COMPUTER SIMULATION

Given the geometric complexity of the dislocation structure and the microstructure in the usual realistic case the treatment of dislocation glide rapidly becomes analytically intractable, even when rather simple assumptions are made about the properties of the dislocations. In analytic treatment of dislocation motion, as described in the previous section, one is usually forced into idealizing assumptions concerning both the critical events which govern glide and the manner in which these events sum statistically to yield glide conditions or glide rates.

The availability of large computers adds a new dimension to the study of dislocation motion. Since these are capable of rapid numerical calculation, of storing and recalling complex geometrical information, and of modeling simultaneous interacting processes the efficient use of computers allows the study of dislocation models in much more elaborate detail. While computer models, like any theoretical models, require initial idealizing assumptions, the number of these assumptions may be greatly reduced and the richness of the results significantly enhanced.

The computer simulation research of this investigation has concentrated on the effects of the configuration of dislocations and the nature and distribution of microstructural barriers on the critical resolved shear stress and the velocity of thermally activated glide. Given the intent of this work the properties of the dislocations and the microstructural barriers have been modelled in the simplest plausible way so that the full power of the computer could be devoted to pro-

viding the geometrical structure needed to give good statistical detail.

A solution to the problem of plastic deformation in the simple model outlined in the previous section should predict at least three types of information:

(1) The athermal yield stress, or critical resolved shear stress for athermal glide ( $\tau_c^*$ ), which depends upon the distribution of dislocations, the nature of dislocation interactions, and the strength and distribution of barriers.

(2) The rate of deformation, which depends additionally on the applied stress, the temperature and the specific nature of the dislocation-obstacle interaction.

(3) The salient morphological features of the deformation process, including in particular the temporal "jerkiness" and spatial heterogeneity of flow. The solution should, moreover be phrased in analytic form, either as the analytic solution to a well-posed subproblem, or as an accurate analytic fit to probative computer-generated data.

Given these desirable features a suitable computer simulation code should have at least the following capabilities:

(1) The flexibility to simulate a variety of interesting cases;

(2) The ability to generate accurate data on the critical resolved shear stress and the flow rate for non-trivial models in reasonable computer time;

(3) The ability to monitor the deformation process in sufficient detail that critical mechanistic features may be identified and isolated for detailed study;

(4) The capability of computing and retrieving the specific data needed to

assess and criticize theoretical models.

A code which generally satisfies these criterion has been in use at Berkeley for sometime. In the following section the central features of that code, which have been reported primarily in references 41, 42, and 63, are described.

## A BASIC CODING TECHNIQUES

In the basic problem simulated in this research a dislocation is introduced into a glide plane containing a distribution of point barriers of specified properties. A stress is applied and the dislocation is allowed to move freely until it finds itself an obstacle configuration which cannot be passed mechanically under the applied load (Figure 10).

Subsequent behavior depends on the process being simulated. In simulating athermal glide the applied stress is increased until the dislocation configuration just becomes mechanically unstable. The dislocations are then displaced through the array until a new stable configuration is found.

As indicated in Figure 11 this process of raising the stress to the minimum point of instability and advancing the dislocation until a new stable configuration is found is continued until a new value of the stress is reached at which no further stable configurations occur. The lowest such value is the critical resolved shear stress,  $\tau_c^*$ . The salient feature of the athermal glide process is the strength determining configuration, the configuration of dislocations and obstacles which is most stable mechanically, and hence determines  $\tau_c^*$ .

In simulating thermally activated glide the applied stress is constant and

the activation barrier is computed at each pinning point in the configuration. The site for thermal activation is then chosen using proper statistical procedures<sup>25</sup> (or well- defined approximations to them.) The activated site is broken, and the dislocation is advanced until a new configuration is found. This process is iterated and the velocity of glide is computed from statistical formulae<sup>41</sup>. The salient feature of thermally activated glide is the sequence of stable configurations encountered during passage through the obstacle array, the geometric properties of these configurations determine the relevant activation barriers.

The precise code used to simulate the processes described above depends on the specific case under study e.g. whether the dislocation motion is assumed to be athermal or thermally activated. These various specific codes are, however, obtained by varying the peripheral features of a code which depend upon three central techniques: (1) A method for storing obstacle arrays so that local subsets can be easily accessed; (2) a data structure for dislocations, which carries all relevant information in a compact form and allows efficient modification as the dislocation is moved; (3) a consistent algorithm which advances dislocations efficiently and without loss of information.

### **I. Storing the Obstacle Array**

Clearly any algorithm for locally advancing a dislocation need consider only the obstacles in the immediate vicinity of the portion of the dislocation currently being advanced. It is hence efficient to store the obstacle array in subarrays such that only the relevant local subarrays need to be accessed and

considered when locally advancing the dislocation. If a subarray has an area,  $A$ , containing randomly distributed points of density one then the probability,  $\rho(n, A)$ , of finding  $n$  points in the subarray is

$$\rho(n, A) = \frac{A^n}{n!} \exp(-A) \quad (VI 1)$$

Inverting this function, a random number generator can be used to determine the number of points in each subarray. Thus by choosing the dimensions of the subarrays each subarray can be constructed individually.

The subarrays may be filled in either one of two ways. If the total size of the array is relatively small, so that computer storage is not an issue, one may simply fill the subarrays by using a random number generator to establish the  $x$  and  $y$  coordinates of the points contained. The  $x$  and  $y$  coordinates of all points may be stored in ordered one-dimensional arrays with additional ordered one-dimensional arrays, as needed, containing the strengths and other pertinent properties of the individual obstacles. Two additional arrays of dimensions two are used to store the start and the end location of each subarray in the  $x$  and  $y$  arrays. Thus a directory is created for finding the necessary subregions of the entire array. The directory also allows efficient storage of the  $x$  and  $y$  arrays. Finally, each obstacle is marked with a digit indicating whether it is behind, ahead of, or on a given dislocation.

When the simulation considers either glide through large arrays or simultaneous glide in several arrays computer storage becomes relevant. A straightforward and useful alternative method may then be used. Rather than storing

the entire array the seeds for the random number generator for each subarray are stored in the directory on construction of the subarrays previously described. Then no subarray need be retained in storage since each can be constructed consistently as needed. Arrays can be recorded and reproduced in separate experiments by simply recalling, (or consistently regenerating) the subarray structure and the associated seeds.

If the subsequent reproducibility of the particular obstacle array is not necessary to the simulation experiment an even more efficient technique may be used. The only a priori information known about a random array of obstacles is its density, which is, in this problem, identically one if the unit length is taken to be  $l$ . It is hence statistically permissible to construct random subregions as they are needed when the dislocation is advanced. Since the dislocation does not know what is in front of it, and does not remember what is behind it, the only obstacle information which ever need be actively in storage is the nature and location of the obstacles which are actually in contact with the dislocation and the nature and location of the obstacles immediately in front of the specific local section of the dislocation which is currently being advanced. In this the glide of an isolated dislocation through an array of very large size may be efficiently treated with minimal demand on computer memory.

These are the basic algorithms used in the simulation code to efficiently create, store and retrieve the obstacle arrays. The modification of these techniques to treat non-random distribution of obstacles is straight-forward.

## 2. Representing the Dislocation

To optimize the information obtained from the simulation of glide it is important that the dislocation be stored in the computer in a simple array which contains all relevant information and can be easily accessed and updated. These criteria are efficiently met by a data structure in which a dislocation is represented by a two-way chained list. The central element of this structure is a simple ordered list of the x and y coordinates of the obstacles in current contact with the dislocation. Each obstacle in this list is then connected to two identifiers which give the location in storage of the obstacles to its immediate left and right, and to a mark which indicated whether the mechanical stability of the dislocation segment to the right of the obstacle has been verified. The configurations of several dislocations may be simultaneously stored by adding a list of pointers to one obstacle on each dislocation; given periodic boundary conditions the sublist representing a single dislocation will be closed under the operation of left and right connection.

All relevant information concerning the dislocation, such as the shapes of inter-obstacle segments, the forces on the obstacles, and the mechanical stability of the configuration, may be easily computed from the information contained in this double chained list. When the dislocation is advanced the bypassing of an obstacle is accounted for by simply deleting it from the list and updating the relevant connections; contact with a new obstacle is achieved by simply adding it to the list. Interesting configurations, such as the strength determining configuration may be stored for later study by simply copying the

list in storage.

### 3. Advancing the Dislocation

The dislocation is advanced in the code by the analytic equivalent of the following procedure. A dislocation configuration becomes unstable by bypassing an obstacle along it, either because of mechanical instability of the segment to the left or right of the obstacle due to the increasing stress or because the obstacle has been passed by thermal activation according to some criterion. This obstacle is appropriately marked and removed from the list representing the dislocation, the obstacles to its left and right are connected in the list and the associated segment is marked to indicate that its stability has not been verified.

The new dislocation segment will bow out between its terminal obstacles toward equilibrium. This bow-out process will be terminated by the first of three events:

(1) the dislocation encounters a new obstacle of the array;

(2) the dislocation violates the angle condition  $\psi > \psi_c$  or the strength condition  $\beta < \beta_c$  at one of its two end points;

(3) the dislocation segment bows into the equilibrium radius  $R^* (= 1/2\tau)$ .

To determine the first of these events the following geometric relation is utilized (Figure 12): if a circular arc is drawn through two points A and B, and if a third point, C, is located on this arc and connected to A and B by lines  $\overline{AC}$  and  $\overline{CB}$ , then the angle,  $\alpha$ , measured clockwise between the extension of  $\overline{AC}$  and

$\overline{CB}$  is given

$$\alpha_i = \sin^{-1}(\overline{AB}/2R) \quad (\text{VI } 2)$$

where  $\overline{AB}$  is the distance from A to B and R is the radius of the arc. Using the terminal conditions (2) and (3), a maximum value,  $\alpha_m$ , may be found at which the bow-out process necessarily terminates. The area of the array associated with bow-out to  $\alpha_m$  may then be identified and the values of  $\alpha_i$  computed for each obstacle,  $C_k$ , within this area.

If there are obstacles having  $\alpha_k \leq \alpha_m$  then the particular obstacle having the minimum value of  $\alpha$  would be the first contacted by the dislocation in a continuous bow-out process. The obstacle is added to the dislocation and the list is updated to correct for its connections to left and right. The corresponding sections are marked and their stability or possible further subdivision is tested in turn.

If there are no obstacles having  $\alpha_k \leq \alpha_m$  then the appropriate terminal condition (2) or (3) is invoked. If condition (2) pertains then the unstable end point is by-passed by properly marking it, removing it from the list, and updating the list. The update defines a new segment whose stability must be tested. If condition (3) pertains then a stable segment has been found. When the list representing the dislocation contains only stable segments a stable configuration has been found.

When the dimensionless applied stress is high ( $\tau^* \geq 0.5$ ) an additional check must be made for possible instability due to self-intersections of the dislocation and a procedure must be provided to decompose the dislocation list

to account for the formation of stable loops from self-intersections during glide. The procedures for handling these cases are straight-forward using the data structure and search algorithm described. At lower values of  $\tau^*$  such intersections are extremely uncommon, and may usually be ignored.

A stable configuration may be broken by either increasing the stress or selecting an obstacle for thermal activation. The stress at which the configuration first becomes unstable may be precisely calculated, and corrected for possible contact with additional obstacles during bow-out as the stress is raised. The athermal critical resolved shear stress is that value of  $\tau^*$  which is just sufficient to insure that no stable configurations are found. It may be found by continuously increasing  $\tau^*$  until no further stable configurations are encountered (Figure 11).

For thermally activated glide, the following procedure is used to calculate the velocity of glide. Given a stable configuration, the code computes the angles  $\psi_i^k$  along it, and uses the assigned value of the dimensionless reciprocal temperature,  $\alpha$ , to compute the mean residence time according to equation (V.117). It then calls a random number and chooses an activation site according to the probability assignment given in equation (V.118). The chosen point is passed, and the code then initiates a new search to establish the next stable configuration. In this way a statistically chosen glide path is generated and a transit time is computed according to equation (V.119). By allowing several sequential passages the ergodic average of the transit time is estimated (equation (V.120)) and the glide velocity  $\langle v^* \rangle$  found.

The above described data structure and search algorithm combine to yield a code whose efficiency is sufficient for the purposes of this research. In current use on the CDC 6600/7600 system at the Lawrence Berkeley Laboratory the code requires  $\sim 25$  computer units ( $\sim 8$  seconds) of running time to determine the athermal resolved shear stress for glide through an array of  $10^4$  points together with a geometric analysis and TV-graphic plot of the strength determining configuration. The simulation of thermally-activated glide is only slightly less rapid. The simulation of glide through very large arrays is relatively time-consuming, but not prohibitively so. Analysis of glide through a square array of  $10^6$  points requires  $\sim 1500$  computing units ( $\sim 7 \frac{1}{2}$  minutes).

## **B. APPLICATIONS AND RESULTS**

The coding procedures described above have been used to conduct simulation studies on the problem of dislocation motion through randomly distributed point obstacles. The athermal critical resolved shear stress for glide through a random array of like obstacles was previously investigated by Kocks<sup>30</sup> (for the particular case of impenetrable obstacles) and by Hoyer and Makin.<sup>23</sup> These studies were extended<sup>44</sup> to include the statistics of the athermal glide stress and the detailed features of the particular obstacle configurations in the limit of large array size. To test the validity of the equations obtained for CRSS and the geometric properties of the strength-determining configurations it was necessary to simulate glide through very large arrays. The results obtained from this study are reported below.

### **1. DISLOCATION GLIDE THROUGH LARGE ARRAYS**

To study the effects of array size and shape we employed computer simulation of dislocation glide through arrays containing  $10^3$  to  $10^6$  obstacles. In each case the properties of the strongest configuration (i.e. CRSS, average segment length, distribution of forces and segment lengths) were printed out. The size effect was studied by taking square arrays and increasing the number of obstacles (e.g. for  $10^6$  obstacles we took an array of size of  $1000 \times 1000$ ). For the shape effect, the number of obstacles was kept constant (e.g. 250,000) but the width of the array was changed.

Two types of boundaries were used in this study. Periodic boundaries, where the array is extended periodically in both directions were used in most of

the computer simulation runs. Mirror boundaries which require that the dislocation meets the boundaries at right angles has also been used in order to see the effects of boundary conditions.

Figure 13 shows the data obtained from simulation of arrays containing up to  $10^6$  obstacles. The CRSS for athermal glide is plotted as a function of the width of the array. The obstacle strength ( $\beta_c$ ) was chosen to be 0.01 and periodic boundaries were used. As is clear from the figure, the CRSS decreases steadily as the array size is increased and approaches a limiting value. The comparison between computer simulation and predictions (equations (III.17), (V.23) and (V.46)) are shown in Figure 14, where the strength of the array  $\beta_1$  at a fixed value of the applied stress ( $\tau^* = 0.001$ ) is plotted as a function of the width of the array. As can be seen from the figure, the parameter  $\beta_1$  increases with array size and appears to asymptote at a value close to that predicted by Hanson and Morris<sup>44</sup>. For comparison the value of  $\beta_1$  predicted by Friedel<sup>13</sup>, (equation III.17), is also included, which underestimates the data for large arrays. The solution by Labusch<sup>58</sup>, equation (V.46), underestimates the data, but the corrected form, equation (V.47), gives very close agreement with the value obtained from arrays containing  $10^6$  obstacles. The data bars in Figures 13 and 14 correspond to computer simulation of two different arrays. Notice that these values are different even for large arrays. The scatter in data, i.e. changes in the properties of the strongest configuration from array to array has important consequences with respect to deformation behavior of idealized crystals.<sup>42</sup>

The distribution of forces on the strongest configuration of an array containing  $10^6$  obstacles is shown in Figure 15, where the force exerted by the dislocation on each obstacle in the strongest configuration is calculated according to equation (III.9). The theoretical distributions are those obtained by Hanson and Morris<sup>44</sup>, equation (V.26), and by Labusch,<sup>58</sup> equation (V.48). The data to construct the histogram was obtained from dislocation glide through  $10^6$  obstacles at a stress of  $\tau^*=0.001$ . The strongest configuration contained 141 obstacles.

The force distribution given by Hanson and Morris gives a rather good fit to the empirical histogram obtained from computer simulation. The prediction by Labusch requires a correction factor in order to give a reasonable fit to the empirical distribution.

The average segment lengths, obtained from two arrays containing obstacles from  $10^3$  to  $10^6$  are plotted in Figure 16 as a function of the width of the arrays. The  $\langle l^* \rangle$  values seem to be a slowly increasing function of array size, and to approach the value predicted by Hanson and Morris<sup>44</sup>, equation (V.34), for very large arrays. The "Friedel relation", equation (III.19), overestimates the simulation data by more than 30%. The value obtained by Labusch, equation (V.53), underestimates the computer simulation results for large arrays.

The distribution of segment lengths are compared in Figure 17, where the histogram obtained from an array containing  $10^6$  points is plotted at a constant applied stress of  $\tau^*=0.001$ . The theoretical distribution by Hanson and Morris<sup>44</sup>, equation (V.30) does a poor job of reproducing the empirical curve,

suggesting that the discrepancy is due to the approximations used in the theoretical model and not due to array size. However, as noted earlier, the average segment length matches that obtained from theory very closely. The prediction by Labusch<sup>58</sup>, equation (V.51), gives the shape of the histogram reasonably well.

The distribution of the angle  $\phi$  predicted by both theories, equations (V.29) and (V.50), are compared with the simulation data in Figure 18. The solution by Hanson and Morris<sup>44</sup> requires that there is a cut-off angle  $\phi_0$ , whereas the prediction by Labusch<sup>58</sup> gives a rather good fit to the empirical distribution.

### a) Correction to the Theory

In the following a simple analytic technique for estimating the influence of the array size on the CRSS will be given. We assume, in addition to those introduced in reference 44, that an obstacle array of arbitrarily large size contains a high density of strong configurations and the strong configurations encountered in glide through a finite array are subsets of these. Using these assumptions one could write the average number of configurations having strengths  $\beta \geq \beta_1$ , to be

$$\langle m \rangle = \left( \frac{nN}{2} \right) (S)^n \quad (\text{VI.3})$$

where  $n$  is the number of obstacles on the dislocation,  $N$  is the total number of points in the array and  $S$  is the area of force distribution, (Figure 19).

By setting

$$\langle m \rangle = 1 \quad (\text{VI.4})$$

one can write

$$S(\beta) = \left( \frac{nN}{2} \right)^{-\frac{1}{n}} \quad (\text{VI.5})$$

and inverting

$$\beta = f(S) \quad (\text{VI.6})$$

Using equation (V.28) for  $S$ , the value of  $\beta$  or  $\tau^*$  can be calculated numerically.

Figure 20 shows the value of the obstacle strength,  $\beta_1$ , required to prevent athermal glide under given applied stress as a function of array width, for two

stresses,  $\tau^* = 0.005$  and  $\tau^* = 0.001$ , where mirror boundaries were used. The agreement between the computer simulation and the prediction (equation (VI.6)) is very good. In Figure 21, the CRSS for athermal glide is plotted as a function of the dimensionless obstacle strength,  $\beta_1$ , for square arrays containing  $10^6$  points. Here, periodic boundaries were used. Again for these sizes of arrays the agreement between calculation and computer simulation is good. However, further refinement of the analysis is needed to account for effects which intrude at higher obstacle strengths and for the influence of boundary conditions in arrays of small size.

To study the effects of array shape on the properties of the strongest configuration, rectangular arrays are considered, where the number of points in the array is kept constant and the array width or height is varied. The strength  $\beta_1$  as a function of the width of the array containing 250,000 points is shown in Figure 22. The computer simulation data was taken for an applied stress  $\tau^* = 0.005$  and periodic boundaries were used. The prediction according to equation (VI.6) is drawn as a continuous line. The agreement between theory and computer simulation is good.

### b) Thermally Activated Glide

The dependence of  $\beta_1$  on array size and shape has profound effects on dislocation velocity in thermally activated glide. For a dislocation-obstacle interaction of simple step form, the velocity of the dislocation at low temperatures can be written<sup>41, 42</sup> in Arrhenius form

$$\langle v^* \rangle = \frac{N}{W^*} \exp[-\alpha(\beta_c - \beta_1)] \quad (\text{VI.7})$$

where  $N$  is the number of obstacles in the array and  $W^*$  is the width of the array in terms of  $l_s$ , and  $\alpha$  is the thermal parameter (equation (V.109)). As can be seen from equation (VI.7), as  $\beta_1$  increases with  $W^*$  the dislocation velocity will increase exponentially, the more so as  $\alpha$  increases, i.e. as temperature decreases. The scatter in  $\beta_1$  from array to array has also important consequences<sup>42,43</sup>, where at low temperatures the dislocation will glide on those planes on which the glide velocity is highest and thus the deformation of the crystal appears inhomogeneous. The deformation becomes homogeneous as temperature is raised or stress is decreased.

## 2. GLIDE THROUGH FIELDS OF UNLIKE OBSTACLES

Foreman and Makin<sup>33</sup> were the first to report on the computer simulation of dislocation glide through mixture of obstacles. They carried out their simulation for relatively high strength obstacles and used mirror boundary condition. Their results seem to confirm equation (V.92), quadratic mean of stresses, for all strong obstacles except in the region where  $\beta_s \gg \beta_w$  and  $x_s \ll x_w$ , where equation (V.93), simple addition of stresses, is assumed to be valid.

Hanson and Morris<sup>45</sup> extended the analytic procedure to estimate the critical resolved shear stress for glide through an array of like barriers, to treat the case of simultaneous random distribution of obstacles of different properties. The predictions of the equations were compared to the results of simulation experiments on glide through arrays containing both strong and weak obstacles. Relevant properties of the strength-determining configurations were determined, including the distribution of angles and segment lengths and the relative

fractions of strong and weak obstacles in actual contact with the dislocation line.

#### a) Two types of obstacles

To identify the regions of applicability of the solutions to the CRSS for two kinds of obstacles we carried out extensive computer simulation of mixtures of two kinds relatively weak obstacles using periodic boundary conditions.

In Figure 23, we plot the CRSS for arrays containing strong and weak obstacles as a function of the fraction of weak obstacles ( $x_w$ ). The CRSS decreases as more and more weak obstacles occupy obstacle positions. The relative strengths of the obstacles correspond to the critical angles of  $90^\circ$  and  $130^\circ$ . To obtain the data we used 10,000 obstacle arrays. For comparison we plot the data obtained by Foreman and Makin<sup>33</sup> and the approximate equation (V.80). Both the data obtained in this study and by Foreman and Makin is in good agreement with the prediction.

In Figure 24 we show the dependence of the CRSS on the fraction of strong obstacles ( $x_s$ ), which increases as the relative number of strong obstacles increases. The obstacles have strengths 0.1, 0.05 and 0.01. The data is obtained from computer simulation of 10 arrays containing 10,000 obstacles and is shown as data bars. We have also plotted various predictions discussed earlier. The formula (V.92) fits the data approximately over the whole region of obstacle fractions, except in the case where  $\beta_s \gg \beta_w$  and  $x_s \ll x_w$ , where the simple addition of stresses can be used. The approximate formula (V.80) fits the computer simulation data over the whole region of obstacle strengths and fractions. The exact theoretical prediction (equations(V.66) and (V.67))

underestimates the data consistently, a result which is believed to be due to relatively small size of the arrays used to obtain the data. The CRSS for arrays containing two types of obstacles is also array size dependent and decreases as the width of the array increases. This is illustrated in Figure 25, where we have plotted CRSS as a function of the width of the arrays containing two types of obstacles of strengths  $\beta_s = 0.05$  and  $\beta_w = 0.01$  and relative fractions  $x_s = 0.1$  and  $x_w = 0.9$ . The CRSS decreases steadily and seems to approach a limiting value for large arrays.

The problem of finding the applicability and the ranges of validity of equations (V.92) and (V.93) is considered in Figures 26 and 27. It is clear from Figure 24 that the simple addition of stresses consistently overestimates the simulation data and the difference diminishes as the ratio of the obstacle strengths is increased. This suggests that either the equation (V.93) is valid in a very limited range of obstacle strengths and fractions or it is fortuitous and holds when the effect of one of the obstacles is negligible. The differentiation between formulas (V.92) and (V.93) is difficult because of the scatter in data obtained from these finite size arrays. Since, the size of the array was not considered in obtaining equations (V.92) and (V.93) and since the plot of these predictions require the knowledge of the end points  $\tau_s^*$  and  $\tau_w^*$ , at  $x_s = 1$  and  $x_s = 0$ , we simulated an array which is rectangular in shape and contains 2000 points. The width of the array was chosen to be 200 so that the strongest configuration will contain a larger number of obstacles. The obstacle strengths were chosen to be 0.1 and 0.01, giving a ratio of 10, which could be considered

to be in the range of applicability of equation (V.93). Figure 26 shows the CRSS as a function of fraction of strong obstacles in the array. We considered arrays containing up to 10% strong obstacles. Even in this range, where the array contains many weak and few strong obstacles, equation (V.93) overestimates the computer simulation data, whereas equation (V.92) gives a very good fit to the simulation results. The data obtained from simulation of arrays containing an even smaller number of obstacles ( $x_s < 1\%$ ) did not fall through the prediction of equation (V.93). As shown in Figure 27, even for this case, equation (V.92) predicts the results rather closely.

Aside from the comparisons made with computer simulation data, equations (V.92) and (V.93) also differ in their behavior of slopes ( $d\tau^*/dx_s$ ) as  $x_s$  approaches zero. This slope is finite for equations (V.80) and (V.92), whereas for the simple addition of the stresses it is infinite. However, it is difficult to get  $(d\tau^*/dx_s)$  from the computer simulation data as  $x_s \rightarrow 0$ . Also as was shown previously, the equation (V.93) breaks down for  $\beta_s = \beta_w$  and  $x_s = x_w = 0.5$ .

The fraction of strong obstacles on the strongest configuration ( $c_s$ ) is shown as a function of the fraction of strong obstacles in the array ( $x_s$ ) in Figure 28. The obstacle strengths used to obtain the data were 0.1, 0.05 and 0.01. The parameter  $c_s$  increases with  $x_s$  with sharper slope as the fraction ( $\beta_s/\beta_w$ ) increases. We have also plotted in the figure the analytical prediction, according to equation (V.81). As is apparent from the figure the calculation reproduces the computer simulation results very well.

The average segment length as a function of the fraction of strong obsta-

cles is plotted in Figure 29 and compared with the equation (V.87). The calculation (equation (V.87)) gives a good fit to the data obtained from the computer simulation of arrays containing 10,000 obstacles. An interesting feature in the figure is that the average segment length as a function of  $x_s$  undergoes a maximum in the range where there are a lot of weak and few strong obstacles. This maximum is predicted correctly by the equation (V.87) and is more pronounced when the difference in the obstacle strengths is large. This can be explained with the help of Figure 28, where the dislocation "picks up" more strong obstacles at small fractions which is more pronounced as the ratio  $(\beta_s/\beta_w)$  increases. For example, in arrays containing 5% strong obstacles, the strongest configuration contains 20% strong obstacles for  $(\beta_s/\beta_w)=2$ . The fraction of strong obstacles increases as  $(\beta_s/\beta_w)$  increases. For  $x_s=0.6$ , the fraction of strong obstacles is, from Figure 28, about 55% for  $\beta_s/\beta_w=5$  and 75% for  $\beta_s/\beta_w=10$ .

#### b) Square spectrum of obstacle strengths

The obstacle strength can be defined either by the critical angle  $\psi_c$  or the critical strength  $\beta_c$ . We first consider the square distribution of obstacle angles  $\psi$ , as shown in Figure 7. The critical resolved shear stress  $\tau^*$  as predicted by the equation (V.100) is shown as functions of the average angle  $\psi_m$  and the width of the distribution  $\psi_w$  in Figure 30. The data obtained by Foreman and Makin<sup>33</sup> in simulating arrays containing 10,000 points is plotted as points. The data obtained in the present work is plotted as data bars and is taken from computer simulation of five arrays containing 1600 obstacles. As can be seen in the

figure the prediction (equation (V.100)) fits the data very well within the range of scatter. The calculation in the range of  $\psi_m \leq 3\pi/8$  was done for completeness, since the work by Bacon et al.<sup>64</sup> showed, that due to the interaction between neighbouring segments the more realistic case for point obstacle strengths to be 0.7 and lower. In general, as shown in Figure 30,  $\tau^*$  is a very weak function of the width of the distribution and decreases slowly if  $\psi_m < \frac{\pi}{2}$  and increases with  $\psi_m$  if  $\psi_m > \frac{\pi}{2}$ . In Figure 31 we show the results for CRSS obtained between the angles  $\frac{\pi}{2}$  and  $\pi$ . The constant k in equation (V.100) which is array size dependent was obtained for  $\psi_m = 5\pi/8$  to be 0.92 from 5 arrays containing 1600 obstacles.

The second case to be considered for the distribution of obstacle strengths is the square spectrum of strengths( $\beta$ ) according to Figure 8. We plot the CRSS as a function of the width of the distribution in Figure 32. We used equations (V.90) and (V.91) to convert  $\beta_i$  into  $\psi_i$ . The data bars indicate the computer simulation results of five arrays containing 1600 points. The prediction according to equation (V.105) is also plotted in the figure and shows good agreement with the computer simulation data. Figure 32 is very similar to Figure 30, except when the average angle  $\psi_m$  is less than  $\frac{\pi}{2}$ . In this range, the decrease in CRSS is stronger in Figure 32 than in Figure 30. The conversion of the two kinds of square distribution is also possible using

$$\left| \rho(\psi) d\psi \right| = \left| \rho(\beta) d\beta \right| \quad (VI.8)$$

For

$$\rho(\beta) = \frac{1}{\beta_{\max} - \beta_{\min}}$$

and

$$d\beta = \frac{1}{2} \sin \frac{\psi}{2} d\psi \quad (\text{V1 9})$$

we get

$$\rho(\psi) = \frac{\sin(\frac{\psi}{2})}{2(\beta_{\max} - \beta_{\min})} \quad (\text{V1 10})$$

or for 
$$\rho(\psi) = \frac{1}{\psi_{\max} - \psi_{\min}}$$

$$\rho(\beta) = \frac{2}{\psi_{\max} - \psi_{\min}} \cdot \frac{1}{\sqrt{1 - \beta^2}} \quad (\text{V1 11})$$

Thus, the uniform distribution of angles emphasizes the stronger obstacles. Both distributions give similar results if the obstacle strengths are small (or for large angles).

The CRSS for the uniform distribution of relatively weak obstacles corresponding to angles between  $\frac{\pi}{2}$  and  $\pi$ , is given as a function of  $\psi_w$  in Figure 33, where the results are very similar to the one shown in Figure 31.

The average segment lengths as a function of  $\psi_w$  for the uniform distribution of relatively weak obstacles is shown in Figure 34. The average segment length depends very weakly on  $\psi_w$ . The prediction, which is obtained from equation (V.87), is also plotted in the figure and shows good agreement with

the computer simulation data.

The distribution of forces on the strongest configuration obtained from computer simulation of arrays containing uniform distribution of obstacle strengths is compared with the theoretical prediction in Figure 35 and show excellent agreement.

### c) Thermally activated glide

Thermally activated glide through arrays containing one type of obstacle has been studied extensively in references 25,41 and 42. In these studies, the statistics of thermally activated glide were developed and useful approximations identified. These approximations were studied through simulation and their range of accuracy identified<sup>41,42</sup>.

In this section, we report results obtained for thermally activated glide through arrays containing two types of obstacles, distributed randomly. We assume that the force-displacement relation is of simple step form. Also, we do not differentiate between obstacles of different types concerning the effective range of interaction ( $d$ ) so that the parameter  $\alpha$  remains the same for both types of obstacles. If the effective ranges of interaction were different, the parameters must be modified accordingly.

Figure 36 gives the stress ( $\tau$ ) at a given velocity of glide as a function of temperature ( $T$ ), for an array containing 2000 obstacles, half of which are strong ( $\beta_s = 0.05$ ) and the other half weak ( $\beta_w = 0.01$ ), at a velocity of  $\ln\langle v \rangle = -10$ . The stresses at  $\ln\langle v \rangle = -10$  as a function of temperature is also plotted if the arrays contained only strong and only weak obstacles.

Using the data given in Figure 36, we see that the formula

$$\tau^*(T^*) = \tau_s^*(T^*)x_s + \tau_w^*(T^*)x_w \quad (VI.12)$$

closely approximates the computer simulation results over the whole range of temperature, whereas the formula

$$\tau^*(T^*) = \tau_s^*(T^*)\sqrt{x_s} + \tau_w^*(T^*)\sqrt{x_w} \quad (VI.13)$$

overestimates the data.

For arrays containing smaller fractions of strong obstacles (10%), the above results are not changed and equation (VI.12) gives a good fit to the computer simulation data (Figure 37).

One of the most striking features in thermally activated glide through arrays containing more than one type of obstacle is that the characteristics of the configurations change with temperature. This is illustrated in Figure 38, where we have plotted the fraction of strong obstacles on the strongest line ( $c_s$ ) as a function of the inverse of the temperature ( $1/T^*$ ) at a given stress ( $\tau^* = 0.005$ ). As can be seen from the figure, the fraction of strong obstacles increases as temperature decreases, suggesting that at low temperatures only strong obstacles determine the strength and at high temperatures the effect of weak obstacles becomes more pronounced. The parameter  $c_s$  approaches the athermal value (Figure 28) as the temperature decreases. The configurations obtained at high ( $T^* = 0.1$ ) and low temperatures ( $T^* = 0.001$ ) are also shown in the figure, where circles represent strong obstacles and dots represent weak obstacles. It is clear from the figure that the number of strong obstacles on the line decreases as temperature increases.

## VII. COMPARISON WITH EXPERIMENTS AND DISCUSSION

The computer simulation experiments discussed above give us information on the statistics of overcoming local obstacles by dislocation which is needed for a reliable analysis of the experimental data and for the further development of the theory of dislocation mobility and crystal plasticity. However, the results obtained are sensitive to the approximations used and it is necessary to check the validity of the assumptions and modifications of the model.

The general problem of plastic deformation arising from cutting of localized obstacles is complicated by the intrusion of several factors. An extensive literature has been developed to describe deformation characteristics due to the motion of dislocations past localized stress fields arising from the presence of substitutional and interstitial solute atoms<sup>15, 16, 22, 28, 29</sup>, tetragonal point defects<sup>28, 29</sup>, precipitates and dispersed phases<sup>20, 26, 48, 49, 65-68</sup> and centers of radiation damage<sup>69-73</sup>. While the details will not be reviewed here, it is appropriate to reconsider the validity of some of the simplifications that have been made to facilitate analyses. The stress fields due to the lattice strain centers decrease very rapidly in amplitude and spread over larger areas of the slip plane as their distance from the slip plane increases. It has been customary to neglect the effects of all strain centers lying a greater distance away than one atomic plane on either side of the slip plane. In most approaches no consideration is given to the fact that the strain centers are usually more or less randomly distributed.

In this study, we assumed the obstacles to be point-like and randomly dis-

tributed. In most models, the nature of the obstacles has generally been unspecified, however a proper description of point obstacle approximation is necessary. According to Morris and Syn<sup>74</sup>, if the effective range of interaction ( $d$ ) is small compared to the mean separation ( $\bar{L}$ ) of the obstacles, which are taken to be identical circularly symmetric barriers to the dislocation glide, then the obstacles can be treated as point-like. Thus, in this model we shall be concerned with barriers having short range interactions. The assumption of randomness of point obstacles is a good one if the obstacles are non-interacting impurities, small dispersion particles or small voids. Interacting point obstacles or flexible forest dislocations will not be random. The nature of the motion of a dislocation through non-random obstacles can of course be quite different and is more pronounced for high-strength obstacles<sup>74</sup>.

We considered dislocations to be flexible, extensible strings of constant line tension, thus, neglecting effects of orientation, radius of curvature and the influence of elastic anisotropy on the energy of the dislocation.

Bacon et al.<sup>65</sup> considered the change in line tension with dislocation type and obstacle spacing when the obstacles are strong. The magnitude of line tension can vary by a factor of 4 depending upon whether the dislocation is edge or screw in character, however, an average line tension could be used for dislocations of mixed character<sup>49,75</sup>. The elastic anisotropy has been considered by Scattergood and Bacon<sup>76-78</sup>.

Given the accuracy and short-comings of the model an attempt will be made to make qualitative and quantitative comparison of the results with exper-

experimental data. The general approach to be followed in order to make the comparison is the following: since the equations given in the previous section are all in non-dimensional form, they have to be dimensionalized. The CRSS in dimensional form is given by equation (III.5) and can be written as:

$$\tau = \tau^* \frac{2\Gamma}{l_s b} \quad (\text{VII.1})$$

where  $\tau^*$  is the dimensionless CRSS,  $\Gamma$  is the line tension and  $l_s$  is the Burgers vector. The average spacing  $l_s$  can be calculated from the density of obstacles. If the character of the moving dislocation is known, then the line tension ( $\Gamma$ ) and Burgers vector  $b$  can be determined. Since  $\tau^*$  depends on the obstacle strength ( $\beta_i$ ), this also has to be calculated or estimated and would generally depend on the shape<sup>79</sup>, size and position of the obstacles relative to the glide plane. The critical force in dimensional form is given by:

$$F_c = 2\Gamma\beta_i \quad (\text{VII.2})$$

If the distributions of the obstacle strengths are known then the dimensionless CRSS ( $\tau^*$ ) can be calculated using equation (V.96) and in dimensional form via equation (VII.1).

The most simple but powerful result obtained from the model considered here is that the CRSS  $\tau$  is proportional to the square root of the obstacle concentration,  $c$ . Since  $l_s \propto \frac{1}{\sqrt{c}}$  we obtain from equation (VII.1)

$$\tau \propto \sqrt{c} \quad (\text{VII.3})$$

This is an experimental fact, observed in most of the experimental studies on

dilute solution and precipitation hardened materials

The first direct comparison of experiment and computer simulation involves qualitative aspects of the dislocation motion. The experimental data is taken from Barnes<sup>49</sup>, who studied the movement of dislocations in irradiated copper crystals. Figure 39 shows the sequence of four successive Transmission Electron Micrographs of copper which had been bombarded with  $3 \times 10^{17}$  38MeV alpha particles per  $\text{cm}^2$  and, as a consequence contains small dislocation loops and even smaller black dots only just resolvable. The dislocation which was induced to slip by intermittently removing the condenser aperture from the electron microscope, moves upward and forms a series of arcs in this direction and is held at individual points along its length. The movement can be realized more readily from Figure 39, where the four dislocations have been superimposed by tracing each in turn, and it can be seen that some sections do not advance between photographs, while neighbouring sections do. It is apparent that the dislocation was held by a number of very small obstacles until, under the stress the dislocation, released from one, rapidly advanced until it met the next obstacle in its path. It is believed that these small obstacles in copper irradiated with alpha particles are vacancy clusters which are not planar and that each of them is acting as an obstacle, and it is possible that even smaller crystal disturbances, which are not detected in the electron microscope, are also effective<sup>50</sup>.

For comparison we have also printed in Figure 39, the motion of the dislocation through randomly distributed point obstacles taken from the computer

simulation 'snapshots'. The dislocation is moving upward and the separation of the successive configurations is shown. Quite surprisingly, the motion of the dislocation in computer simulation and experiment is very similar. Some points can be made from the comparison.

ii) The obstacles to dislocation motion in irradiated Cu are not distributed in a regular manner, rather they are distributed in a more or less random fashion.

iii) The obstacles are not of equal size and each interact with the dislocation differently, suggesting that their strengths are not the same.

iv) Not only the dislocation moves in the same fashion, but also the lengths of dislocation segments between pinning obstacles are very similar.

v) The dislocation bows between the obstacles in approximately circular fashion.

In direct observation of the interactions between dislocations and precipitates in an Aluminium - Silicon alloy Nemoto and Koda<sup>60</sup> estimated the CRSS from the measurements of the radius of curvature of moving dislocations expanded between the precipitates. Their micrographs showed also close resemblance to the dislocation motion through computer simulation.

In order to study the dynamical behaviour of dislocations a direct method has been developed in recent years. This method is based on the *in-situ* deformation experiment in a High Voltage Electron Microscope (HVEM) with a tensile device attached to it. In this technique, the specimen is deformed plastically while under observation in a HVEM, and the behaviour of individual

dislocations is recorded continuously. Figure 40 is taken from such a study.<sup>53, 54</sup> In Figure 40 we compare the distribution of segment lengths obtained from computer simulation with the experimentally determined one. Saimoto et al.<sup>53, 54</sup> studied using HVEM the deformation of Cu single crystals. In their study, in order to characterize the dislocation-dislocation interactions, geometrically, following properties of the specimen were required:

- A homogeneous microstructure throughout the crystal; the scale of which is small enough such that it can be completely examined in the electron microscope.
- The dislocation arrays are more or less random without clustered regions such that every dislocation and node can be resolved.
- The yield stress can be reproducibly determined from specimen to specimen.

The specimen which satisfied the above structural conditions closely was identified and *in-situ* HVEM deformation studies were conducted<sup>53</sup>. HVEM has the advantage of being able to penetrate relatively thick foils which permit determinations of the three dimensional array of dislocations. Saimoto et al.<sup>53</sup> measured the distribution of true segment lengths and the interobstacle spacings. From these measurements and using the following formula for CRSS

$$\tau = 0.887\beta_c^{3/2} \frac{Gb \ln(l_s/r_0)}{l_s} \quad (\text{VII.4})$$

they were able to estimate the obstacle strength  $\beta_c$  to be between 0.3 and 0.7, taking various values for the lower cut-off radius  $r_0$ . They used two reflection

order to determine the effect of the impurity concentration on the dislocation velocity. Figure 4 shows the results of the computer simulation for a dislocation in a pure metal. The dislocation velocity is plotted against the applied shear stress. The dislocation velocity is found to increase with the applied shear stress. The dislocation velocity is found to increase with the applied shear stress. The dislocation velocity is found to increase with the applied shear stress. The dislocation velocity is found to increase with the applied shear stress. The dislocation velocity is found to increase with the applied shear stress.

It is interesting to note that the dislocation velocity is found to increase with the applied shear stress. This is in agreement with the experimental results of Nabarro and Flynn (1957) and Flynn and Nabarro (1958). Flynn and Nabarro (1958) found that the nature of the dislocation core is different from that of a perfect dislocation. Using the same technique, Van der Ven and Nabarro (1961) measured the dislocation velocity in Mo-0.5% copper crystals containing impurities as a function of applied stress and temperature.

The stress exponent,  $m^*$ , which is defined from the stress dependence of the dislocation velocity

$$\langle v^* \rangle = (\tau^*)^{m^*} \quad (\text{VII.5})$$

as

$$m^* = \frac{d \ln v^*}{d \ln \tau^*} \quad (\text{VII.6})$$

was given as a function of temperature. Several other investigators have tried to predict  $m^*$  as a function of stress and temperature<sup>84-86</sup>. Computer simulation studies<sup>42</sup> suggest that the stress exponent is a function of stress and

temperature and increases as stress increases or temperature decreases. In the following a very simple method is given to predict  $m^*$  at low temperatures and high stresses. Since the velocity of glide at low temperatures and high stresses is given by Arrhenius form:

$$\langle v \rangle = \frac{A^*}{B} \exp[-u(\beta - \beta_0)] \quad (\text{VII } 7)$$

or

$$\langle v \rangle = \frac{A^*}{B} \exp[+u\beta - u(\frac{\beta_0}{\beta_c} - 1)] \quad (\text{VII } 8)$$

Using the approximation

$$\ln(\frac{\beta_1}{\beta_c}) \approx \frac{\beta_1}{\beta_c} - 1 \quad (\text{VII } 9)$$

we obtain the stress exponent to be

$$m^* \approx \frac{2}{3} \beta_c \frac{Gb^3}{kT} \quad (\text{VII.10})$$

where  $G$  is the shear modulus and the interaction distance ( $d$ ) has been assumed to be equal to one Burger's vector. The equation (VII.10) is obtained for a particular dislocation-obstacle interaction form. For other types of interaction similar result can be obtained. Equation (VII.10) indicates that the stress exponent  $m^*$  is an inverse function of temperature and is directly proportional to the obstacle strength. The stress exponent  $m^*$  as a function of the inverse of the temperature is shown in Figure 41, following the data given in reference 51. The plot gives a straight line through the data points as demanded by equation

(VII.10). The same type of behaviour is observed for other materials<sup>61-65</sup>. This plot can be used to estimate the obstacle strength  $\beta$ . Using the values of  $b$  and  $G$  for MgO, we estimate from the slope of Figure 41 the obstacle strength to be of the order of 0.1.

The same material was deformed in a special tensile stage inside the HVEM to determine the distribution of the distance between the obstacles<sup>62</sup>. The obstacles to the dislocation motion are believed to be clusters of impurities having sizes of the order of 20 Å. The distribution of segment lengths of screw dislocations obtained from specimens of MgO single crystals by Appel et al.<sup>62</sup> is shown in Figure 42. The histogram obtained through computer simulation of dislocation motion in arrays containing 2000 points is also shown in the figure. This data was obtained from the thermally activated glide of dislocations through point obstacles of strength  $\beta_c = 0.1$ , at a temperature of  $T^* = 0.01$  and stress  $\tau^* = 0.005$ . The agreement between computer simulation and experiment as shown in Figure 42 is excellent. The density of obstacles estimated from  $l_s = \langle l \rangle_{\text{measured}} / \langle l^* \rangle_{\text{computer}}$  matches with the impurity concentration closely.

Munjal and Ardell<sup>55</sup> investigated the effect of the width of the  $\gamma'$  particle size distribution on the CRSS of Ni-Al single crystals containing 6 wt.-% Al. The samples were given two-step aging treatments to produce broader unimodal distributions than those resulting from isothermal aging. By changing the width of the distribution by 30% they observed a decrease in CRSS by 8%. The size distribution of  $\gamma'$  (Ni<sub>3</sub>Al) particles was obtained by TEM and the breaking

angles were calculated according to the procedure given by Ham<sup>89</sup>. The average angle  $\psi_m$  was approximated to be in the range of  $3\pi/8$ . The computer simulation data using uniform distribution of angles, as obtained by Foreman and Makin<sup>33</sup> and in this study, is given in Figure 30. The CRSS in the range of  $\psi_m = 3\pi/8$  shows very little decrease with the changes in the width of the distribution, suggesting that the computer simulation and experiment is not in agreement. However, since the obstacle strength is usually taken to be proportional to the precipitate size<sup>49-50</sup> and since the distribution of angles discriminates against the weak obstacles, a more reasonable approximation to the distribution of the particle sizes is the uniform distribution of obstacle strengths rather than the angles. The CRSS for the distribution of obstacle strengths is shown in Figure 32, where  $\tau^*$  is a decreasing function of the width of the distribution in the range of  $\psi_m = 3\pi/8$ . One-to-one correspondence between computer simulation and the experiment in this case is difficult, partly because the precipitates are ordered and dislocations travel in pairs and also, the average particle size and the volume fraction change from experiment to experiment. Also the scatter in the computer simulation data makes the comparison more difficult. However, by taking the calculated distributions of angles given by Munjal and Ardell<sup>55</sup> and performing computer simulation through randomly distributed point obstacles the CRSS changed by 4 to 6%, which is close to the experimentally observed value. The experimental data is in accord with the computer simulation studies on at least two accounts: First of all, the CRSS decreases with the width of the distribution of angles and secondly the experimental data show a small decrease with the width of the distribution compared

to the effect of average size. The prediction, equation (V.162), also suggests that the CRSS is mainly determined by the average value of the obstacle strength.

Similar approaches have been taken by Melander<sup>91</sup> who used the lower order approximations to the CRSS (equation (V.75)) and applied it to the experimentally determined particle size distributions for copper alloys containing silica particles obtained by Ashby and Ebeling<sup>92, 93</sup>. Using similar approach, the strength of a precipitation hardened AlZnMg alloy was also calculated recently<sup>94</sup> and good agreement was found between theory and experiment.

## VIII. SUMMARY AND CONCLUSIONS

The major objectives of investigations on dislocation mechanisms are to provide a basic understanding of the varied plastic behaviour of materials and to utilize these concepts in engineering applications. The primary goal of this research was to calculate the CRSS as a function of the strength of the obstacles and to determine the dislocation velocity as functions of temperature and applied stress and strength of the obstacles. A computer model was used to directly simulate glide under precisely controlled conditions and compared the results with analytical predictions and experimental data.

From the study of the effects of the array size and shape the following conclusions can be drawn:

i) The CRSS for athermal glide obtained in simulating finite size arrays depends on the array size and shape and decreases as the width of the array increases or the height of the array decreases.

ii) The array-to-array scatter in the properties of the strongest configuration still exists even with large arrays.

iii) The velocity of a dislocation in thermally activated glide will depend on the array size and increases as the size of the array increases.

iv) The CRSS is also dependent on the boundary conditions (mirror or periodic) for arrays of small size.

v) Since the microstructural obstacle arrays of physical interest are finite, the variation of glide properties with the size of the array should be taken into account in physical theories.

Since most of the obstacles in real materials have distribution of strengths, we have made analytical and computer simulation studies of dislocation motion through arrays containing distribution of obstacle strengths. Mixture of obstacles change the properties of the strongest configuration drastically, especially in the case of two kinds of obstacles. The effects are more pronounced when the array contains a lot of weak and a few strong obstacles. We have calculated the CRSS, average segment length, the fraction of obstacles on the configuration and distribution of forces and obtained good correlations with computer simulation data. We have also demonstrated that in the case of superposition of two mechanisms the addition of stresses does not hold in the ranges of obstacle strengths studied and in general the CRSS can be calculated using the quadratic sum of the stresses, i.e.  $\tau^2 = \sum_i \tau_i^2 x_i$ . Thermally activated dislocation glide through two types of obstacles have also been considered and the effects of the temperature on the strength-determining configuration is studied through computer simulation.

The comparison of the computer simulation results with experiment was carried out in the last section. The dislocation motion through irradiated Cu is compared to computer simulation of dislocation glide through randomly distributed obstacles and very good agreement is found. Quantitative comparison of the segment length distributions of gliding dislocations obtained from computer simulation and hardened Cu single crystal showed very good agreement. The stress exponent is shown to depend inversely with the temperature which has been observed experimentally. The distribution of segment lengths obtained

from MgO single crystal containing impurities matched very closely the computer simulation histogram. The results compared with the experimental data obtained from a precipitation hardened alloy also showed good agreement.

## **ACKNOWLEDGEMENTS**

The author is indebted gratefully to Professor J.W. Morris, Jr. for his continuous guidance and encouragement throughout this study. My sincere thanks to Dr. K. Hanson and to Professor A. J. Ardell of the Materials Department in UCLA for useful discussions, to Professors J. Washburn and F. E. Hauser for reviewing the manuscript, to Gloria Pelatowski for drawing the figures.

This work was supported by the Department of Energy through the Materials and Molecular Research Division of the Lawrence Berkeley Laboratory and by the National Science Foundation through Grant# DMR 75-08163.

## REFERENCES

1. Reported by Th. von Karman, *Enzykl. d. Math. Wiss.*, IV.4, p.767, (1913).
2. L. Prandtl, *Z. Angew. Math. Mech.* **8**,85, (1928).
3. U. Dehlinger, *Ann. Phys.* **2**,749, (1929).
4. E. Orowan, *Z. Physik*, **89**,614, (1934).
5. E. Orowan, *Z. Physik*, **89**,634, (1934).
6. M. Polanyi, *Z. Physik*, **89**,660, (1934).
7. G. I. Taylor, *Proc. Roy. Soc. London*, **A-145**,362, (1934).
8. R. Becker, *Z. Physik*, **26**,919, (1925).
9. E. Orowan, *Z. Physik*, **89**,605, (1934).
10. E. Orowan, *Proc. Phys. Soc.* **52**,8, (1940).
11. W. Kauzmann, *Trans. AIME*, **143**,57, (1941).
12. A. Seeger, *Z. Naturf.*, **9A**,758, (1954).
13. J. Friedel, *Les Dislocations*, Gauthier-Villars, Paris, (1956),  
*Dislocations*, Addison-Wesley, New York, (1964).
14. J. Friedel, in *Electron Microscopy and Strength of crystals*, G. Thomas and J. Washburn, eds., Interscience Publishers, New York (1963), p. 605.
15. U. F. Kocks, A. S. Argon and M. F. Ashby, *The dynamics of Slip*, *Prog. Mat. Sci.*, **19**,1, (1975).
16. F. R. N. Nabarro, in *The Physics of Metals*, P. B. Hirsch, ed. Cambridge University Press, Cambridge (1975), vol.2, p152.

17. F. R. N. Nabarro, *J. Less Common Metals*, **28**, 257, (1972).
18. U. F. Kocks, Report after an International Workshop, Cornell University, (1976).
19. N. F. Mott, in *Imperfections in Nearly Perfect Crystals*, Schocley et al., eds., John Wiley, New York (1952).
20. N. F. Mott and F. R. N. Nabarro, *Report of a Conference on Strength of Solids*, The Physical Society, London, (1948), p.1.
21. R. Labusch, *Acta Met.*, **20**, 917, (1972).
22. F. R. N. Nabarro, *Phil Mag.*, **35**, 613, (1977).
23. A. J. E. Foreman and M. J. Makin, *Phil. Mag.*, **14**, 911, (1966).
24. J. W. Morris, Jr. and C. K. Syn, *J. Appl. Phys.*, **45**, 961, (1974).
25. J. W. Morris, Jr. and D. H. Klahn, *J. Appl. Phys.*, **44**, 4882, (1973).
26. E. Orowan, *Symposium on Internal Stresses*, Inst. Metals, London, (1947), p.451.
27. R. Labusch, *Z. Physik*, **167**, 452, (1962).
28. P. L. Fleischer, *Acta Met.*, **10**, 835, (1962).
29. P. L. Fleischer and W. R. Hibbard, in *The Relation Between the Structure and Mechanical Properties of Metals*, Her Majesty's Stationary Office, London, (1963), p.262.
30. U. F. Kocks, *Phil. Mag.*, **13**, 541, (1966).

31. T. Stefansky and J. E. Dorn, Trans. AIME.,**245**,1869,(1969).
32. J. E. Dorn, P. Guyot, and T. Stefansky, in *Physics of Strength and Plasticity*; A. S. Argon, ed.,MIT Press, Cambridge, (1969), p.133.
33. A. J. E. Foreman and M. J. Makin, Can. J. phys., **45**,571,(1967).
34. A. J. E. Foreman, P. B. Hirsch and F. J. Humphries, *Fundamental Aspects of Dislocation Theory*, NBS Publ.#317, (1970) ,vol.2, p.1083.
35. R. O. Scattergood and E. S. P. Das, Nuclear Metallurgy, **20**, 740 (1976).
36. R. S. W. Shewfelt and L. M. Brown, Phil. Mag., **35**,945,(1977).
37. D. H. Klahn, D. Austin, A. K. Mukherjee, and J. E. Dorn, in *Advances In Applied Probability*, Supplement 2, (1973), p.112.
38. S. I. Zaitsev and E. M. Nadgornyi, Sov. Phys. Solid State, **15**,1777,(1974).
39. R. J. Arsenault and T. Cadman, in *Rate Processes in Plastic Deformation of Materials*, J. C. M. Li and A. K. Mukherjee, eds., ASM, #4, (1975), p.102.
40. R. J. Arsenault and T. Cadman, phys. stat. sol., (**a**)**24**,299, (1974).
41. J. W. Morris, Jr. and D. H. Klahn, J. Appl. Phys.,**45**,2027, (1974).
42. S. Altintas, K. Hanson, and J. W. Morris, Jr., J. Eng. Mater. Techn. (Trans. ASME H), **98**, 86, (1976).
43. S. Altintas, K. Hanson, and J. W. Morris, Jr., in *Proceedings of the Second International Conference on Mechanical Behavior of Materials*, Boston, Mass., (1976), p.2.
44. K. Hanson and J. W. Morris, Jr., J. Appl. Phys., **46**,983, (1975).

45. K. Hanson and J. W. Morris, Jr., *J. Appl. Phys.*, **46**,2678, (1975).
46. U. F. Kocks, *Trans. Japan. Inst. Metals, Supplement*, **9**,1, (1968).
47. T. J. Koppelaar and D. Kuhlmann-Wilsdorf, *Appl. Phys. Letters*, **4**, 59,(1964).
48. A. Kelly and R. B. Nicholson, *Precipitation Hardening*, *Progr. in Mat. Sci.*,**10**,1,(1963).
49. L. M. Brown and R. K. Ham, in *Strengthening Methods in Crystals*, A. Kelly and R. B. Nicholson, eds., Applied Science Publishers. London, (1971), p 12.
50. R. S. Barnes, in *Flow and Fracture of Metals and Nuclear Environments*, ASTM publ.#380, (1965), p.40.
51. S. N. Val'kovskii and E. M. Nadgornyi, *Sov. Phys. Solid State*, **17**,1733,(1975).
52. F. Appel, H. Bethge, and U. Messerschmidt, *phys. stat. sol.* (**a**)**38**,103,(1976).
53. S. Saimoto, H. Saka and T. Imura, *Scripta Met.*, **11**,903,(1977).
54. S. Saimoto, H. Saka, T. Imura, and N. Yukawa, in *Proceedings of the Fifth Intern. Conference on HVEM*, Kyoto, (1977), to be published.
55. V. Munjal and A. J. Ardell, *Acta Met.* **24**,827,(1976).
56. W. Feller, *An Introduction to Probability Theory and Its Applications*, 2nd ed.,Wiley, New York,(1957), vol.1.

57. I. N. Bronstein and K. A. Semendjajew, *Taschenbuch der Mathematik*, Verlag Harri Deutch, Zurich, (1970), p.117.
58. R. Labusch, submitted to *J. Appl. Phys.* (1977).
59. A. I. Landau, *phys. stat. sol.* (a)**30**,659,(1976).
60. S. I. Zaitsev and E. M. Nadgornyi, *Nuclear Metallurgy*,**20**, 707,(1976).
61. R. J. Arsenault and T. W. Cadman, *Nuclear metallurgy*,**20**,658,(1976).
62. S. I. Zaitsev and E. M. Nadgornyi, *Nuclear Metallurgy*,**20**, 816,(1976)
63. K. Hanson, S. Altintas, and J. W. Morris, Jr., *Nuclear Metallurgy*,  
**20**,917,(1976).
64. D. J. Bacon, U. F. Kocks, and R. O. Scattergood, *Phil. Mag.*,  
**28**,1241,(1973).
65. M. Fine, in *The Relations Between the Structure and Mechanical Properties of Metals*, Her Majesty's Stationary Office, London,(1963), p.299.
66. M. Fine, in *Strengthening of Metals*, D. Peckner, ed., Reinhold Publishing Corp., New York, (1964), p.141.
67. A. Kelly, in *Electron Microscopy and Strength of Crystals*, G. Thomas and J. Washburn, eds., Interscience, New York, (1963), p.947.
68. P. M. Kelly, *Intern. Metal. Rev.*,**18**, 31,(1973).
69. A. Seeger, *Proc. 2nd U. N. Intern. Conference. PUAE*, **6**,250,(1968).
70. J. Diehl, in *Vacancies and Interstitials in Metals*, A. Seeger, D. Schumacher, W. Schilling, and J. Diehl, eds., North-Holland Publ. Co., Amsterdam, (1970), p.739.

71. M. Ruhle, *phys. stat. sol.*, **26**,661,(1968).
72. W. Frank, M. Ruhle, and M. Saxlova, *phys. stat. sol.*, **26**, 671,(1968).
73. J. Diehl, in *Moderne Probleme der Metallphysik*, A. Seeger, ed., Springer-Verlag, Berlin, (1965), vol.1, p.227.
74. Reference 49, p.33.
75. L. M. Brown, *Phil. Mag.*, **15**, 363,(1967).
76. R. O. Scattergood and D. J. Bacon, *phys. stat. sol.*, (**a**)**25**, 395,(1974).
77. R. O. Scattergood and D. J. Bacon, *Phil. Mag.*,**31**,179,(1975).
78. D. J. Bacon and R. O. Scattergood, *J. Phys.* **F4**.2126,(1974).
79. P. M. Kelly, *Scripta Met.*,**6**,647,(1972).
80. M. Nemoto and S. Koda, *Trans. Japan. Inst. Metals*, **7**,235,(1966).
81. A. R. Rosenfield, G. T. Hahn, A. L. Bement, Jr., and R. I. Jaffee, *Dislocation Dynamics*, Mc-Graw Hill, New York, (1968).
82. J. J. Gilman and W. G. Johnson, *J. Appl. Phys.*,**30**,129,(1959).
83. T. Imura, in *Electron Microscopy and Structure of Materials*, G. Thomas, R. M. Fulrath, and R. M. Fisher, eds., University of California Press, Berkeley,(1972), p.104.
84. A. I. Landau and V. I. Dotsenko, *phys. stat. sol.*,(**a**)**37**,709, (1976).
85. P. M. Kelly and J. M. Round, *Scripta Met.*,**3**,85,(1969).
86. J. C. M. Li, *Can. J. Phys.*,**45**,493,(1967).

87. K. R. Evans, D. J. Bailey, and W. F. Flanagan, *phys. stat. sol.*,  
22,607,(1967).
88. U. F. Kocks, *Scripta Met.*, 4,29,(1970).
89. R. K. Ham, *Trans. Japan. Inst. Metals, Supplement*, 9,52, (1968).
90. I. M. Brown, *Scripta Met.*, 9,591,(1975)
91. A. Melander, to be published.
92. A. Melander and P. A. Persson, *Acta Met.*,26.267,(1978).
93. M. F. Ashby and R. Ebeling, *Trans. AIME*,236.1395,(1966).
94. R. Ebeling and M.F. Ashby, *Phil. Mag.*, 13, 805, (1966).

**Table. I. Assumptions and Basic Equations**

<b>Assumptions:</b>		
Obstacles:	randomly distributed, localized and point-like.	
Dislocation:	flexible string, constant line tension.	
<b>Basic Equations:</b>		
Quantity	Dimensional	Dimensionless
Number of Obstacles	$N$	$N$
Total Area	$A$	$A^* = N$
Stress	$\tau$	$\tau^* = \tau l_b / 2\Gamma$
Radius of Bow-out	$R$	$R^* = 1 / (2\tau^*)$
Force on the obstacle	$F$	$\beta = F / 2\Gamma$ $= \cos(\psi/2)$
Obstacle Strength	$F_c$	$\beta_c = \cos(\psi_c/2)$

## FIGURE CAPTIONS

- Figure 1. Schematic illustration of the problem of yield or initial deformation in a grain or single crystal.
- Figure 2. Detail of mechanical equilibrium in the  $i$ -th obstacle configuration.
- Figure 3. Geometry of randomly distributed localized obstacles. (After Friedel<sup>13</sup>).
- Figure 4. Parametrization of the area searched by circle-rolling to an angle  $\theta_c = \pi$ . The parameters  $\theta$  and  $\phi$  define the shaded area  $dA^*$ .
- Figure 5. Division of the search area ( $a$ ) into a limiting area ( $a_0$ ) and the excess area ( $a_1$ ) by the coordinate line  $\phi = -\phi_0$ . The position of obstacle  $k+1$  to be found in area ( $a_0$ ) is defined by the angles  $\theta$  and  $\phi$ .
- Figure 6. Division of the search area into regions I, II, and III.
- Figure 7. Square distribution of the obstacle strengths measured by the critical angle  $\psi_i^*$ .
- Figure 8. Square distribution of the obstacle strengths measured by  $\beta_i$ .
- Figure 9. A possible force-displacement relation,  $\beta(x/d)$ , for dislocation passage through an obstacle, which forms a simple repulsive barrier. The shaded area indicates the activation energy ( $g_i^k$ ) if the dislocation exerts a force  $\beta_i^k$  on the obstacle.

- Figure 10. Dislocation glide through an array containing randomly distributed point obstacles. The dislocation starts at the bottom of the array and moves until the strongest configuration is found.
- Figure 11. Flowchart explaining the essential features of the computer code for finding the athermal critical resolved shear stress.
- Figure 12. Parameters for dislocation motion algorithm: a) division into subarrays, b) bow-out process.
- Figure 13. Athermal glide stress versus array width for arrays containing randomly distributed obstacles of strength,  $\beta_c = 0.01$ .
- Figure 14. The resistance to dislocation glide under a dimensionless stress of  $\tau^* = 0.001$  as a function of size of a square array of identical point barriers.
- Figure 15. The histogram of forces, obtained through direct computer simulation of glide through an array containing  $10^6$  randomly distributed obstacles, compared to theoretical distributions.
- Figure 16. The average segment length,  $\langle l^* \rangle$ , as a function of size of a square array of identical point obstacles of strength  $\beta_c = 0.01$ .
- Figure 17. The comparison of theoretical distribution of average segment lengths with the histogram obtained by computer simulation of an array containing  $10^6$  obstacles at a stress of  $\tau^* = 0.001$ .
- Figure 18. The comparison of theoretical distributions of the angle  $\phi$  to the histogram obtained through computer simulation of an array of  $10^6$  obstacles at a stress of  $\tau^* = 0.001$ .

- Figure 19. Schematic distribution of forces along the strongest configuration.
- Figure 20. The obstacle strength  $\beta_1$  required to prevent athermal glide under given applied stresses ( $\tau^* = 0.005$  and  $0.001$ ) as a function of the width of square arrays. The calculated curve is drawn from equation(VI.6).
- Figure 21. Comparison of theoretical prediction and computer simulation for arrays containing  $10^6$  obstacles at various values of stresses.
- Figure 22. The strength  $\beta_1$  as a function of the width of arrays containing 250,000 obstacles at a stress  $\tau^* = 0.005$  and comparison with equation(VI.6).
- Figure 23. The CRSS for arrays containing two types of obstacles as a function of the fraction of weak obstacles.
- Figure 24. The CRSS for arrays containing two kinds of barriers as a function of the fraction of strong obstacles,  $x_s$ : a) For obstacle strengths  $\beta_s = 0.1$ ,  $\beta_w = 0.05$ , b) for obstacle strengths  $\beta_s = 0.05$ ,  $\beta_w = 0.01$  c) for obstacle strengths  $\beta_s = 0.1$ ,  $\beta_w = 0.01$ .
- Figure 25. The CRSS for arrays containing two types of obstacles as a function of array size.
- Figure 26. The CRSS for arrays containing mainly weak obstacles as a function of the fraction of strong obstacles ( $x_s \leq 10\%$ ).

- Figure 27. The CRSS for arrays containing a lot of weak, a few strong obstacles ( $x_s \leq 1\%$ ), as a function of the fraction of strong obstacles.
- Figure 28. The fraction of strong obstacles on the strongest configuration ( $c_s$ ), as a function of the fraction of strong obstacles in the array,  $x_s$ : a) for  $\beta_s=0.1$  and  $\beta_w=0.05$ , b) for  $\beta_s=0.05$  and  $\beta_w=0.01$ , and c) for  $\beta_s=0.1$  and  $\beta_w=0.01$ .
- Figure 29. The average segment length,  $\langle l^* \rangle$  as a function of the fraction of strong obstacles,  $x_s$ : a) for  $\beta_s=0.1$  and  $\beta_w=0.05$ , b) for  $\beta_s=0.05$  and  $\beta_w=0.01$ , and c) for  $\beta_s=0.1$  and  $\beta_w=0.01$ .
- Figure 30. The CRSS for arrays containing obstacles whose strength is distributed according to Figure 7, as a function of the width of the distribution  $\psi_w$  and the mean value,  $\psi_m$ .
- Figure 31. Same as Figure 28, but  $\pi/2 \leq \psi_m \leq \pi$ .
- Figure 32. The CRSS for arrays containing obstacles with square distribution of strengths as a function of  $\psi_w$  and  $\psi_m$ .
- Figure 33. Same as Figure 29, but  $\pi/2 \leq \psi_m \leq \pi$ .
- Figure 34. Average segment length for arrays containing obstacles with square distribution of strengths as a function of  $\psi_w$  and  $\psi_m$ .
- Figure 35. Distribution of forces along the strongest configurations in arrays containing obstacles whose strengths is distributed according to Figure 8.

Figure 36. The stress at a given glide velocity as a function of temperature for arrays containing one kind and two kinds of obstacles.

Figure 37. The variation of stress at a given velocity as a function of temperature, for arrays containing relatively large number of weak obstacles.

Figure 38. The fraction of strong obstacles,  $c_s$  in arrays containing two types of obstacles, as a function of the inverse of temperature. The strongest configurations encountered during glide are also shown for high temperature (left), and for low temperature (right). The small circles represent strong obstacles whereas the weak obstacles are indicated by dots.

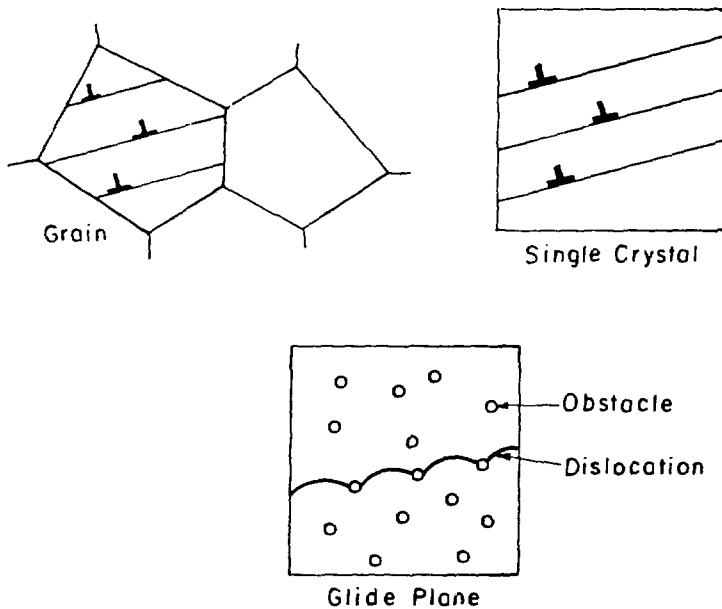
Figure 39. Comparison of the characteristics of gliding dislocations through obstacles between experiment (left) and computer simulation (right). The dislocation motion through irradiation-induced defects as seen in Transmission Electron Microscope (TEM) is taken from the work by Barnes<sup>50</sup> in England.

Figure 40. Comparison between computer simulation and experimental distribution of free segment lengths along gliding dislocations in hardened copper single crystals. Experimental data from High Voltage Electron Microscope in situ deformation studies by Saimoto, Saka, and Imura<sup>53</sup> in Japan.

Figure 41. Comparison of predicted temperature dependence of stress exponent with experimental data obtained on MgO single

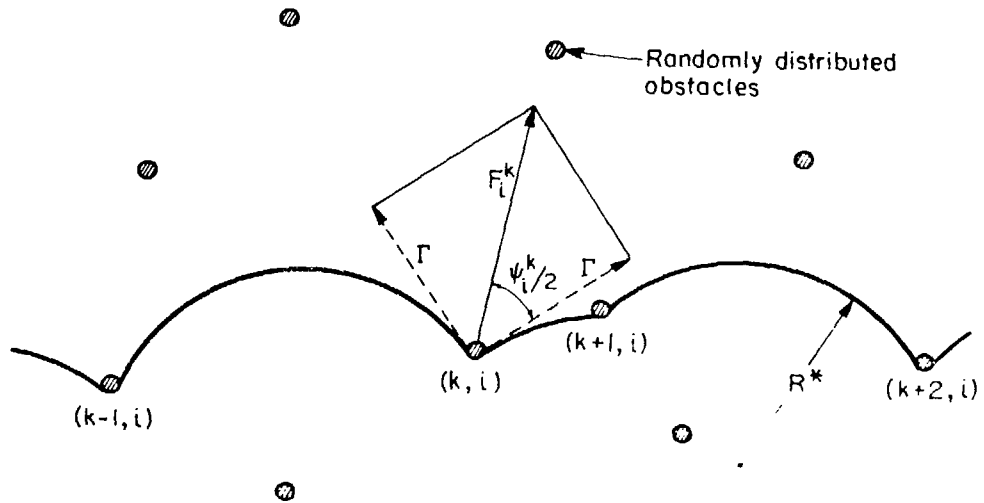
crystals by Val'kovskii and Nadgornyi<sup>51</sup> in Soviet Union

Figure 42. Comparison between computer simulation and experimental distribution of segment lengths along gliding dislocations in MgO. Experimental data from in situ HVEM studies by Appel, Bethge and Messerschmidt<sup>52</sup> in East Germany



XBL 784-4906

Figure 1



XBL732-5721

Figure 2

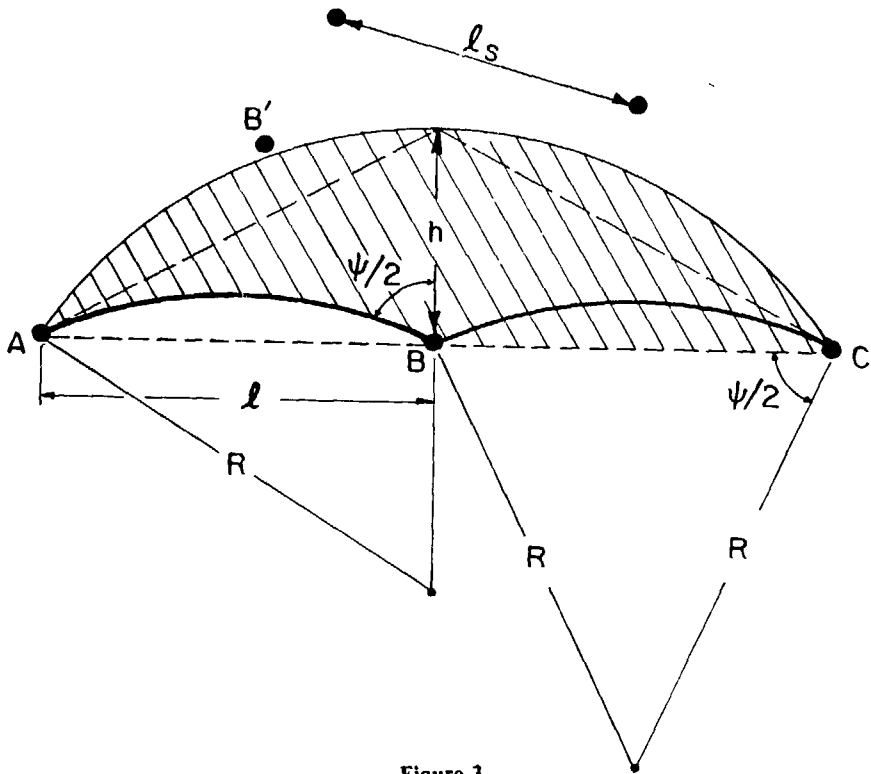
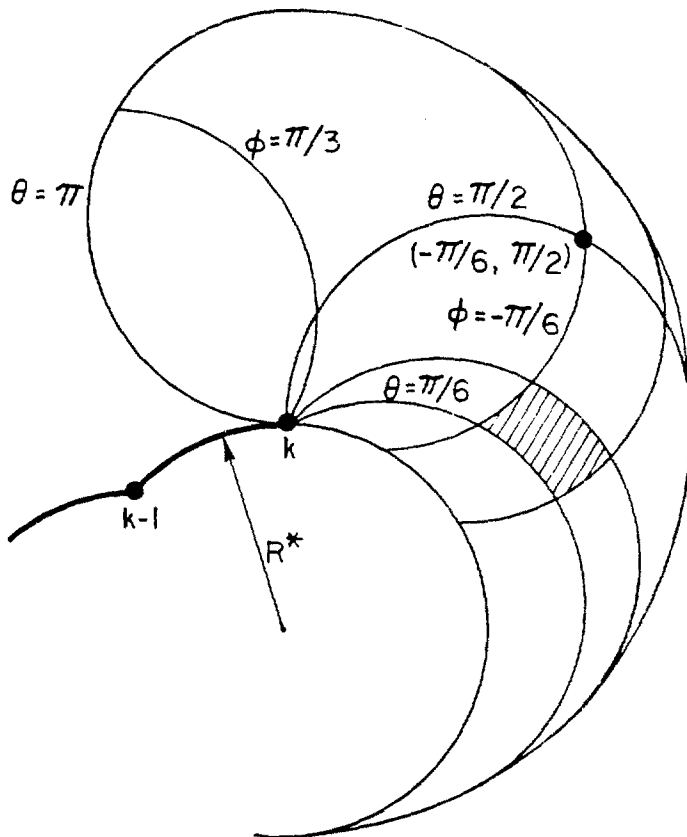


Figure 3

XBL784-4907



XBL 784-4910

Figure 4

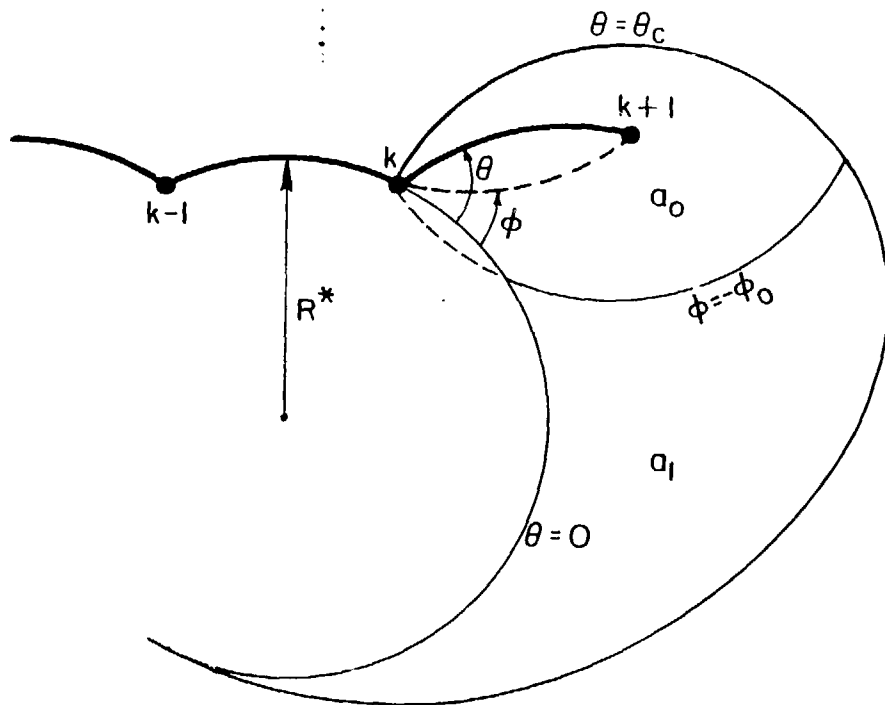


Figure 5

XBL 784-4909

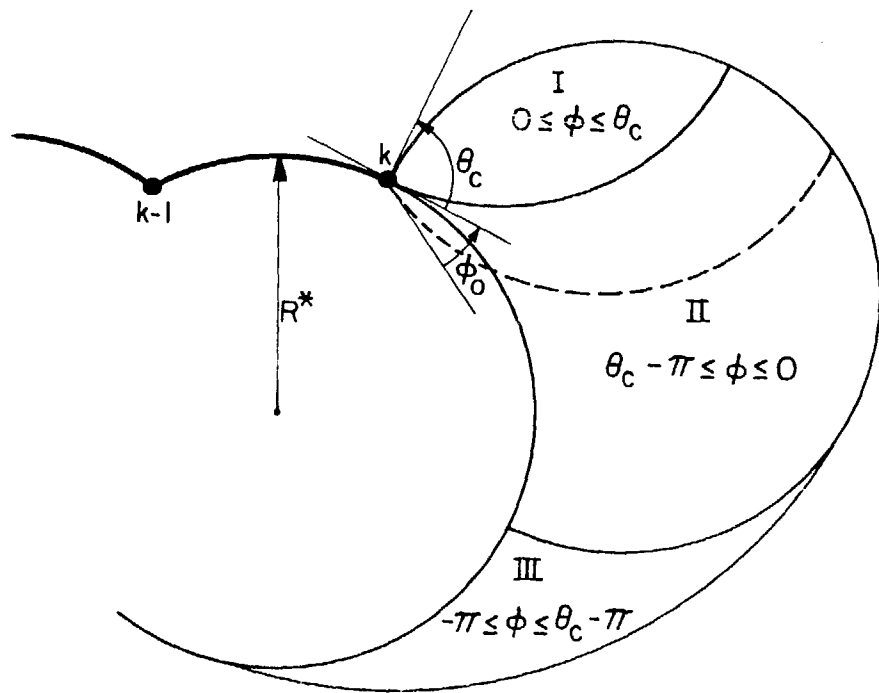


Figure 6

XBL 784-4908

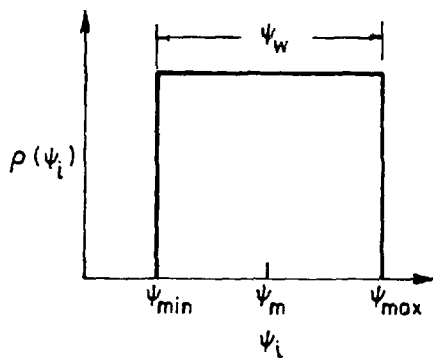
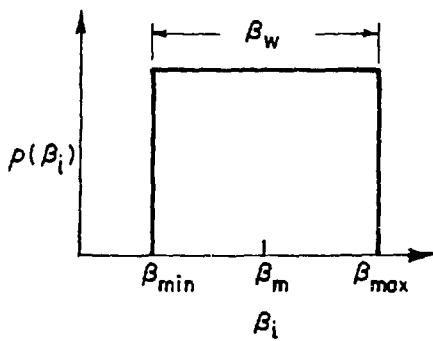
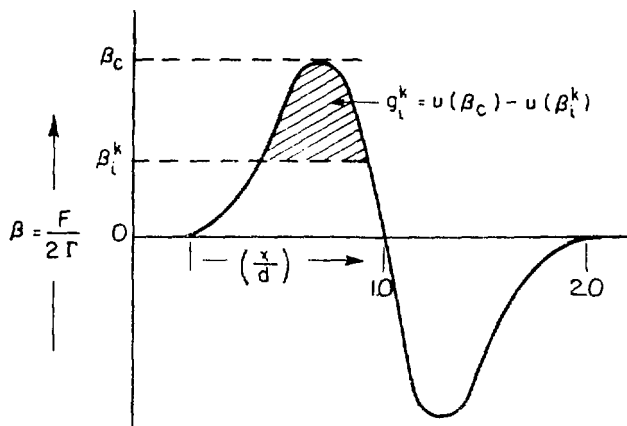


Figure 7

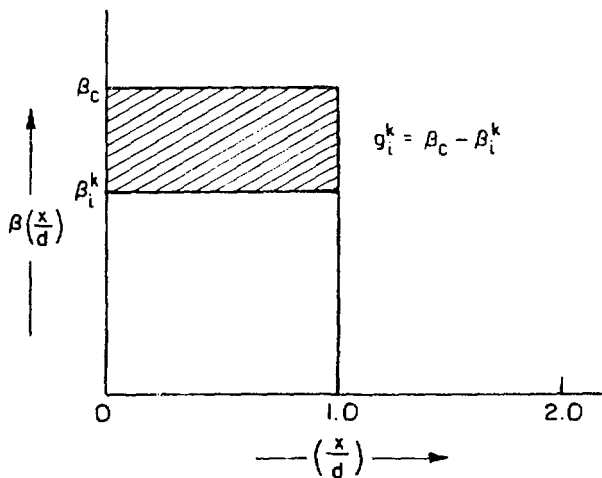


XBL 784-4905

Figure 8



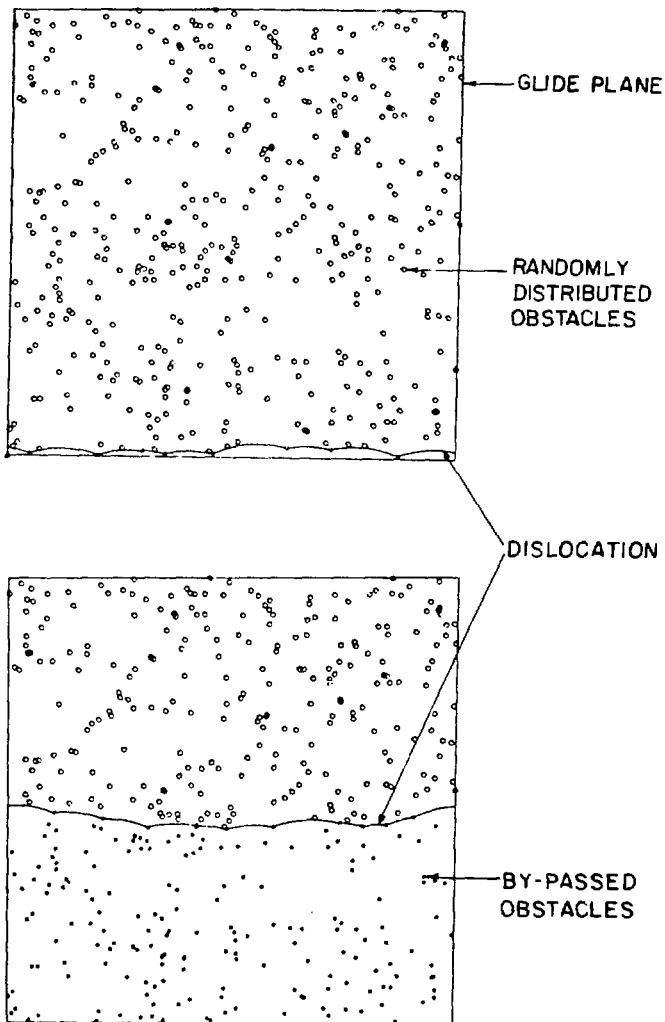
(a)



(b)

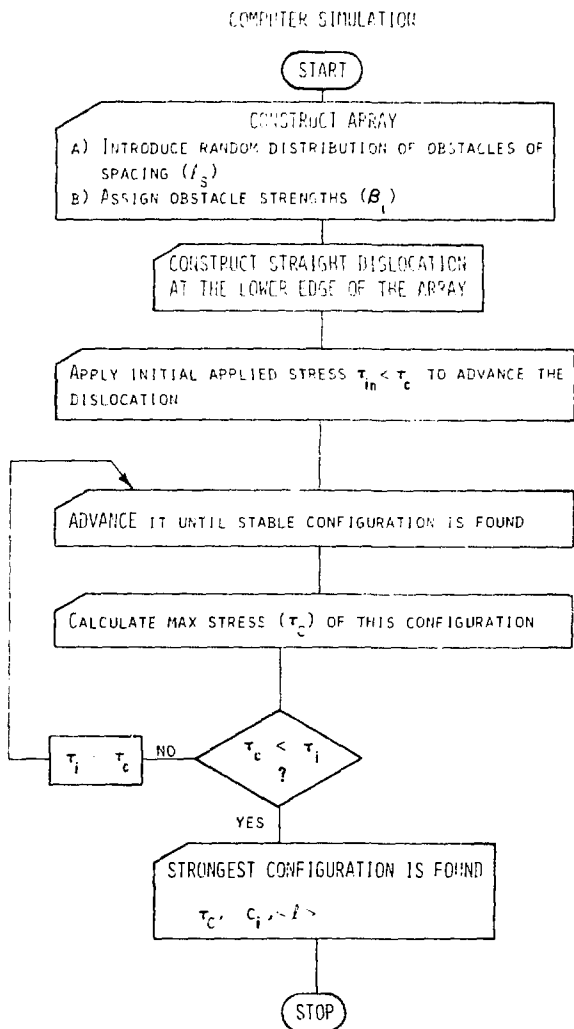
XBL 75 4-6131

Figure 9



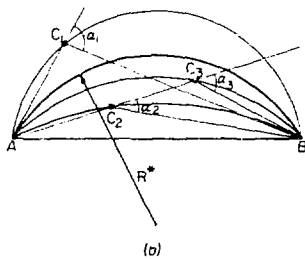
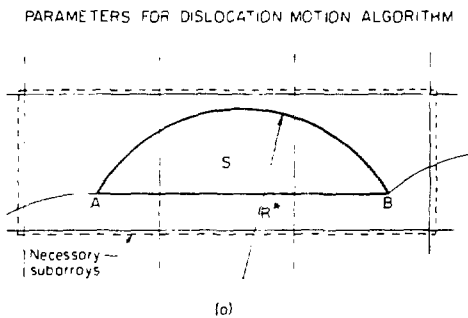
XBL 782-7314A

Figure 10



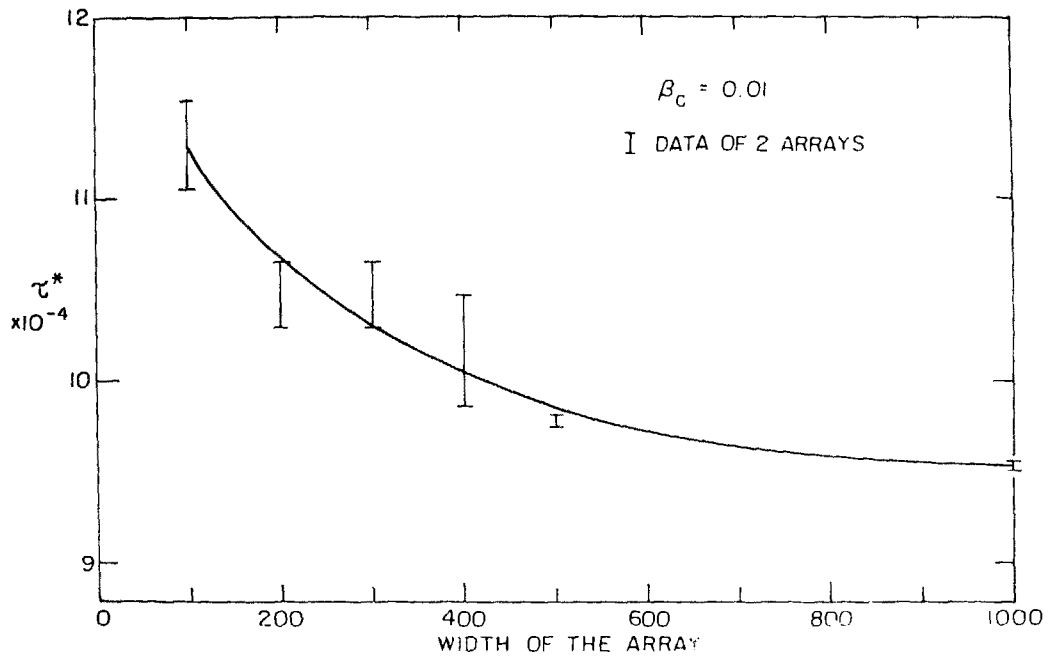
XBL 762-6466

Figure 11



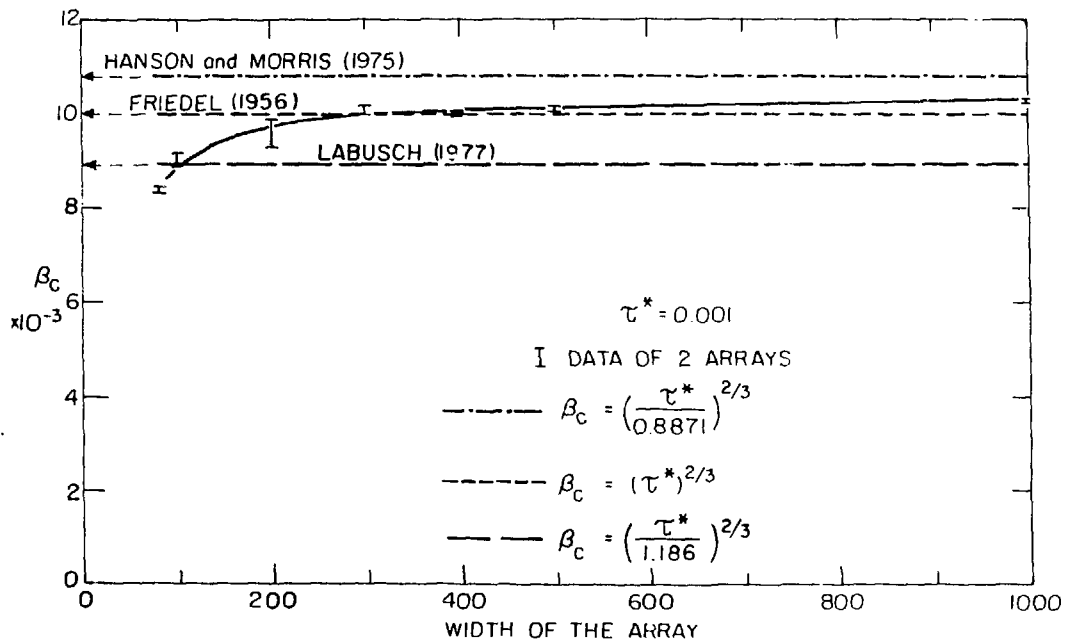
xBL 764-6677

Figure 12



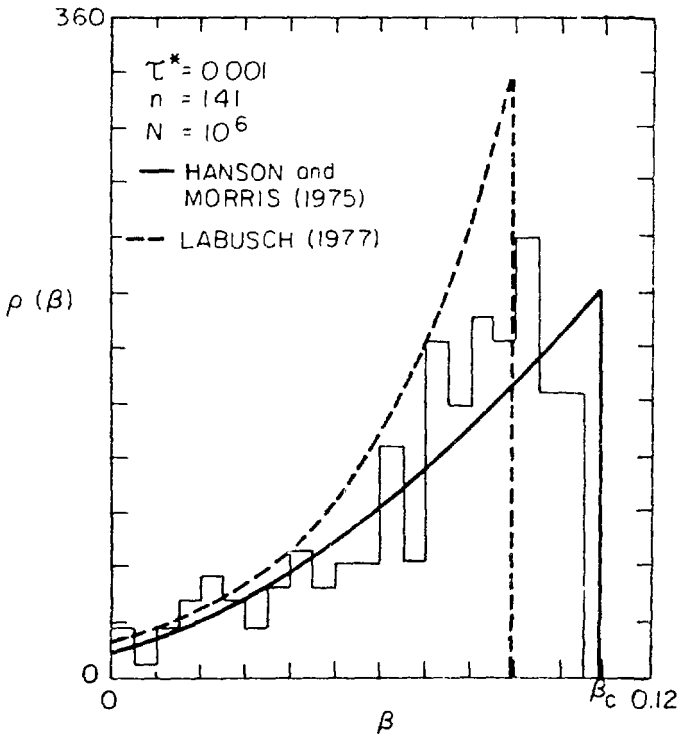
XBL 762-6439

Figure 13



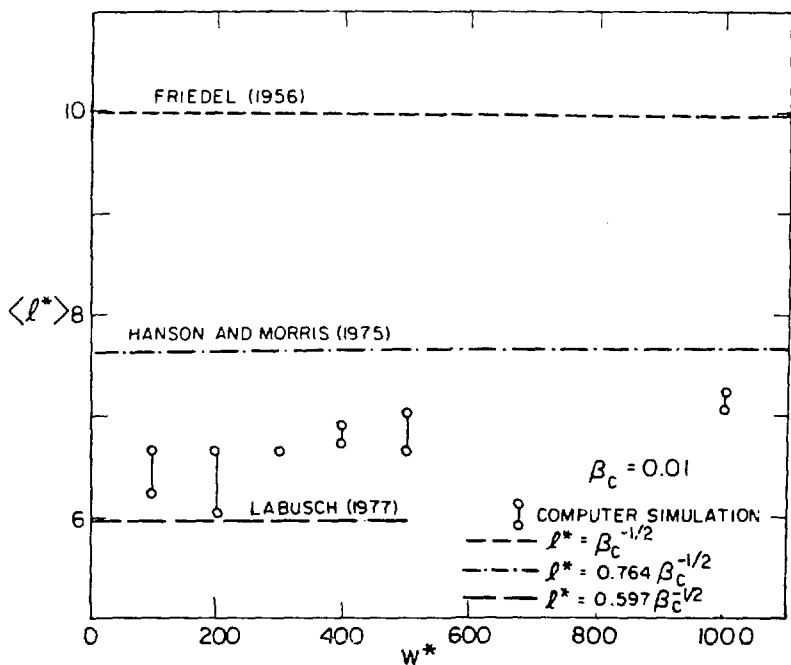
XBL 762-6438 B

Figure 14



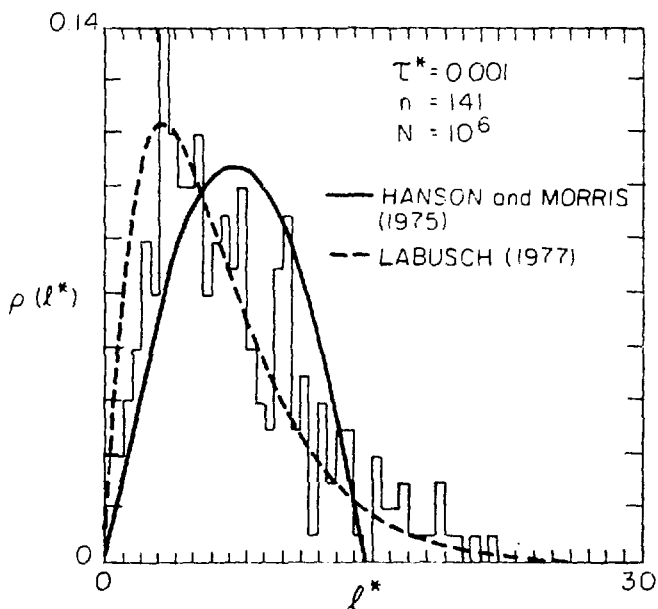
XBL 7610-7644 A

Figure 15



XBL775-5438B

Figure 16



XBL 7610-7645 B

Figure 17

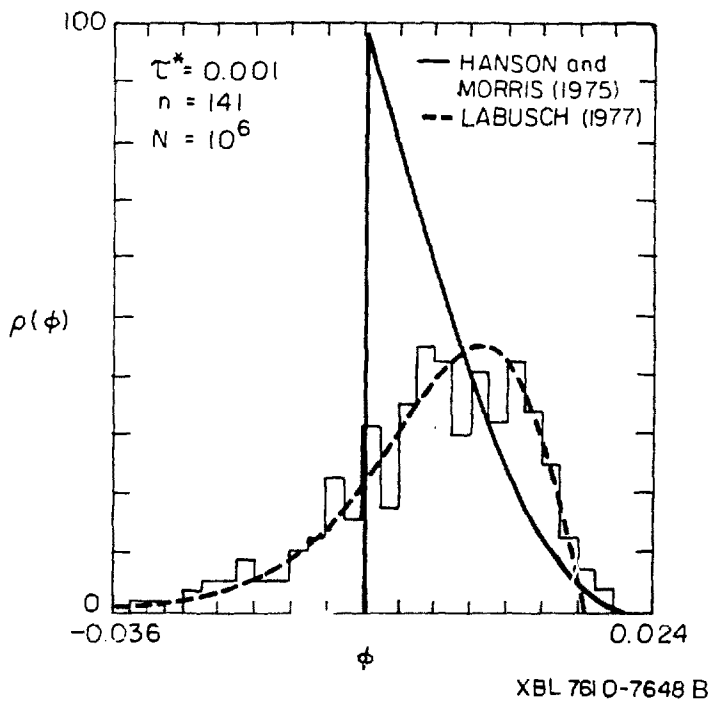
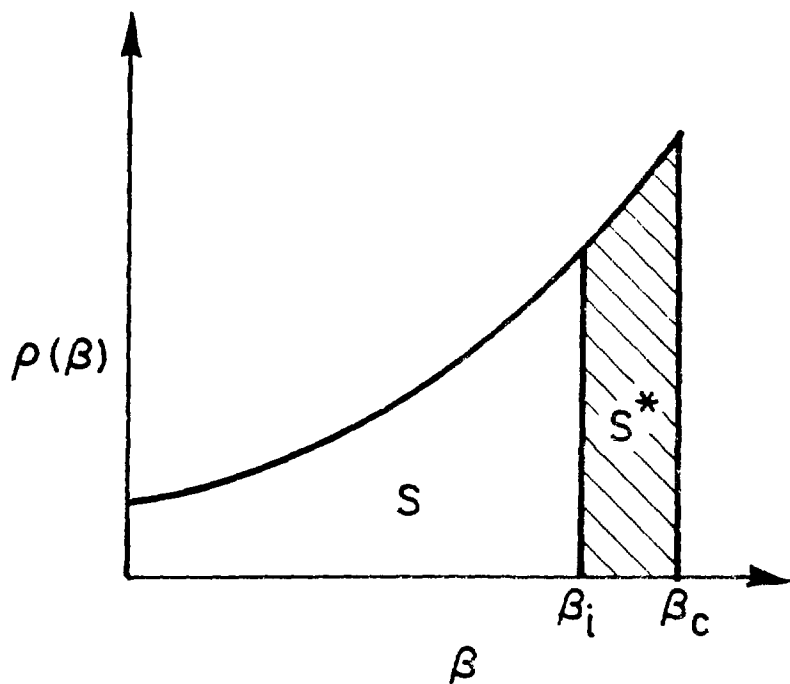
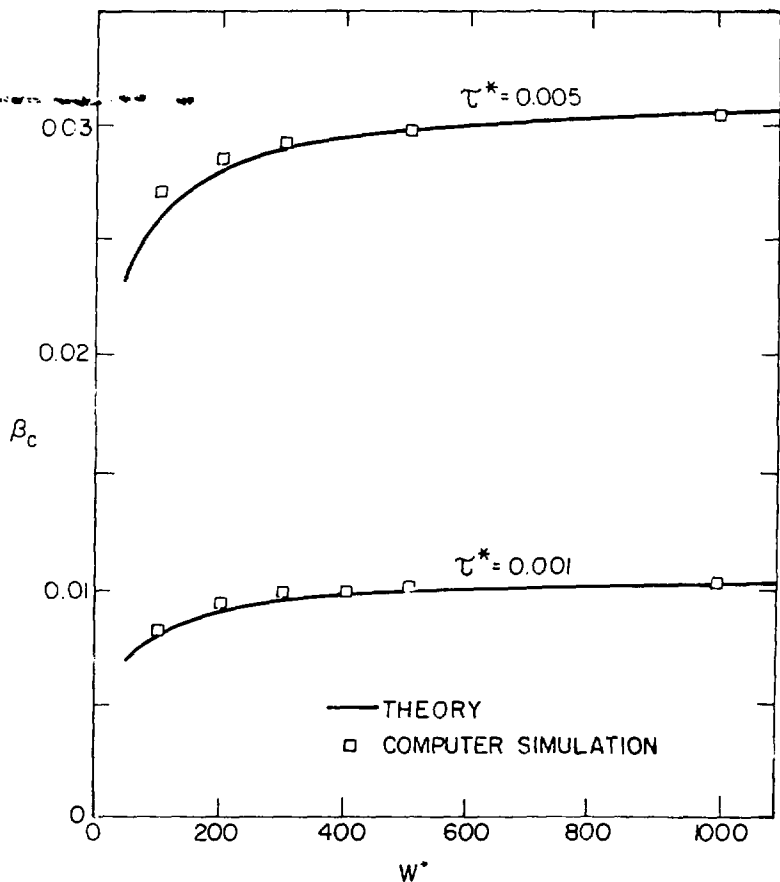


Figure 18



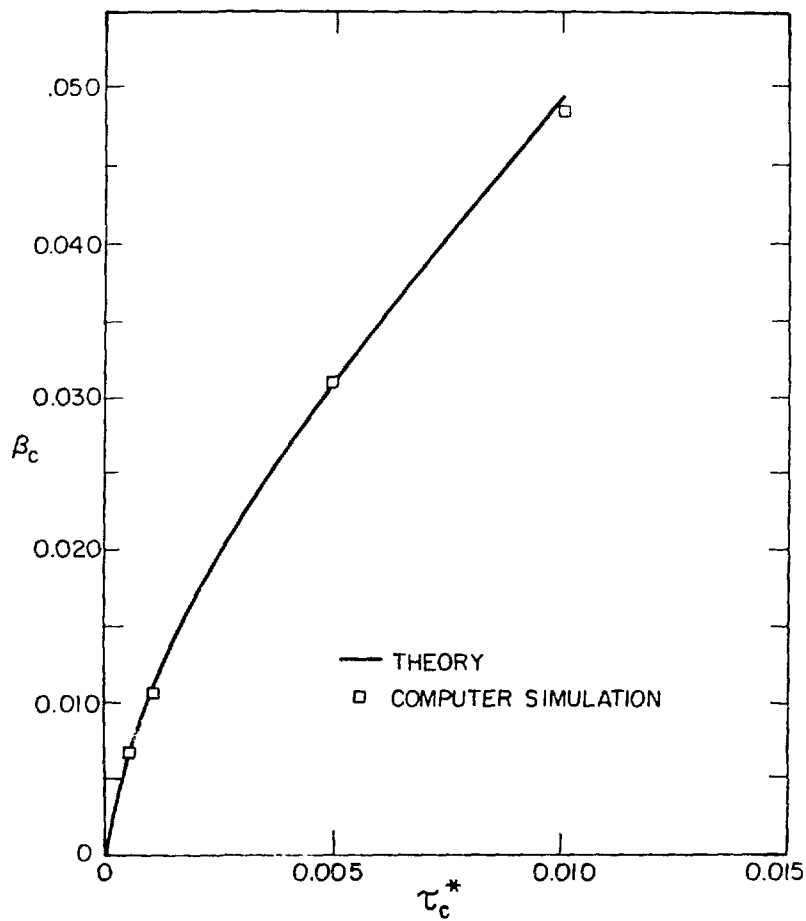
XBL 784-4904

Figure 19



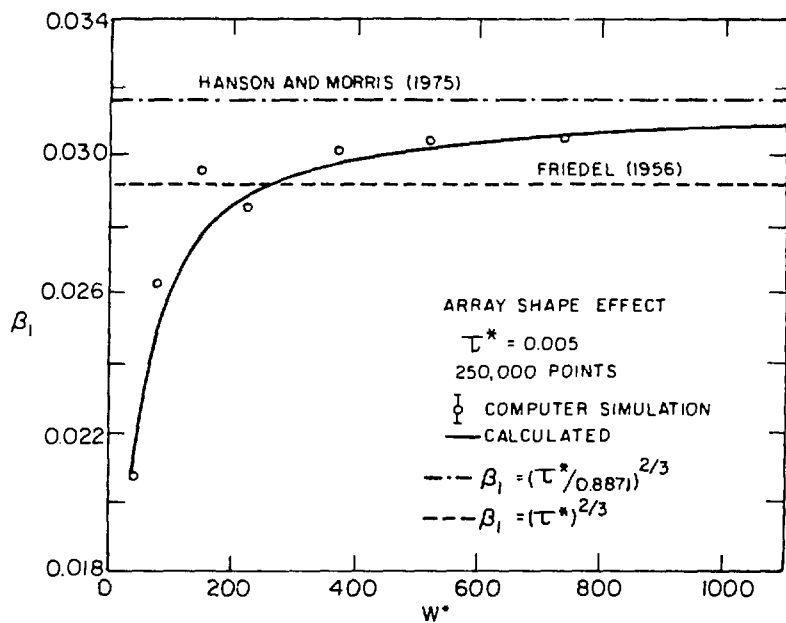
XBL 771-912A

Figure 20



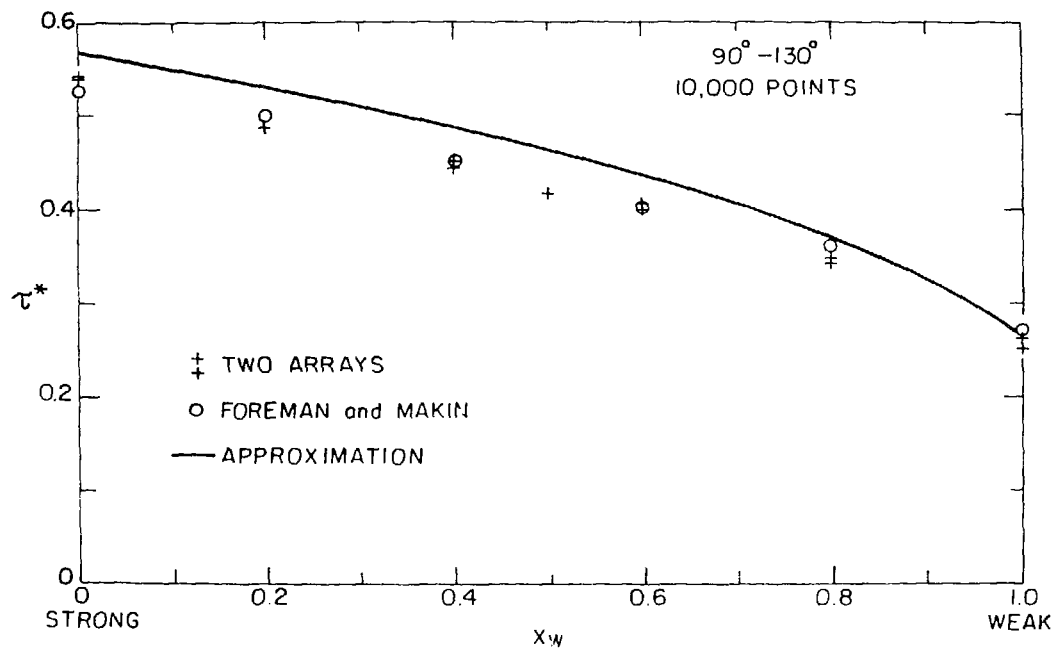
XBL 771 -4911

Figure 21



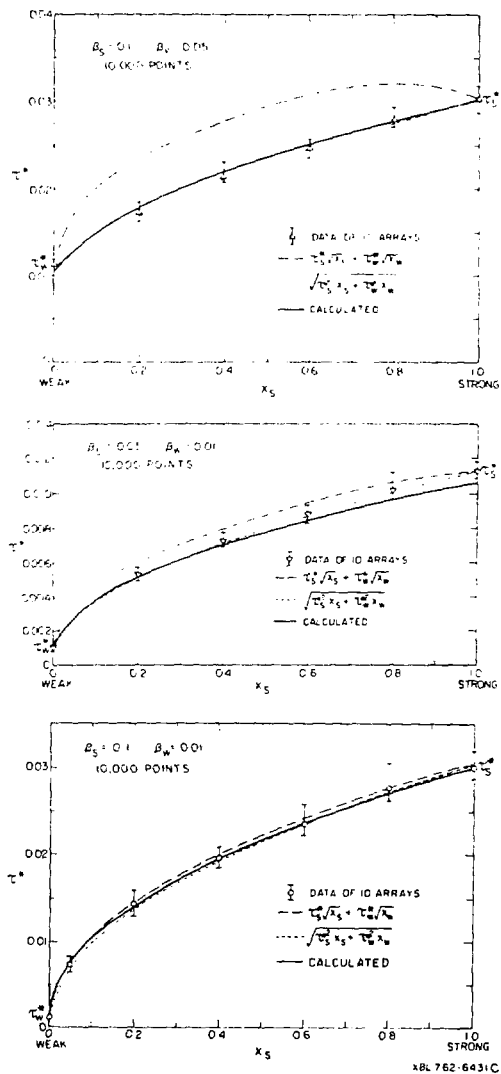
XBL 775-5439A

Figure 22



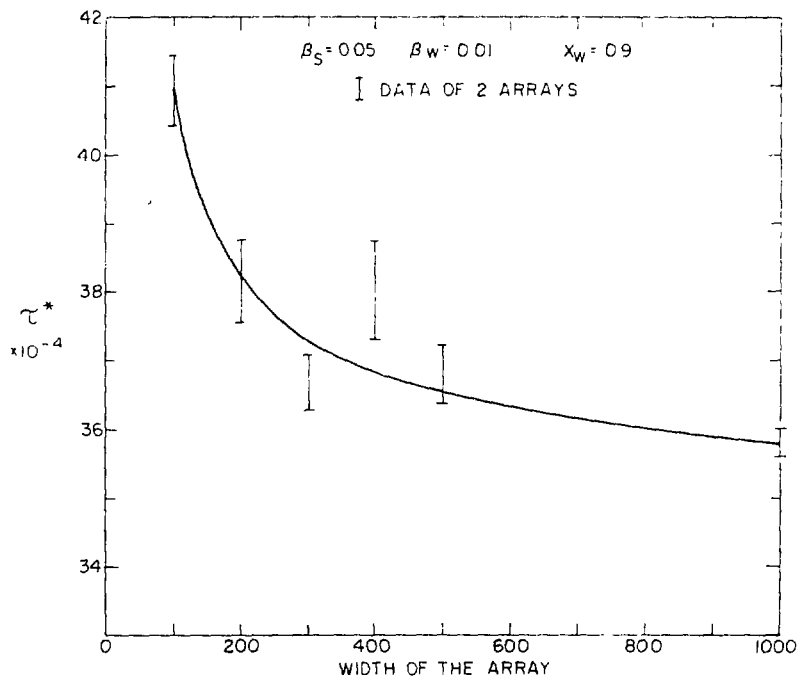
xBL 762-6428

Figure 23



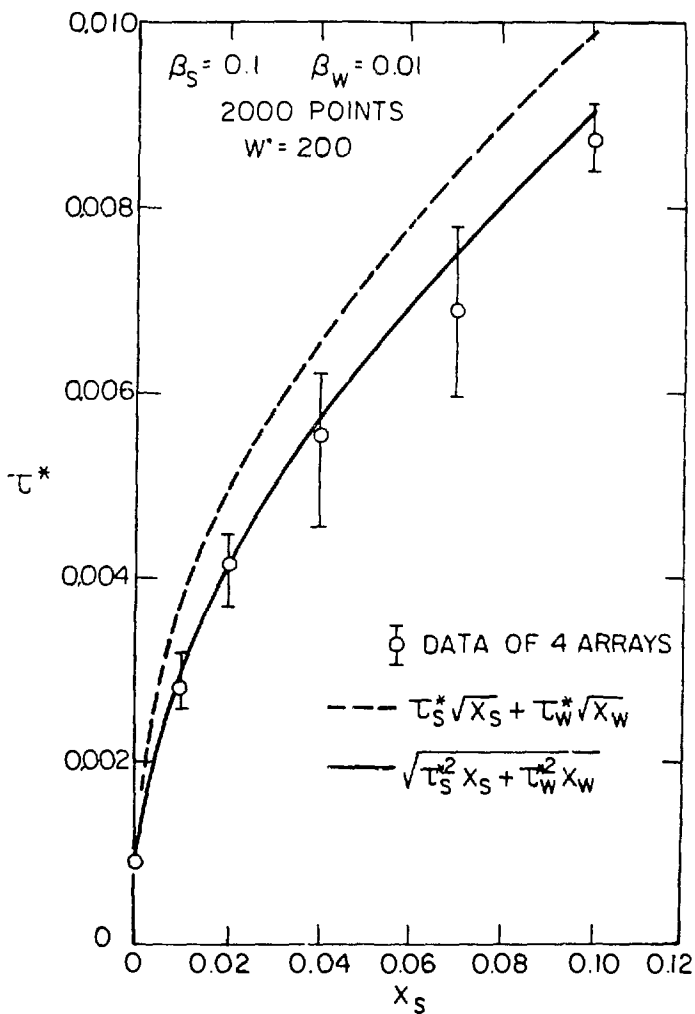
NBL 762-6431C

Figure 24



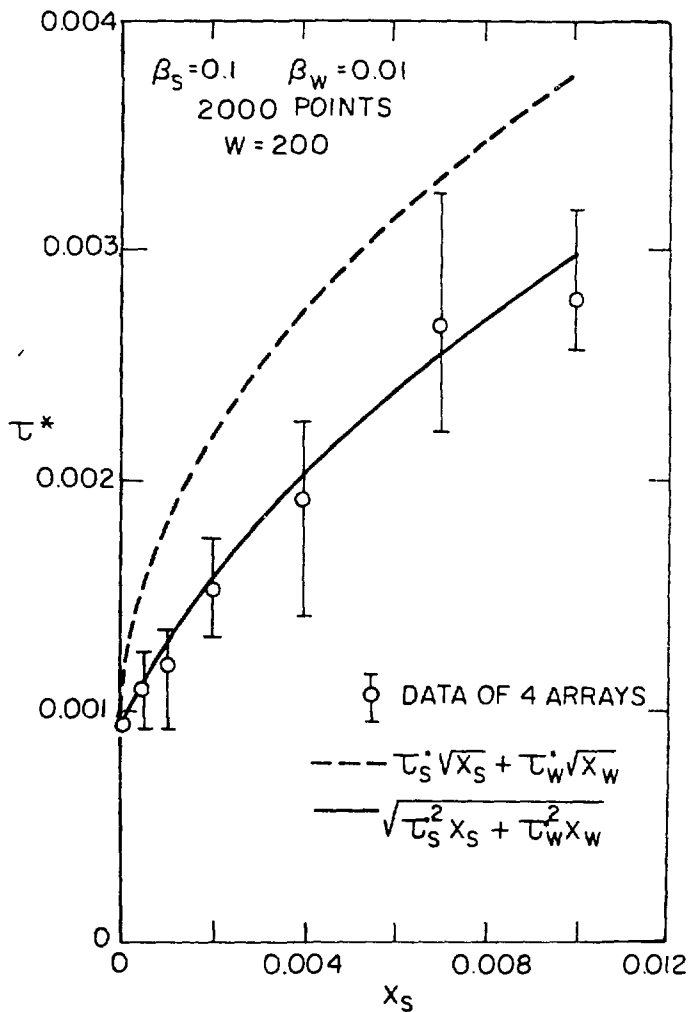
XBL 762-6443

Figure 25



XBL 775-5440A

Figure 26

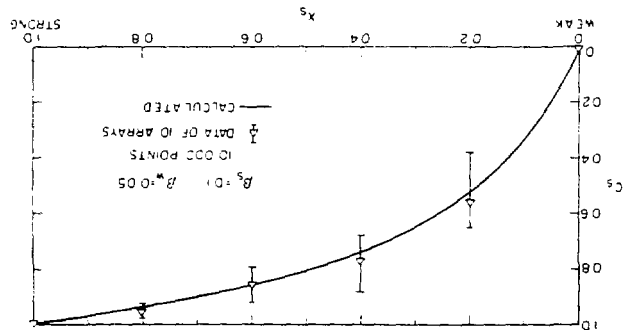
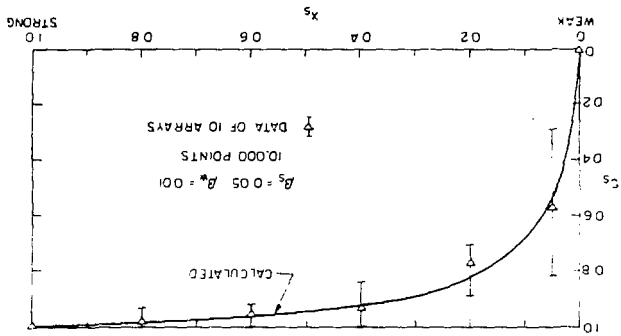
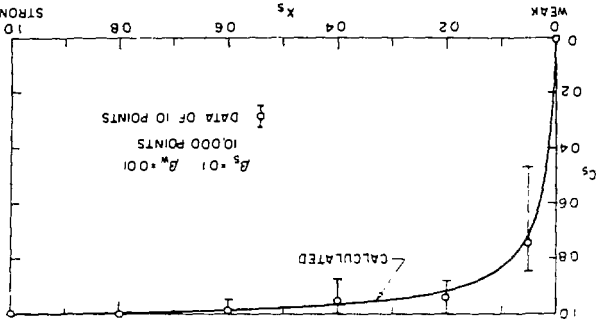


XBL 775-5441A

Figure 27

Figure 28

XBL 762-6437C  
STRONG



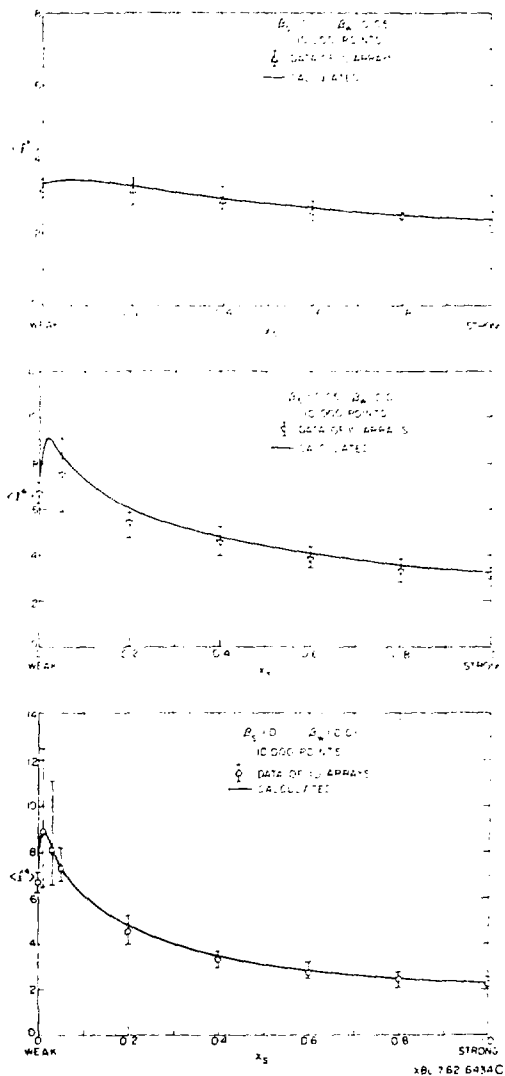
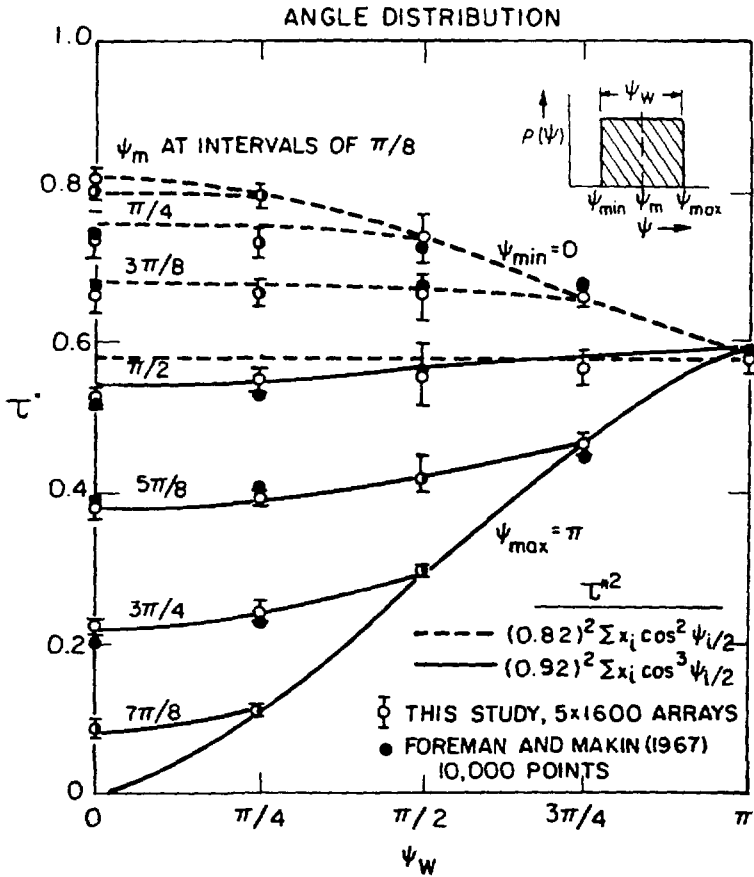
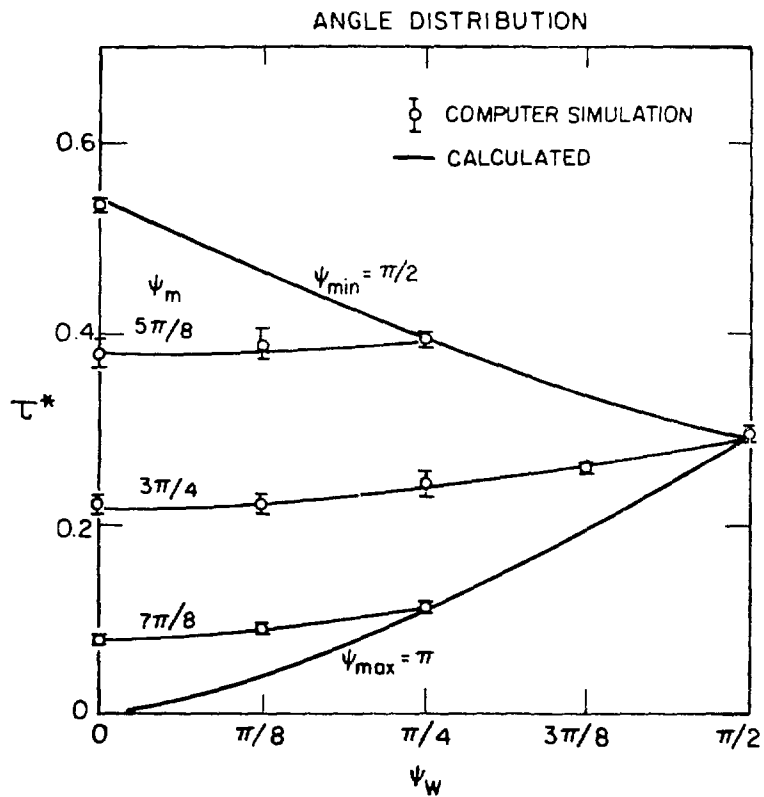


Figure 29



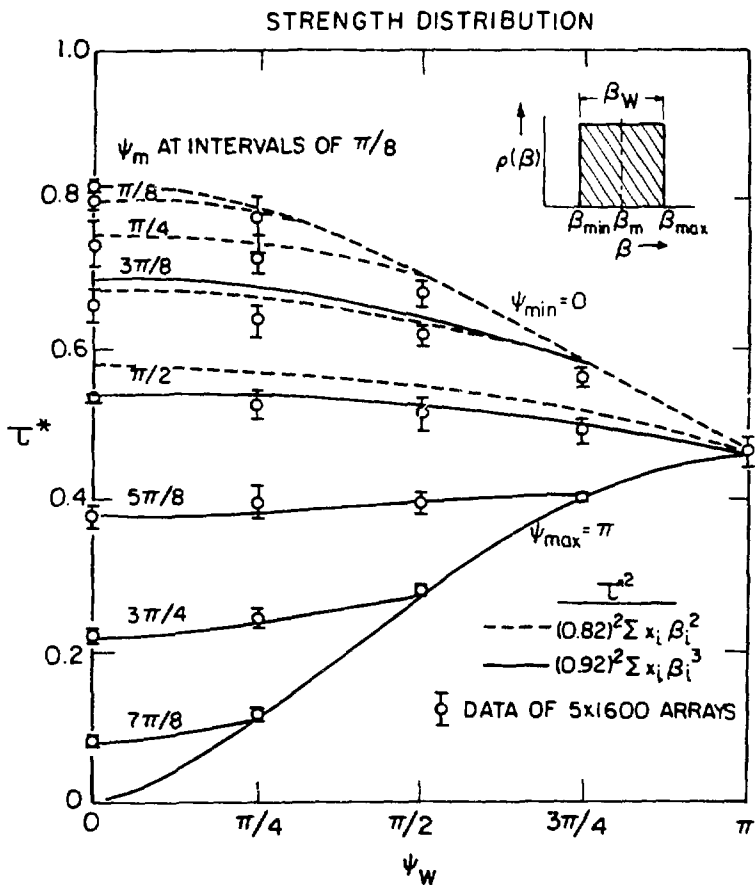
XBL 775-5437A

Figure 30



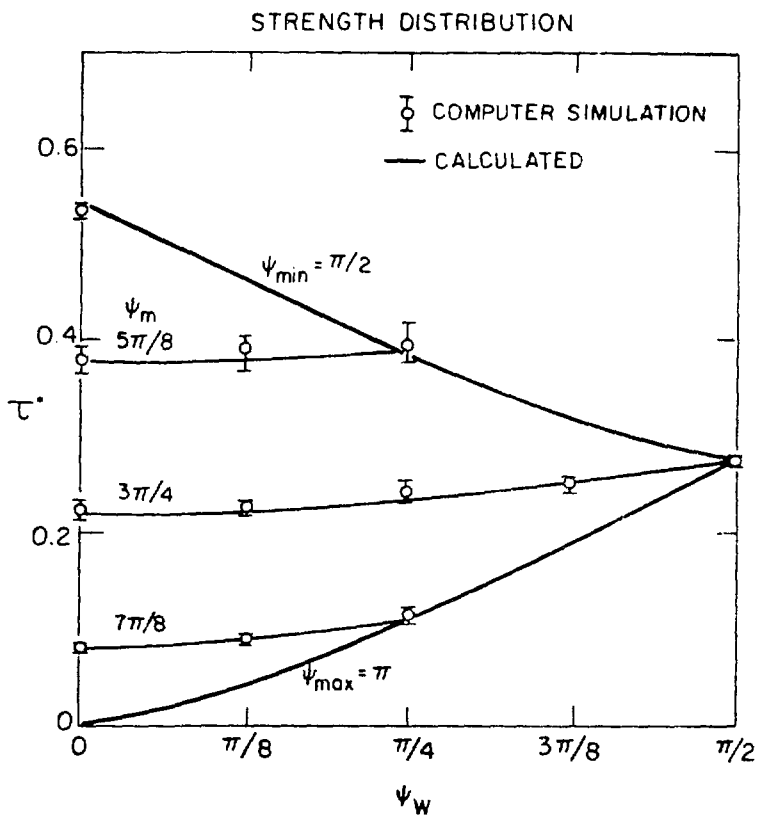
XBL 775-5436

Figure 31



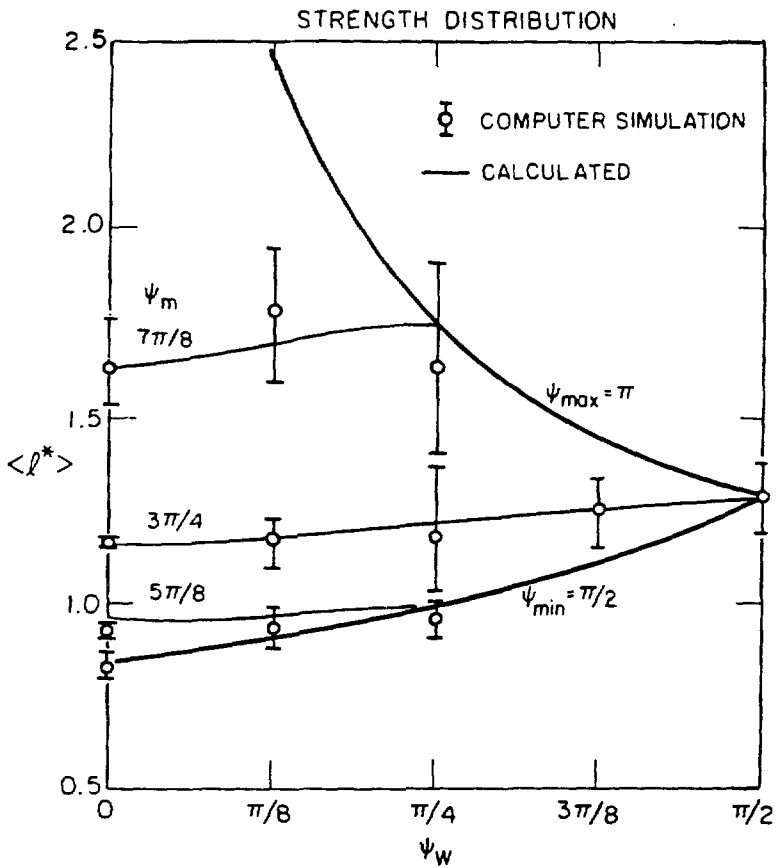
XBL775-5435A

Figure 32



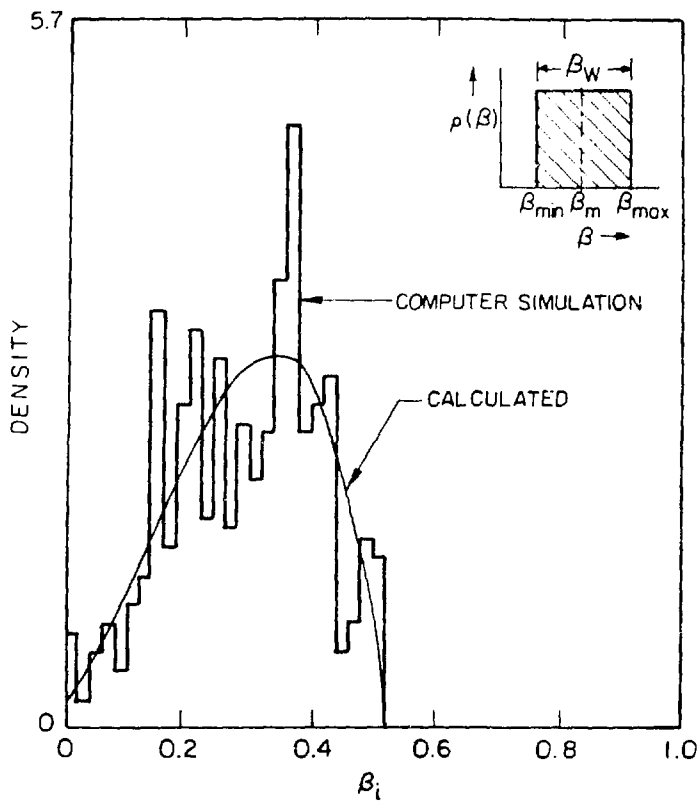
XBL 77 5-5434A

Figure 33



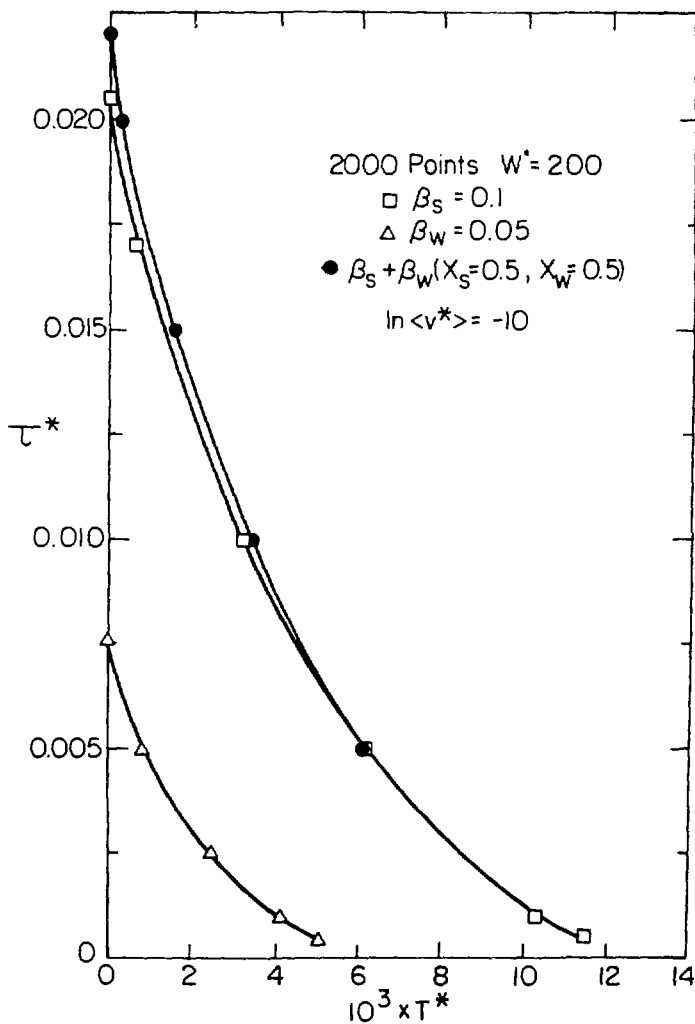
XBL775-5433

Figure 34



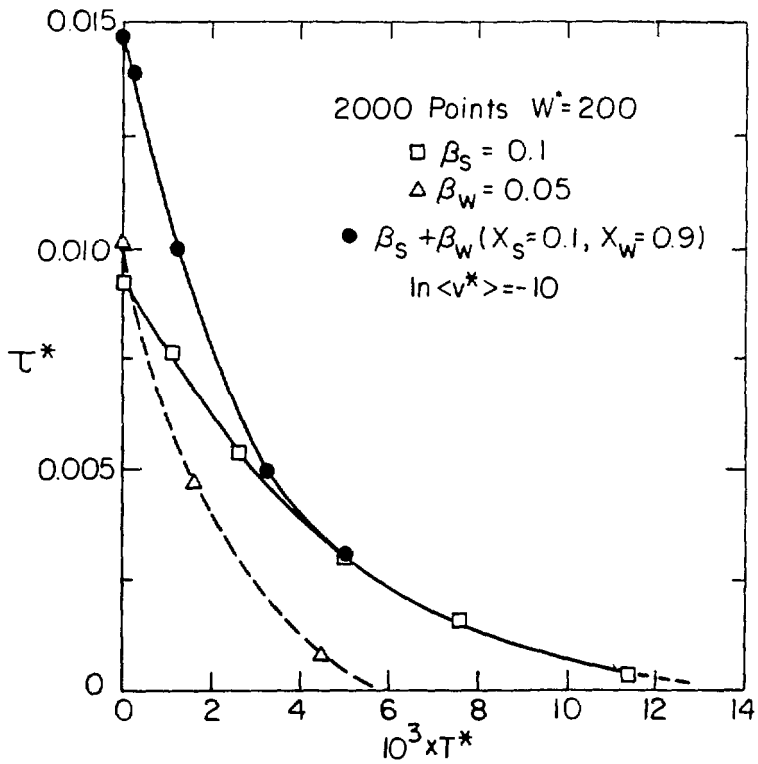
XBL 775-5432

Figure 35



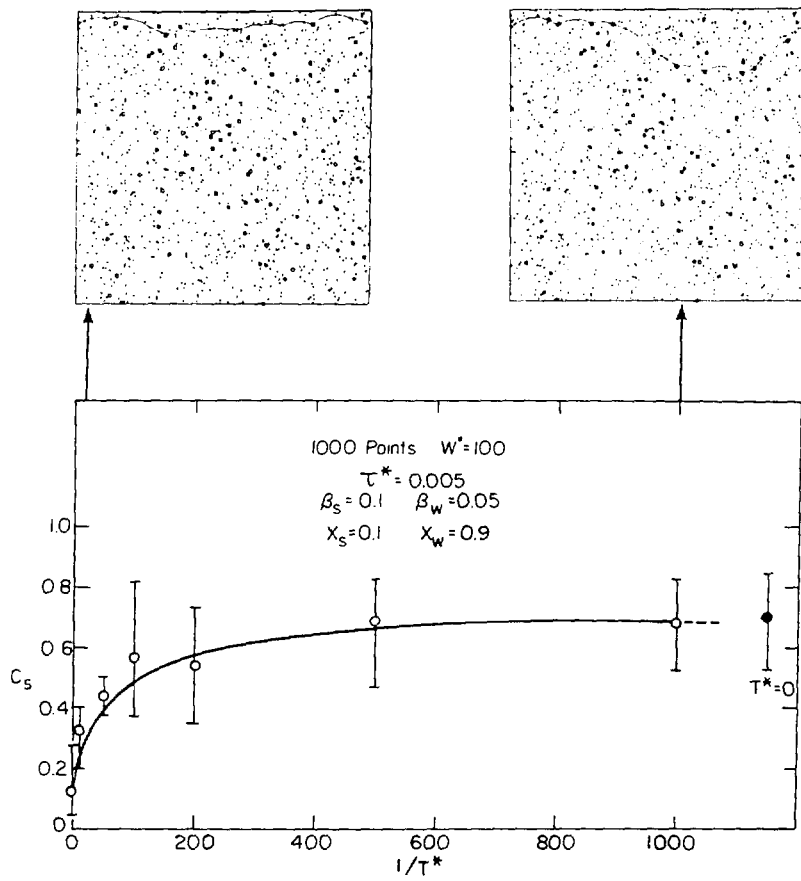
XBL 775-5458A

Figure 36



XBL 775-5459A

Figure 37



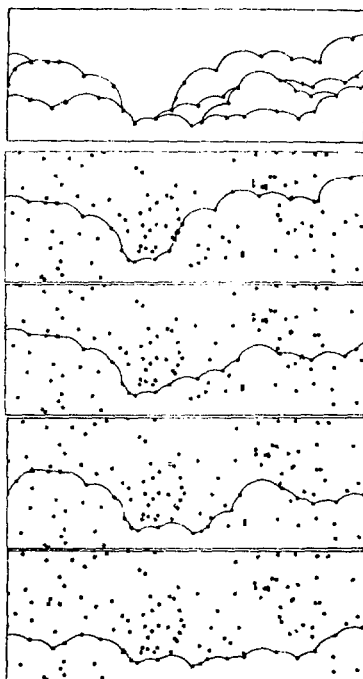
XBL 775-5457 A

Figure 38

TEM EXPERIMENT ON Cu (Barnes, 1965)

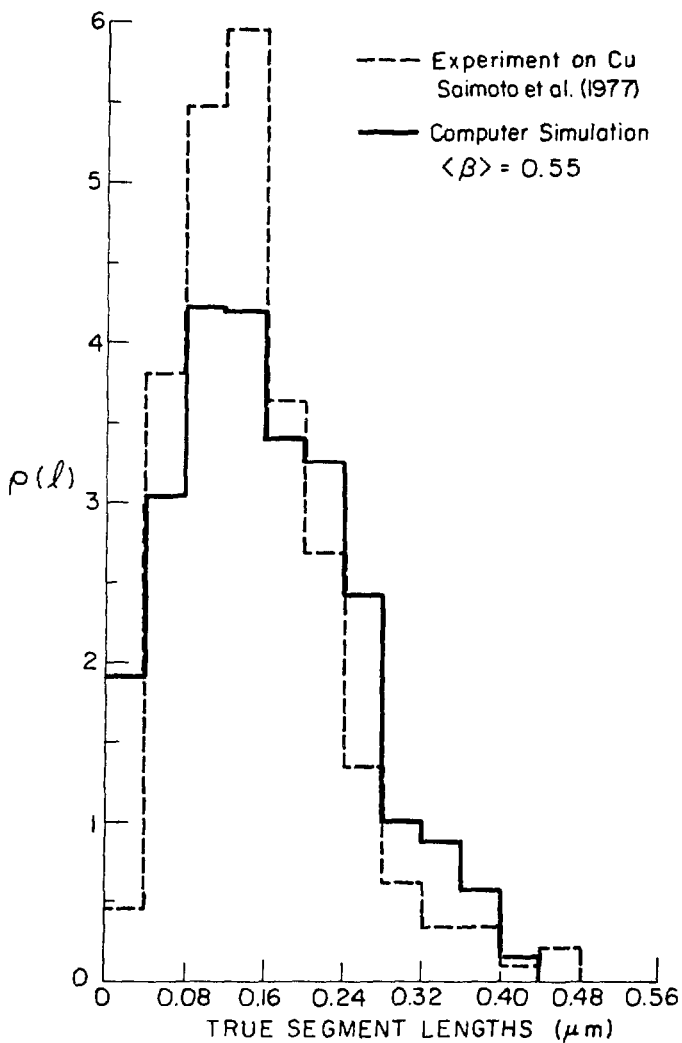


COMPUTER SIMULATION



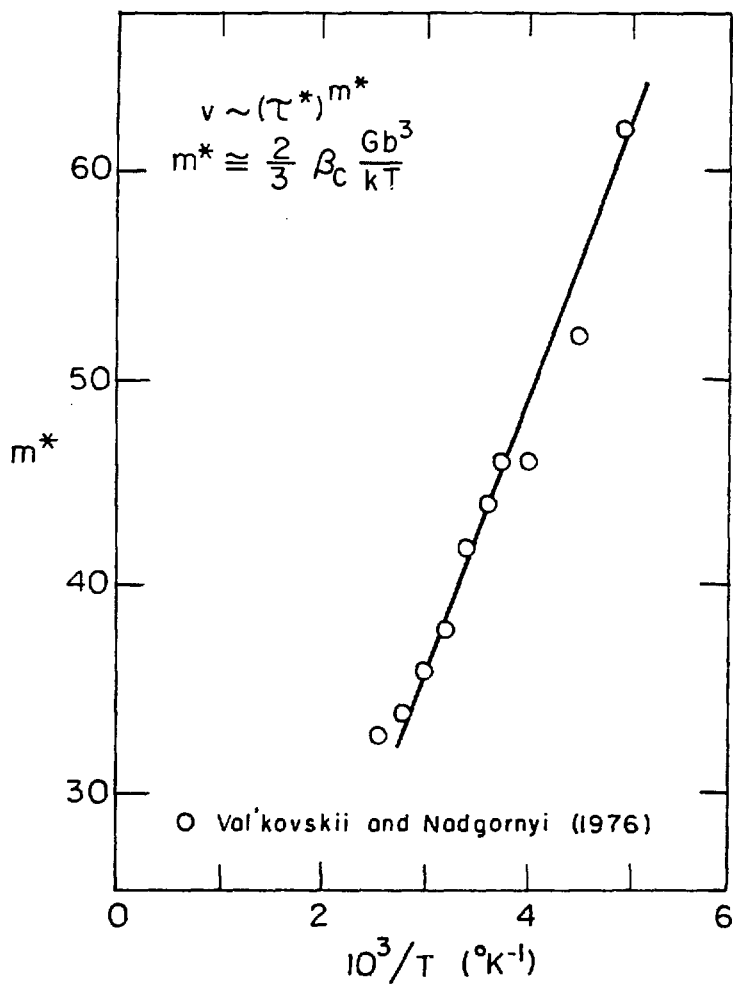
BBB 82-71,4

Figure 39



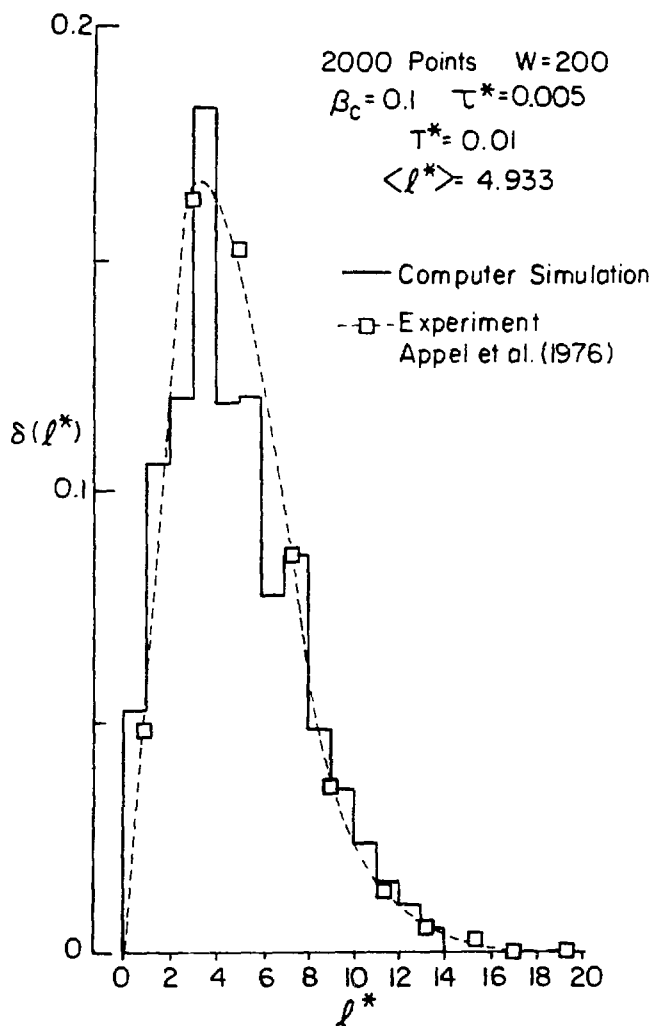
XBL 7B2-7315

Figure 40



XBL 782-4595

Figure 41



XBL775-5454

Figure 42